Ph.D. Thesis

University of Naples "Federico II"

Department of Electrical Engineering
and Information Technology

Doctorate of Philosophy in
Electronics and Telecommunications Engineering

The Role of the Cooperative Paradigm in Traditional and Cognitive Wireless Networks

Roberto Savoia

PhD Coordinator
Ch.mo Prof. Niccoló Rinaldi

Supervisor
Ch.mo Prof. Luigi Paura

XXVI cycle

Dedication

To my family,

for their unconditional love and endless support.

Acknowledgments

First of all, I wish to thank my supervisor Prof. Luigi Paura, for his guidance, support and encouragement, and more important for teaching me the meaning of working collaboratively in a group.

I would like to express my gratitude to Dr. Sara Cacciapuoti and Dr. Marcello Caleffi for their patience and guidance during my Ph.D. studies, and more important for teaching me that criticisms are necessary to improve the quality of our work.

I am also grateful to Prof. Francesco Verde for his valuable teachings and for the very good time spent to discuss about our research work.

I am also grateful to all my colleagues of the Department, and all my friends, for their valuable support during the difficult moments and for sharing with me the best ones.

Contents

List of Figures

Introduction

The word *cooperate* derives from the Latin words *co-* and *operare* (to work), thus it connotes the idea of working together to achieve a common/mutual benefit, as opposed to working in competition for selfish benefit. The main idea behind cooperation is that each cooperating entity can take advantage from the unified action by receiving a benefit as a reward for sharing its resources. This definition is in contrast with altruism, a behavior where one of the participants does not benefit from the interaction to support the others; contrarily, a cooperative behavior aims at guaranteeing the fairness among the cooperators for achieving some advantages.

The cooperative paradigm [1], [2], is extensively applied in nature, both at small scale (i.e., few entities collaborate) and at large scale (i.e., massive collaboration), where the latter includes cooperation between the members of large groups up to the society itself. One illustrative example that gives a perfect idea about the meaning of cooperation is the behavior of vampire bats. These mammals live in large groups and spend most of the day in hollow trees. In the night, they search for large animals that have some bleeding cuts. Once they find such an animal, they will sit next to the cut and simply sip as much blood as they can. Bats try to feed every day, but are able to survive also some time without feeding. The critical limit for a period without any food is sixty hours, where most of the bats without any blood will starve to death. Fortunately, bats that have found enough blood can help the others that have not enough once they are back at their hollow trees. The donation of blood is not based on altruism, but on a strict scoring table. Bats are able to remember which bats gave them blood previously. Furthermore they can detect if other bats getting asked for blood are declining these requests even though they have enough to donate. The bats punish cheaters by refusing to help them when they are in

need, but reward cooperators by helping them when they need it. Bats can live up to eighteen years so cooperation is well established since the cheaters do not survive for long time but cooperators live to breed over many seasons.

Cooperation is a well studied paradigm in many subject areas. One of the most famous example is the prisoner's dilemma, invented around 1950 by Merrill Flood and Melvin Dresher. The prisoner's dilemma tries to describe the problem of cooperation of two entities, where each entity is trying to maximize its own gain, without concern for the well-being of the other entity, and it is a representative of a non-zero sum game regarding the game theory. The prisoner's dilemma describes two thieves who are caught by the police and they are interrogated separately at the same time. Each thief has two options, namely not telling the truth to the police (cooperating with his colleague) or confessing (not cooperating with his colleague). In total there are four possible outcomes. If both confess they will go to jail for a long time. If one confesses and the other is loyal, the latter will go into jail for a very long time, while the former one goes free. But if both cooperate (not telling anything to the police), both will go to jail for a short period only. The dilemma they are facing is that both decisions are made independently (even though before the police arrested them they might have promised to be loyal) and cannot be sure that the other will remain loyal. Moreover, they may hope the other will cooperate so that they could decline their cooperation to get a larger advantage out of it. To cooperate, or not cooperate? This simple question (and the implicit question of whether to trust, or not), expressed in an extremely simple game, is a crucial issue across a broad range of life.

The cooperative paradigm is typically adopted in wireless communication systems [3], [4]. In this context the cooperative entities are wireless nodes connected each other (e.g., wireless terminals and radio base stations) whose purpose is to exchange information in a reliable and efficient manner. Cooperation can be applied at each layer of the Internet protocol stack (TCP/IP), from physical layer to application layer, with the aim to improve the overall network performance. The entities at each layer can act independently from the other layers, or in turn they can act in a collaborative manner by exchanging information each other in order to optimize the performance (cross-layer paradigm). Cooperation also requires that nodes make available their communication

resources, such as battery, computational capabilities and bandwidth, to achieve better performances; thus, the cooperative gain comes at the cost of a cooperation overhead that is an important factor to take into account for the design of cooperative strategies.

Several research efforts in wireless networks have been addressed at the physical layer due to the related fundamental issues and challenges. The main reason is that the reliability of communication over wireless channels is severely compromises by the adverse effects of multipath and shadow fading that introduce strong attenuation in the amplitude of the radio signals. In this case, the main idea behind cooperation is to exploit the *spatial diversity* that arises from the presence of spatially distributed wireless nodes subjected to independent fading conditions: the greater the number of cooperating nodes, the smaller the probability that all the nodes experience severe fading conditions; in the literature, such kind of diversity is also referred to as *cooperative diversity* [5–7]. These nodes may serve as relay stations for a given source-destination pair (*cooperative relaying system*), helping the source to transmit the symbols toward the destination, as shown in Fig. 1, thus yielding higher reliability than direct transmission. The principle is the same used in Multiple-Input Multiple-Output (MIMO) systems, where multiple antennas at both the source and destination create multiple independent channels, if the antennas are sufficiently separated, and such degrees of freedom can be used to improve the reliability or the throughput of communication. However, the use of multiple antennas is not a practical solution in several scenarios, such as wireless ad-hoc and sensor networks, where the nodes have limited hardware and energy capabilities. Contrary, a cooperative relaying system effectively overcome these limitations, and it can be considered like a virtual MIMO system where each relay is a virtual antenna of a multiple antenna device that share its resources with the others relays.

The cooperative transmission process takes place in two phases: (i) *Broadcasting*, (ii) *Relaying*. In the first phase, the source node transmits in broadcast a block of symbols toward the relays, whereas, in the second phase, each relay forwards the block of symbols toward the destination by simply amplifying the received signal (*Amplify-and-Forward* (A&F)), or first by decoding the block of the received symbols (*Decode-and-forward* (D&F)) before to forward them toward the destination, in absence of decoding errors. In particular, an efficient relaying strategy to

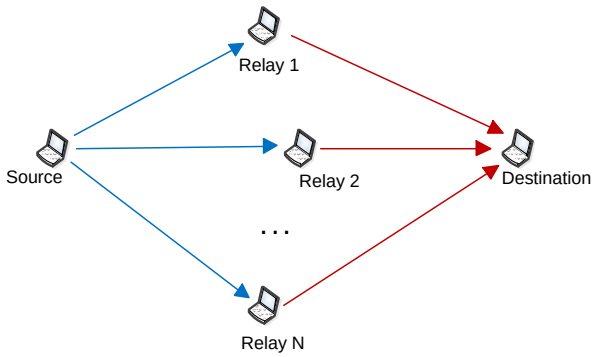

Figure 1: Cooperative relaying system.

transmit the symbols is given by the Space-Time Block Coding (STBC) schemes [8], natively developed for MIMO systems but extensively applied to distributed systems, that introduce correlation in different time slots and among different relays nodes to improve the performance. Contrary to the repetition coding, where the transmission of the relays takes place in different time slots, the use of STBC schemes allows the relays to transmit the information simultaneously, thus improving the spectral efficiency. This advantage is obtained at the cost of an increased complexity of the receiver, since it is required a block decoding to recover the transmitted symbols; however, in particular cases, such as orthogonal STBC, the complexity is notably reduced since it is required only a single symbol decoding.

However, the transmission of information is not the only purpose for using cooperation in wireless networks. Typical examples are given by radio-localization [9], for determining the position of wireless nodes in the network, and beamforming [10], that is a powerful mean for interference suppression along certain directions of an array of antennas, which enables space division multiple access among the wireless nodes. Other examples can be also found at the upper layers of the protocols stack, especially with reference to wireless ad-hoc networks. In particular, at the MAC layer, the cooperation can be used to improve the network throughput [11] or to mitigate the multi-channel hidden terminal problem in multi-channel ad-hoc networks [12]. At the network

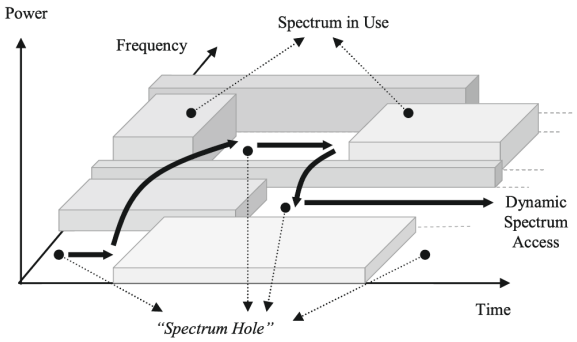

Figure 2: Spectrum Holes concept.

layer [13, 14], the cooperation is intrinsically used to send the packets from a source node to a destination node through multiple intermediate hops, that otherwise would not be possible with a direct transmission due to the large distance between source and destination; furthermore, cooperation can be also used to discover more effective paths toward the destination or to exploit the path-diversity [15] which arises from independent traffic and links conditions characterizing different routes.

Cooperation has been also considered in Cognitive Radio (CR) Networks [16, 17], which differ from traditional networks due to the uncertainty of spectrum availability, and have been introduced as an effective way to improve the radio spectrum efficiency and satisfy the increased demand for bandwidth. This objective is achieved by allowing the unlicensed users, referred to as Cognitive Users (CUs), to dynamically exploit the spectrum opportunities, also referred to as Spectrum Holes (Fig. 2, [18]), namely the portions of the radio spectrum temporarily not occupied by the licensed users, referred to as Primary Users (PUs), which have the priority for using the spectrum and generally do not cooperate with the CUs. To this aim, CR networks necessitate unique functionalities, such as *spectrum sensing* that enables the CUs to detect the transmissions of the PUs through the analysis of the radio signals received from the surrounding radio environment.

The objectives of spectrum sensing are twofold: first, to guarantee an high detection accuracy for avoiding harmful interference against PU networks and, second, to efficiently identify and exploit the spectrum holes for enhancing the transmission capacity and the quality-of-service (QoS) of CR networks. Thus, the sensing accuracy in spectrum sens-

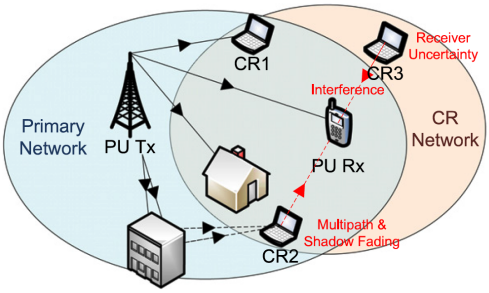

Figure 3: Multipath/shadow fading and receiver uncertainty problem.

ing is a crucial factor that determines the performance of both primary and CR networks. However, these objectives are difficult to achieve due to many factors that compromise the sensing reliability such as multipath fading, shadowing and primary receiver uncertainty problem that happen when the CU is outside the transmission range of the PU transmitter but the primary receiver is inside the CU interference range, as illustrated in Fig. 3 [19]. In these cases, the CUs may experience very low signal-to-noise ratio (SNR) conditions such that it is required a large sensing time to achieve an acceptable detection performance, thus introducing a large sensing overhead.

Also in this case, an effective way to improve the sensing performance is to exploit the spatial diversity through the cooperation of spatially distributed CUs [19], that share their sensing information for making a combined decision more accurate than the individual decision (*cooperative spectrum sensing*). The cooperative sensing process, represented in Fig. 4, takes place in three phases: (i) *Sensing Phase*, where a certain number of CUs perform the sensing of a given channel, by sampling the received signal for a certain interval of time; (i) *Reporting Phase*, where the sensing data are transmitted on a common control channel through point-to-point links, referred to as reporting channels, toward a specific node of the network referred to as Decision Maker; (iii) *Combining Phase*, the Decision Maker combines the received sensing data, by implementing a fusion-rule, and takes the cooperative decision about the presence/absence of the PU that is transmitted in broadcast to all the CUs. Thus, cooperative sensing is an effective way to counteract the fading effects and reduce the primary receiver uncertainty problem, thus yielding to higher detection performance than local spectrum sensing,

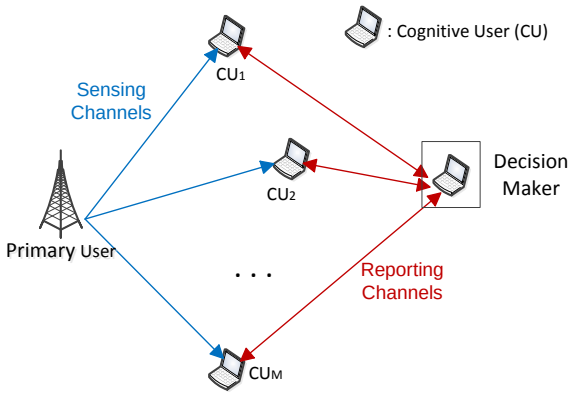

Figure 4: Cooperative sensing process.

with a lower sensing time, that allows to reduce interference against the PU networks and increase the transmission capacity of CR networks.

Similarly to traditional ad-hoc networks, the cooperation can be also used at MAC and network layers in cognitive radio ad-hoc networks [18], but the problems are more challenging due to the uncertainty of spectrum availability, that varies in time and space, and due to the interference avoidance principle against the PU networks.

Thus, the scope of this thesis is to demonstrate that the cooperative paradigm in wireless network is an effective way to counteract the impairments of wireless channels caused by the fading effects, through the exploitation of the spatial diversity, and so to guarantee satisfactory performance that otherwise would not be achievable through an individual action. More specifically, the advantages of the cooperative paradigm are shown with reference to both traditional relay networks, for cooperative transmission, and the emerging cognitive radio networks, for cooperative spectrum sensing, and three different works on these research topics are presented.

Therefore, the thesis is organized as follows:

- In **Chapter 1**, the performance analysis of distributed STBC schemes involving multiple decode-and-forward relays is carried out in the presence of impulsive noise, which, together with multipath fading, is one of the major sources of performance degrada-

tion in many wireless systems. To this aim, the Middleton Class-A impulsive noise model is adopted, and as decoding structures at the destination, the maximum-likelihood (ML) detector (optimum detector), its ideal version (IML), as well as the minimum-distance (MD) detector, that is suboptimum in non-Gaussian noise, are considered. For the proposed receiving structures, the performances are derived in terms of average bit-error rate, coding gain, finite signal-to-noise ratio (SNR) diversity order and asymptotic (i.e., when the SNR is sufficiently large) diversity order, and the impact of impulsive noise on these performance metrics is studied.

- In **Chapter 2**, the performance analysis of several cooperative spectrum sensing techniques in cognitive radio networks is carried out for two different decision approaches according to the role of the decision maker. In the first approach, referred to as Combining Decision (CD), the role of the decision maker is only to combine the sensing information collected from its cooperators, without participating in the sensing of the monitored band. Differently, in the second approach, referred to as Sensing & Combining Decision (SCD), the decision maker combines not only the sensing information of its cooperators, but also its own local sensing information. The accuracy of the cooperative decision strictly depends on the selected decision approach (CD or SCD), independently of the considered cooperative technique. For this reason, the criteria for an effective decision-approach selection are analytically derived with the object of maximizing the detection accuracy in presence of realistic channel propagation effects.

- In **Chapter 3**, the spatio-temporal spectrum sensing design problem for cognitive radio networks in the presence of PU mobility is addressed, with the aim to optimize the sensing time that maximizes the actual transmission capacity achieved by the CU with a limited sensing accuracy, while satisfying the PU interference constraints. This is a crucial problem since the choice of the sensing time deeply affect the sensing accuracy that is an important factor that determines the actual performance achieved by the CU. This problem is very challenging in the spatio-temporal spectrum sensing scenario with PU mobility, since the mobility effect can deeply influence the transmission capacity achieved by the CU.

Chapter 1

Performance Analysis of Distributed Space-Time Block Coding Schemes in Middleton Class-A Noise

1.1 Introduction

Cooperative diversity [5–7], arising from the presence of terminals distributed in space, which may serve as relay stations for a given source-destination pair, offers significant robustness against the adverse effects of fading in wireless communications, thus yielding higher reliability and throughput than direct transmission. *Decode-and-Forward* (D&F) and *Amplify-and-Forward* (A&F) relaying are popular cooperation protocols: in the former one, the relay node forwards the source symbols if it has correctly decoded the received data; in the latter one, the relay node simply scales the received signal and retransmits it to the destination. Early cooperative communication schemes employed a single relay [5], [6]; subsequently, multiple relays have been allowed to forward signals at the same time [7]. In this latter case, to benefit from cooperative diversity without a significant loss in spectral efficiency, the use of *Space-Time Block Coding* (STBC) among the relays has been proposed in [20–29], which was originally designed for co-located antennas [30], [31]. STBC rules can be employed in a *distributed* manner by allowing each relay to transmit a linear combination of the L columns of a conventional

STBC matrix. The weights of the aforementioned linear combination can be optimally assigned to each relay by a central unit [20], i.e., in a *centralized* fashion, which requires extra signaling overhead. On the other hand, such weights can be chosen by the relays locally in a random way [21]- [29], i.e., in a *decentralized* manner. Decentralized techniques eliminate the requirement of space-time codeword assignment and reduce the coordination among the source and the relays, thus leading to a reduction in signaling cost.

Design and analysis of distributed STBC (DSTBC) rules [20–29] focus on the classical additive white Gaussian noise (AWGN) model. However, together with multipath fading, impulsive (non-Gaussian) noise is the prevalent source of performance degradation in many wireless scenarios, such as indoor, urban, rural, industrial, medical, commercial, modern local and personal area networks [32–34]. Recently, the use of cooperative techniques has been also proposed in [35], [36] for power line communications. A widely-accepted impulse noise model is the *Middleton Class-A* (MCA) one [37–39], which was derived bearing in mind the real physical mechanisms that generate disturbance in communication receivers, whose validity has been confirmed by many measurement campaigns. Other well-known models are the Bernoulli-Gauss one [40], which can be regarded as an approximation to the more fundamental MCA noise model in many practical scenarios, and the symmetric alpha stable distribution [41], which models the multiple access interference in a multi-user network when the interfering nodes are scattered according to a spatial Poisson point process. The combined effects of fading and impulsive noise on the performance of MIMO systems with co-located antennas have been studied in [42], [43] by using the MCA noise model and in [44] by considering the symmetric alpha stable distribution. More recently, performance and optimization of cooperative diversity systems in impulsive noise have been considered in [45], [46]. Both the A&F diversity scheme considered in [45] and the D&F cooperative system studied in [47] do not employ DSTBC by assuming that the source and the relays use orthogonal channels, e.g., the source and the relays transmit in different time slots or different frequency bands, and maximum ratio combining techniques are used at the destination to extract the source information from the received signals. Even though DSTBC is employed across the relays in [46], the performance analysis in the case of minimum distance (MD) detection at the destination is targeted at A&F

relaying and it is based on the assumption that impulsive noise samples at the relays and the destination are temporally dependent during a transmission frame.

The aim of this work [48] is to study the effects of both fading and impulsive noise on cooperative links employing multiple D&F relays with DSTBC, by completing and extending the preliminary results of [49]. To this goal, we use the MCA noise model and, as decoding structures at the destination, we consider the maximum-likelihood (ML) detector, its *ideal* version (IML), as well as the MD detector that is suboptimum in non-Gaussian noise.[1] Our analysis shows that the IML detector is able to satisfactorily counteract the impulsiveness of the noise in the *asymptotic* signal-to-noise ratio (SNR) regime,[2] by achieving an asymptotic diversity order $R_{\max}$ that is equal to the minimum between L and the maximum number of cooperating nodes (relays plus source). However, thanks to closed-form formula directly linking the *finite-SNR* performance to the main parameters of both impulse noise and STBC, we highlight that the IML detector pays a penalty in terms of diversity order for a wide range of SNR values of practical interest; in particular, we show that, in the case of complex orthogonal STBC, such a penalty becomes negligible for increasing values of $R_{\max}$. It is also demonstrated that, even though it ensures the same asymptotic diversity order $R_{\max}$ of the IML detector, the performance of the simpler MD detector is adversely affected not only in terms of finite-SNR diversity order but also in terms of coding gain; specifically, we show that, in the case of complex orthogonal STBC, there is an increase in such a penalty as $R_{\max}$ grows.

The chapter is organized as follows. In Section 1.2, the cooperative protocol is described and the detection process at the relays is analyzed by using the MCA noise model introduced in Subsection 1.1.1. The asymptotic- and finite-SNR performances of the IML and MD detectors are derived in Sections 1.3 and 1.4, respectively. Monte Carlo simulation results, in terms of average bit-error-rate (ABER) and finite-SNR

[1] Alternative suboptimal methods for reducing the adverse effect of impulse noise is to precede the MD detector with a memoryless nonlinearity [50]. In some contexts, such as multiuser detection [51] and multicarrier modulation [52], this strategy allows to bridge much of the gap between the IML (or ML) detector and the MD one, without a substantial increase in complexity. A detailed study of the tradeoff between performance and complexity of such detectors in the DSTBC framework at hand is outside the scope of this work.

[2] Our numerical results show that ML and IML detectors substantially exhibit the same performances.

diversity order, are presented in Section 1.5 for the ML, IML, and MD detectors and compared with our analytical results. Finally, some conclusions are drawn in Section 1.6.

1.1.1 Notations and preliminaries

The fields of complex, real, and nonnegative integer numbers are denoted with $\mathbb{C}$, $\mathbb{R}$, and $\mathbb{N}$, respectively; matrices [vectors] are denoted with upper [lower] case boldface letters (e.g., $\mathbf{A}$ or $\mathbf{a}$); the field of $m \times n$ complex [real or nonnegative integer] matrices is denoted as $\mathbb{C}^{m\times n}$ [$\mathbb{R}^{m\times n}$ or $\mathbb{N}^{m\times n}$], with $\mathbb{C}^m$ [$\mathbb{R}^m$ or $\mathbb{N}^m$] used as a shorthand for $\mathbb{C}^{m\times 1}$ [$\mathbb{R}^{m\times 1}$ or $\mathbb{N}^{m\times 1}$]; the superscripts $*$, T, H, and -1 denote the conjugate, the transpose, the conjugate transpose, and the inverse of a matrix, respectively; $|\mathcal{A}|$ represents the cardinality of the set $\mathcal{A}$; $\min(x, y)$ [$\max(x, y)$] is the minimum [maximum] value between $x \in \mathbb{R}$ and $y \in \mathbb{R}$; $\mathbf{0}_m \in \mathbb{R}^m$, $\mathbf{1}_m \in \mathbb{R}^m$, $\mathbf{O}_{m\times n} \in \mathbb{R}^{m\times n}$, and $\mathbf{I}_m \in \mathbb{R}^{m\times m}$ denote the null vector, the vector whose entries are all equal to one, the null matrix, and the identity matrix, respectively; $\{\mathbf{a}\}_i$ indicates the ith element of $\mathbf{a} \in \mathbb{C}^m$, with $i \in \{1, 2, \ldots, m\}$; $\mathrm{rank}(\boldsymbol{A})$ is the rank of $\mathbf{A} \in \mathbb{C}^{m\times n}$; $\det(\boldsymbol{A})$ and $\mathrm{trace}(\mathbf{A})$ denote the determinant and the trace of $\mathbf{A} \in \mathbb{C}^{n\times n}$, respectively; $\|\boldsymbol{a}\|$ is the Euclidean norm of $\boldsymbol{a} \in \mathbb{C}^n$; the eigenvalues of a matrix $\mathbf{A} \in \mathbb{C}^{m\times m}$ are denoted as $\mu_i(\mathbf{A})$, for $i \in \{1, 2, \ldots, m\}$, and, when they are real, they are ordered as $\mu_1(\mathbf{A}) \geq \mu_2(\mathbf{A}) \geq \cdots \geq \mu_m(\mathbf{A})$; let $\mathbf{A} \in \mathbb{C}^n$ and $\mathbf{B} \in \mathbb{C}^n$ be Hermitian matrices, we write $\mathbf{A} \succ \mathbf{B}$ [$\mathbf{A} \succeq \mathbf{B}$] if the matrix $\mathbf{A} - \mathbf{B}$ is positive definite [semidefinite]; $\binom{n}{k}$ is the binomial coefficient, for $n, k \in \mathbb{N}$; $o(x)$ denotes the Landau symbol, i.e., for a function $f(x) = o(g(x))$, the ratio $f(x)/g(x) \to 0$, as $x \to 0$; $\mathrm{Q}(x) \triangleq (1/\sqrt{2\pi}) \int_x^{+\infty} e^{-u^2/2}\,\mathrm{d}u$ denotes the Q function; $P(A)$ denotes the probability that an event A occurs and $P(A \,|\, B)$ is the conditional probability of A given an event B; the operator $\mathrm{E}[\cdot]$ denotes ensemble averaging and, specifically, $\mathrm{E}_{\tilde{\mathbf{x}}\,|\,\tilde{\mathbf{Y}}}[\cdot]$ is the conditional mean with respect to the random vector $\tilde{\mathbf{x}} \in \mathbb{C}^m$ given the random matrix $\tilde{\mathbf{Y}} \in \mathbb{C}^{n\times k}$; if $\tilde{\mathbf{Y}} = \mathbf{Y}$, the value of the random variable (RV) $\mathrm{E}_{\tilde{\mathbf{x}}\,|\,\tilde{\mathbf{Y}}}[\cdot]$ is denoted as $\mathrm{E}_{\tilde{\mathbf{x}}\,|\,\tilde{\mathbf{Y}}=\mathbf{Y}}[\cdot]$; a circular symmetric complex Gaussian random vector $\boldsymbol{x} \in \mathbb{C}^n$ with mean $\boldsymbol{\mu} \in \mathbb{C}^n$ and covariance matrix $\boldsymbol{K} \in \mathbb{C}^{n\times n}$ is denoted as $\boldsymbol{x} \sim \mathcal{CN}(\boldsymbol{\mu}, \boldsymbol{K})$.

In the high-SNR regime, the average symbol error probability (ASEP) for a digital communication system over a fading channel usually behaves

as $\mathrm{ASEP}(\gamma) \leq (G_c\,\gamma)^{-G_d}$ [53], where γ denotes the average SNR, G_c is the coding gain, and G_d is the *asymptotic* diversity order; at an arbitrary SNR γ, the *finite-SNR* diversity order $G_d(\gamma)$ is defined [54] by the negative slope of the log-log plot of the average pairwise error probability (APEP) versus SNR, that is,

$$G_d(\gamma) \triangleq -\frac{\mathrm{d}\,\log[\mathrm{APEP}(\gamma)]}{\mathrm{d}\log(\gamma)} = -\frac{\gamma}{\mathrm{APEP}(\gamma)}\,\frac{\mathrm{d}\,\mathrm{APEP}(\gamma)}{\mathrm{d}\gamma} \tag{1.1}$$

which converges to G_d for asymptotically high SNR values.

According to [37]- [39], the MCA complex noise RV $\tilde{x}$ is the sum of two independent components: a Gaussian component $\tilde{n}$ with variance $\sigma_{\tilde{n}}^2$ and an interfering component $\tilde{\imath}$ with variance $\sigma_{\tilde{\imath}}^2$, and its probability density function (pdf) $f_{\tilde{x}}(x)$, with $x \in \mathbb{C}$, is given by

$$f_{\tilde{x}}(x) = \sum_{m=0}^{+\infty} p_{\widetilde{m}}(m)\, f_{\tilde{x}\,|\,\widetilde{m}}(x\,|\,m) \tag{1.2}$$

with

$$f_{\tilde{x}\,|\,\widetilde{m}}(x\,|\,m) \triangleq \frac{1}{\pi\,\sigma^2\,\sigma_m^2}\,\exp\left\{-\frac{|x|^2}{\sigma^2\,\sigma_m^2}\right\} \tag{1.3}$$

and

$$p_{\widetilde{m}}(m) \triangleq \exp\{-\lambda\}\,\frac{\lambda^m}{m!} \quad \text{and} \quad \sigma_m^2 \triangleq \frac{m\,\lambda^{-1}+\Gamma}{1+\Gamma} \tag{1.4}$$

where λ is the impulsive index, i.e., the average number of impulses affecting the receiver in a symbol period, $\Gamma \triangleq \sigma_{\tilde{n}}^2/\sigma_{\tilde{\imath}}^2 > 0$ is the Gaussian-to-impulse ratio, and $\sigma^2 = \sigma_{\tilde{n}}^2 + \sigma_{\tilde{\imath}}^2$ is the variance of $\tilde{x}$. Such a model comes from the assumption that the number of interfering impulses affecting the receiver is a Poisson RV $\widetilde{m}$ with parameter λ, whose probability mass function (pmf) is denoted as $p_{\widetilde{m}}(m)$, which represents the probability of having $m \in \mathbb{N}$ impulses within the considered symbol period. It is seen from (1.2) that $f_{\tilde{x}\,|\,\widetilde{m}}(x\,|\,m)$ is the conditional pdf of $\tilde{x}$ given $\widetilde{m} = m$ and, thus, $\tilde{x}\,|\,\widetilde{m} \sim \mathcal{CN}(0, \sigma^2\,\sigma_m^2)$. The parameters λ and Γ control the "impulsiveness" of the noise: for $\lambda \ll 1$, the noise $\tilde{x}$ becomes more and more impulsive; for $\lambda \geq 1$, the probability distribution of $\tilde{x}$ approaches that of Gaussian noise;[3] for small values of Γ, the noise becomes more impulsive; the noise tends to be Gaussian for large values of Γ.

[3] In the case of $\lambda = 10$, the noise $\tilde{x}$ can be regarded as a circular symmetric complex Gaussian RV.

1.2 Cooperative transmission scheme and performance analysis at the relays

We consider a wireless network where $N_{\max}$ randomly and independently placed *potential* relay nodes might assist the data transmission between a given source-destination pair. Each node in the network employs a single transmit/receive antenna. The relays work in half-duplex mode, i.e., they cannot transmit and receive at the same time, and they adopt a D&F relaying protocol. The link between each node pair is modeled as a frequency-flat[4] Rayleigh block-fading channel, i.e., it is characterized by a single fading coefficient that remains constant within $P > 0$ symbol intervals. Let the source wish to send the block $\tilde{\mathbf{a}} \triangleq [\tilde{a}_1, \tilde{a}_2, \ldots, \tilde{a}_K]^T \in \mathbb{C}^K$ towards the destination, with $K \leq P$, which is composed of independent and identically distributed (i.i.d.) zero-mean unit-variance equiprobable symbols. The vector $\tilde{\mathbf{a}}$ assumes values in the *symbol set* $\mathcal{A} = \{\mathbf{a}_1, \mathbf{a}_2, \ldots, \mathbf{a}_{|\mathcal{A}|}\}$. The cooperative transmission takes place in two phases.

In Phase I (*broadcast phase*), which spans a time interval of K consecutive symbol periods, the source broadcasts the symbol vector $\tilde{\mathbf{a}}$ to all the potential relays, which try to decode it. The discrete-time baseband equivalent received signal at the nth relay is given by $\tilde{\mathbf{z}}_n = \tilde{f}_n \, \tilde{\mathbf{a}} + \tilde{\mathbf{w}}_n$, for $n \in \{1, 2, \ldots, N_{\max}\}$, where $\tilde{f}_n$ denotes the channel gain between the source and the nth relay, whereas the entries of the noise vector $\tilde{\mathbf{w}}_n \triangleq [\tilde{w}_{n,1}, \tilde{w}_{n,2}, \ldots, \tilde{w}_{n,K}]^T \in \mathbb{C}^K$ are modeled as i.i.d. MCA RVs [43, 55], whose pdf is given by (1.2), with parameters Γ, λ, and variance $\sigma^2 \triangleq \mathrm{E}[|\tilde{w}_{n,k}|^2]$. Moreover, according to the Rayleigh-fading assumption, the channel vector $\tilde{\mathbf{f}} \triangleq [\tilde{f}_1, \tilde{f}_2, \ldots, \tilde{f}_{N_{\max}}]^T \in \mathbb{C}^{N_{\max}}$ is modeled as $\tilde{\mathbf{f}} \sim \mathcal{CN}(\mathbf{0}_{N_{\max}}, \mathbf{\Sigma}_{\tilde{\mathbf{f}}})$, with $\mathbf{\Sigma}_{\tilde{\mathbf{f}}} \triangleq \mathrm{diag}(\sigma^2_{\tilde{f}_1}, \sigma^2_{\tilde{f}_2}, \ldots, \sigma^2_{\tilde{f}_{N_{\max}}})$, which is independent of $\tilde{\mathbf{a}}$ and $\{\tilde{\mathbf{w}}_n\}_{n=1}^{N_{\max}}$. Assuming that error detection mechanisms such as cyclic redundancy check are employed at the potential relays, only those nodes that successfully decode $\tilde{\mathbf{a}}$ will serve as relays in the subsequent phase, whose number is unknown and randomly time-varying. Following the related literature, e.g., [5], [20], [21], perfect synchronization is assumed at the symbol level among the source and

[4]This assumption is made for the sake of simplicity and might be removed. If the channel is frequency selective, orthogonal frequency-division multiplexing techniques may be used to transform a frequency-selective channel into parallel frequency-non-selective channels.

the relays.

In Phase II (*relaying phase*), which spans a time interval of P consecutive symbol periods, all the *active* relays, along with the source, simultaneously transmit in the same frequency band a space-time block coded version of $\tilde{\mathbf{a}}$ and it is assumed that the destination uses only the data received in such a phase to decode the source symbols. More precisely, as done in standard STBC [30], [31], the source and each active relay first map the vector $\tilde{\mathbf{a}}$ onto a given STBC matrix $\boldsymbol{\mathcal{C}}(\tilde{\mathbf{a}}) \in \mathbb{C}^{P\times L}$, where $L \geq 2$ denotes the number of *virtual* antennas in the underlying space-time code. Without considering any specific code structure, we only assume that code matrix satisfies the rank criterion [31], which states that, for any pair $\boldsymbol{\mathcal{C}}_k \triangleq \boldsymbol{\mathcal{C}}(\mathbf{a}_k)$ and $\boldsymbol{\mathcal{C}}_\ell \triangleq \boldsymbol{\mathcal{C}}(\mathbf{a}_\ell)$, where $\mathbf{a}_k, \mathbf{a}_\ell \in \mathcal{A}$ with $k \neq \ell$, the matrix $\boldsymbol{\mathcal{C}}_{k,\ell} \triangleq \boldsymbol{\mathcal{C}}_k - \boldsymbol{\mathcal{C}}_\ell$ is full rank, i.e., $\mathrm{rank}(\boldsymbol{\mathcal{C}}_{k,\ell}) = \min(P, L)$. Then, the source and each active relay virtually act as a single antenna in a multiple antennas transmitter, by transmitting a linear combination of the columns of $\boldsymbol{\mathcal{C}}(\tilde{\mathbf{a}})$. Specifically, let $\tilde{\mathbf{r}}_n \in \mathbb{C}^L$ be a *signature* vector containing the linear combination coefficients for the nth node, the transmitted code $\tilde{\mathbf{x}}_n \in \mathbb{C}^P$ is given by $\tilde{\mathbf{x}}_n = \boldsymbol{\mathcal{C}}(\tilde{\mathbf{a}})\,\tilde{\mathbf{r}}_n$, for $n \in \{0, 1, \ldots, N_{\max}\}$ (where $n = 0$ is the representative index of the source), and, then, the baseband equivalent discrete-time signal received at the destination assumes the form

$$\begin{aligned}\tilde{\mathbf{y}} &= \tilde{g}_0\,\tilde{\mathbf{x}}_0 + \sum_{n=1}^{N_{\max}} \tilde{s}_n\,\tilde{g}_n\,\tilde{\mathbf{x}}_n + \tilde{\mathbf{d}} \\ &= \boldsymbol{\mathcal{C}}(\tilde{\mathbf{a}})\,\tilde{\boldsymbol{\mathcal{R}}}\,\tilde{\mathbf{S}}\,\tilde{\mathbf{g}} + \tilde{\mathbf{d}} = \boldsymbol{\mathcal{C}}(\tilde{\mathbf{a}})\,\tilde{\mathbf{h}} + \tilde{\mathbf{d}} \end{aligned} \tag{1.5}$$

where $\tilde{g}_0$ is the channel coefficient between the source and the destination; for $n \in \{1, 2, \ldots, N_{\max}\}$, $\tilde{s}_n \in \{0, 1\}$ is a binary RV indicating if the nth relay is active in Phase II (i.e., if it correctly decoded the symbols of $\tilde{\mathbf{a}}$), with $\tilde{s}_{n_1}$ statistically independet of $\tilde{s}_{n_2}$, for $n_1 \neq n_2 \in \{1, 2, \ldots, N_{\max}\}$; $\tilde{g}_n$ denotes the fading channel gain between the nth active relay and the destination; the matrix $\tilde{\boldsymbol{\mathcal{R}}} \triangleq [\tilde{\mathbf{r}}_0, \tilde{\mathbf{r}}_1, \ldots, \tilde{\mathbf{r}}_{N_{\max}}] \in \mathbb{C}^{L\times(N_{\max}+1)}$ collects the signature vectors used by the source and the relays; according to the Rayleigh-fading assumption, the vector $\tilde{\mathbf{g}} \triangleq [\tilde{g}_0, \tilde{g}_1, \ldots, \tilde{g}_{N_{\max}}]^T \in \mathbb{C}^{N_{\max}+1}$ is modeled as $\tilde{\mathbf{g}} \sim \mathcal{CN}(\mathbf{0}_{N_{\max}+1}, \boldsymbol{\Sigma}_{\tilde{\mathbf{g}}})$, with $\boldsymbol{\Sigma}_{\tilde{\mathbf{g}}} \triangleq \mathrm{diag}(\sigma^2_{\tilde{g}_0}, \sigma^2_{\tilde{g}_1}, \ldots, \sigma^2_{\tilde{g}_{N_{\max}}})$, which is statistically independent of $\tilde{\mathbf{S}} \triangleq \mathrm{diag}(1, \tilde{s}_1, \tilde{s}_2, \ldots, \tilde{s}_{N_{\max}}) \in \mathbb{R}^{(N_{\max}+1)\times(N_{\max}+1)}$; the vector $\tilde{\mathbf{h}} \triangleq \tilde{\boldsymbol{\mathcal{R}}}\,\tilde{\mathbf{S}}\,\tilde{\mathbf{g}} \in \mathbb{C}^L$ represents the *overall* channel between the cooperating

nodes in Phase II and the destination; the vector $\tilde{\mathbf{d}} \triangleq [\tilde{d}_1, \tilde{d}_2, \ldots, \tilde{d}_P]^T \in \mathbb{C}^P$ denotes additive noise, which is independent of $\tilde{\mathbf{a}}$ and $\tilde{\mathbf{h}}$, whose entries are modeled as i.i.d. MCA RVs [43], [55], whose pdf is given by (1.2), with parameters Γ, λ, and variance $\sigma^2 \triangleq \mathrm{E}[|\tilde{d}_p|^2]$.[5] The signal model (1.5) is quite general and subsumes different distributed STBC approaches. In a *centralized* approach [5], each simultaneously transmitting node transmits a *pre-assigned* column of the STBC matrix $\boldsymbol{\mathcal{C}}(\tilde{\mathbf{a}})$, i.e., $L = N_{\max} + 1$ and $\tilde{\boldsymbol{\mathcal{R}}}$ is proportional to $\mathbf{I}_{N_{\max}+1}$. In a *decentralized deterministic* scheme [20], matrix $\tilde{\boldsymbol{\mathcal{R}}}$ has to be properly optimized. In the *decentralized randomized* coding rule developed in [21]- [29], the vector $\tilde{\mathbf{r}}_n$ is random and generated locally at the nth node. It is noteworthy that, in decentralized strategies, there is *no* relationship between L and the number of active relays in Phase II and, thus, L can be chosen without knowing what is the number of relays that are simultaneously transmitting.

For the statistical characterization of the RVs $\tilde{s}_1, \tilde{s}_2, \ldots, \tilde{s}_{N_{\max}}$, it is seen [56] that $\tilde{s}_n$ is a Bernoulli RV, whose success probability is $P(\tilde{s}_n = 1) = (1 - \mathrm{ASEP}_n)^K$, for $n \in \{1, 2, \ldots, N_{\max}\}$, where ASEP_n is the *average* (over the random gain $\tilde{f}_n$) symbol error probability (SEP) at the output of the ML detector of the nth relay, which is modulation dependent. It can be shown [57] that, in the case of memoryless modulation schemes, the following result holds

$$\mathrm{ASEP}_n = \sum_{m=0}^{+\infty} p_{\tilde{m}}(m)\, \mathrm{ASEP}_{n,\mathrm{RAY}}(\sigma^2\, \sigma_m^2) \tag{1.6}$$

where $\mathrm{ASEP}_{n,\mathrm{RAY}}(\sigma^2\, \sigma_m^2)$ is the average SEP (ASEP) for a Rayleigh-fading channel affected by AWGN with variance $\sigma^2\, \sigma_m^2$, which can be (approximatively) expressed [58] as

$$\mathrm{ASEP}_{n,\mathrm{RAY}}(\sigma^2\, \sigma_m^2) = \alpha \left(1 - \sqrt{\frac{\beta\, \sigma_{\tilde{f}_n}^2}{\sigma^2\, \sigma_m^2 + \beta\, \sigma_{\tilde{f}_n}^2}} \right) \tag{1.7}$$

with α and β being modulation-dependent parameters that depend on the constellation size. For instance, in the case of QPSK modulation, it results that $\alpha = 1$ and $\beta = 1/2$.

[5] We have assumed for the sake of simplicity that the noise variances at the relays and at the destination are all equal.

1.3 Performance analysis of the ML detector

The optimum detector makes a decision on $\tilde{\mathbf{a}}$ based on the observation of a particular realization $\mathbf{y}$ of the received vector $\tilde{\mathbf{y}}$ in (1.5) such that the probability of correct decision is maximized, provided that the noise pdf parameters λ, Γ, and σ^2 are known exactly.[6] Since $\tilde{\mathbf{a}}$ assumes values in $\mathcal{A}$ with equal probability, under the assumption that the realization $\mathbf{h}$ of the channel vector $\tilde{\mathbf{h}}$ is perfectly known by the destination,[7] optimum detection corresponds [58] to the ML criterion: choose the vector $\mathbf{a}_k$ that maximizes the conditional pdf of $\tilde{\mathbf{y}}$ given that $\tilde{\mathbf{a}} = \mathbf{a}_k$ was transmitted and $\tilde{\mathbf{h}} = \mathbf{h}$, which is denoted as $f_{\tilde{\mathbf{y}} \,|\, \tilde{\mathbf{a}}, \tilde{\mathbf{h}}}(\mathbf{y} \,|\, \mathbf{a}_k, \mathbf{h})$. Since $f_{\tilde{\mathbf{y}} \,|\, \tilde{\mathbf{a}}, \tilde{\mathbf{h}}}(\mathbf{y} \,|\, \mathbf{a}_k, \mathbf{h}) = f_{\tilde{\mathbf{d}}}(\mathbf{y} - \boldsymbol{\mathcal{C}}_k \, \mathbf{h})$, one has the decision rule

$$\widehat{\mathbf{a}}_{\mathrm{ml}} \;=\; \arg \max_{k \in \{1,2,\ldots,|\mathcal{A}|\}} \prod_{p=1}^{P} \sum_{m_p=0}^{+\infty} \frac{p_{\widetilde{m}_p}(m_p)}{\pi \, \sigma^2 \, \sigma_{m_p}^2} \exp \left\{ - \frac{|\{\mathbf{y} - \boldsymbol{\mathcal{C}}_k \, \mathbf{h}\}_p|^2}{\sigma^2 \, \sigma_{m_p}^2} \right\} . \tag{1.8}$$

For practical implementations, it is customary to resort to the *normalized* M-term truncation $\widehat{f}_{\tilde{d}_p}(d_p)$ of the pdf given in (1.2) (see [60] for details), which converges pointwise to $f_{\tilde{d}_p}(d_p)$ as $M \to +\infty$. Starting from $\widehat{f}_{\tilde{d}_p}(d_p)$, the infinite series in (1.8) is replaced with a sum having only M terms. Performance measures of the ML decoder are $\mathrm{ASEP}_{\mathrm{ml}} \triangleq \mathrm{E}[\mathrm{SEP}_{\mathrm{ml}}(\tilde{\mathbf{h}})]$, where $\mathrm{SEP}_{\mathrm{ml}}(\tilde{\mathbf{h}})$ is the SEP at the output of the ML decoder [58], conditioned on $\tilde{\mathbf{h}}$, and $\mathrm{APEP}_{\mathrm{ml}} \triangleq \mathrm{E}\left[\mathrm{PEP}_{\mathrm{ml}}(\tilde{\mathbf{h}})\right]$, where $\mathrm{PEP}_{\mathrm{ml}}(\tilde{\mathbf{h}}) \triangleq P(\{\mathbf{a}_k \to \mathbf{a}_\ell\}_{\mathrm{ml}} \,|\, \tilde{\mathbf{h}})$ is the pairwise error probability (PEP) of the ML detector [21], conditioned on $\tilde{\mathbf{h}}$, i.e., the probability that $\mathbf{a}_\ell$ is detected at the destination when $\mathbf{a}_k$ was transmitted. Due to the awkward expression of the ML decision rule (1.8), exact computation of $\mathrm{ASEP}_{\mathrm{ml}}$ and $\mathrm{APEP}_{\mathrm{ml}}$ is very difficult, even when union bounding techniques are used. However, with reference to a MIMO system with co-located antennas, it has been numerically shown in [43] that the

[6] The expectation-maximization algorithm can be used [59] to derive estimates for the parameters of the MCA noise model.

[7] The relevant channel vector realization $\mathbf{h}$ can be estimated at the destination by allowing each data transmission in Phase II be preceded by a training period, wherein all the active relays transmit a symbol sequence known to the destination; the signature vectors used during the training phase will be maintained in the subsequent data transmission.

ASEP performance of the ML detector (1.8) is very similar to that of the *ideal* ML (IML) detector, which has perfect knowledge of the realization of $\widetilde{\mathbf{m}} \triangleq [\widetilde{m}_1, \widetilde{m}_2, \ldots, \widetilde{m}_P]^T \in \mathbb{N}^P$.[8] For the distributed framework at hand, this behavior is confirmed by the simulation results in Section 1.5. Let $\boldsymbol{\Sigma}_{\mathbf{m}} \triangleq \mathrm{diag}(\sigma^2_{m_1}, \sigma^2_{m_2}, \ldots, \sigma^2_{m_P}) \in \mathbb{R}^{P\times P}$, the IML criterion amounts to choosing the vector $\mathbf{a}_k$ that maximizes the conditional pdf of $\boldsymbol{\Sigma}_{\mathbf{m}}^{-1/2}\,\tilde{\mathbf{y}}$ given that $\tilde{\mathbf{a}} = \mathbf{a}_k$ was transmitted, $\tilde{\mathbf{h}} = \mathbf{h}$ was acquired, and $\widetilde{\mathbf{m}} = \mathbf{m} \triangleq [m_1, m_2, \ldots, m_P] \in \mathbb{N}^P$. Since $\boldsymbol{\Sigma}_{\mathbf{m}}^{-1/2}\,\tilde{\mathbf{d}} \sim \mathcal{CN}(\mathbf{0}_P, \sigma^2\,\mathbf{I}_P)$, the IML decision rule ends up to

$$\widehat{\mathbf{a}}_{\mathrm{iml}} = \arg \min_{k\in\{1,2,\ldots,|\mathcal{A}|\}} (\mathbf{y} - \boldsymbol{\mathcal{C}}_k\,\mathbf{h})^H\,\boldsymbol{\Sigma}_{\mathbf{m}}^{-1}\,(\mathbf{y} - \boldsymbol{\mathcal{C}}_k\,\mathbf{h}) \tag{1.9}$$

whose PEP is simpler to analyze than that of (1.8). Let $\mathrm{PEP}_{\mathrm{iml}}(\tilde{\mathbf{h}}, \tilde{\mathbf{m}}) \triangleq P(\{\mathbf{a}_k \to \mathbf{a}_\ell\}_{\mathrm{iml}} \,|\, \tilde{\mathbf{h}}, \widetilde{\mathbf{m}})$ be the PEP, conditioned on $\tilde{\mathbf{h}}$ and $\widetilde{\mathbf{m}}$, at the output of the IML decoder, it can be analytically shown that $\mathrm{PEP}_{\mathrm{iml}}(\mathbf{h}, \mathbf{m}) \leq \mathrm{PEP}_{\mathrm{ml}}(\mathbf{h})$ for $\tilde{\mathbf{h}} = \mathbf{h}$ and $\widetilde{\mathbf{m}} = \mathbf{m}$, which is the consequence of the fact that, with respect to the ML case, the IML detector utilizes the additional knowledge of $\widetilde{\mathbf{m}} = \mathbf{m}$. As previously announced, our simulation results show that $\mathrm{APEP}_{\mathrm{iml}} \triangleq \mathrm{E}\left[\mathrm{PEP}_{\mathrm{iml}}(\tilde{\mathbf{h}}, \tilde{\mathbf{m}})\right]$ turns out to be an approximation of $\mathrm{APEP}_{\mathrm{ml}}$, and not necessarily a lower bound. From (1.9), the PEP at output of the IML decoder is given by

$$\begin{aligned}\mathrm{PEP}_{\mathrm{iml}}(\mathbf{h}, \mathbf{m}) &= \mathrm{Q}\left(\frac{\|\boldsymbol{\Sigma}_{\mathbf{m}}^{-1/2}\,\boldsymbol{\mathcal{C}}_{k,\ell}\,\mathbf{h}\|}{\sqrt{2\,\sigma^2}}\right) \\ &= \frac{1}{\pi}\int_0^{\pi/2} \exp\left(-\frac{\mathbf{h}^H\,\boldsymbol{\mathcal{C}}_{k,\ell}^H\,\boldsymbol{\Sigma}_{\mathbf{m}}^{-1}\,\boldsymbol{\mathcal{C}}_{k,\ell}\,\mathbf{h}}{4\,\sigma^2\sin^2\theta}\right)\,\mathrm{d}\theta\end{aligned} \tag{1.10}$$

where the last equality is the consequence of a change of variables from rectangular to polar coordinates in the integral defining the Q-function. Recalling that $\tilde{\mathbf{h}} = \tilde{\boldsymbol{\mathcal{R}}}\,\tilde{\mathbf{S}}\,\tilde{\mathbf{g}}$, we keep the signature matrix $\tilde{\boldsymbol{\mathcal{R}}}$ fixed, i.e., $\tilde{\boldsymbol{\mathcal{R}}} = \boldsymbol{\mathcal{R}}$, with $\boldsymbol{\mathcal{R}} \in \mathbb{C}^{L\times(N_{\max}+1)}$ being a certain matrix with $R_{\max} \triangleq \mathrm{rank}(\boldsymbol{\mathcal{R}}) = \min(L, N_{\max}+1)$, and we average $\mathrm{PEP}_{\mathrm{iml}}(\tilde{\mathbf{h}}, \tilde{\mathbf{m}})$ over all the realizations of $\tilde{\mathbf{s}} \triangleq [\tilde{s}_1, \tilde{s}_2, \ldots, \tilde{s}_{N_{\max}}]^T \in \mathbb{R}^{N_{\max}}$ (which collects the random diagonal entries of $\tilde{\mathbf{S}}$), $\tilde{\mathbf{g}}$, and $\widetilde{\mathbf{m}}$.

[8] Such a detector is ideal since knowledge or estimation of a particular realization of $\widetilde{\mathbf{m}}$ is unrealistic and, for such a reason, it has been referred to as genie-aided detector in [43].

In the sequel, we first study the performance of the IML detector in the high-SNR regime by evaluating the asymptotic diversity order, and, then, we focus on its achievable finite-SNR diversity order.

1.3.1 Analysis of the IML detector in the high-SNR region

Let $\mathbf{S} \triangleq \mathrm{diag}(1, s_1, s_2, \ldots, s_{N_{\max}}) \in \mathbb{R}^{(N_{\max}+1)\times(N_{\max}+1)}$ be a realization of the matrix $\tilde{\mathbf{S}}$, with $\sum_{n=1}^{N_{\max}} s_n = N(\mathbf{s})$, where the vector $\mathbf{s} \triangleq [s_1, s_2, \ldots, s_{N_{\max}}]^T \in \mathbb{R}^{N_{\max}}$ is the corresponding realization of $\tilde{\mathbf{s}}$, i.e., only $N(\mathbf{s}) \leq N_{\max}$ relays are active in Phase II, for sufficiently high (but finite) SNR values, the ASEP at the output of the IML detector, given $\tilde{\boldsymbol{\mathcal{R}}} = \boldsymbol{\mathcal{R}}$ and $\tilde{\mathbf{s}} = \mathbf{s}$, can be approximated (see, e.g., [58]) as

$$\mathrm{ASEP}_{\mathrm{iml}}(\boldsymbol{\mathcal{R}}, \mathbf{s}) \approx N_e \cdot \max_{\substack{k,\ell \in \{1,2,\ldots,|\mathcal{A}|\} \\ \ell \neq k}} \mathrm{E}_{\tilde{\mathbf{m}}\,|\,\tilde{\mathbf{s}}=\mathbf{s},\tilde{\boldsymbol{\mathcal{R}}}=\boldsymbol{\mathcal{R}}} \left\{ \mathrm{E}_{\tilde{\mathbf{g}}\,|\,\tilde{\mathbf{m}},\tilde{\mathbf{s}}=\mathbf{s},\tilde{\boldsymbol{\mathcal{R}}}=\boldsymbol{\mathcal{R}}} \left[\mathrm{PEP}_{\mathrm{iml}}(\tilde{\mathbf{h}}, \tilde{\mathbf{m}}) \right] \right\} \quad (1.11)$$

where N_e is the average number of minimum-distance neighbors for $\mathcal{A}$.

The following theorem holds:

Theorem 1 (*IML ASEP for a fixed number of active relays*)**.** Let us assume without loss of generality that $P \geq L$ and the diagonal entries of $\boldsymbol{\Sigma}_{\tilde{\mathbf{g}}}$ are arranged in increasing order, i.e., $\sigma^2_{\tilde{g}_0} \leq \sigma^2_{\tilde{g}_1} \leq \cdots \leq \sigma^2_{\tilde{g}_N}$, and define the average SNR as $\gamma \triangleq 1/\sigma^2$. It results that

$$\mathrm{ASEP}_{\mathrm{iml}}(\boldsymbol{\mathcal{R}}, \mathbf{s}) \lessapprox \Upsilon(N(\mathbf{s})) \left[\prod_{r=1}^{R(\mathbf{s})} \frac{1}{\mu_r(\mathbf{S}\,\boldsymbol{\mathcal{R}}^H \boldsymbol{\mathcal{R}}\,\mathbf{S})} \right] \gamma^{-R(\mathbf{s})} \quad (1.12)$$

where $R(\mathbf{s}) \triangleq \mathrm{rank}(\boldsymbol{\mathcal{R}}\,\mathbf{S}) = \min(L, N(\mathbf{s}) + 1)$ and

$$\Upsilon(N(\mathbf{s})) \triangleq N_e\, \Theta \left[\prod_{r=N(\mathbf{s})-R(\mathbf{s})+1}^{N(\mathbf{s})} \frac{1}{\sigma^2_{\tilde{g}_r}} \right] \cdot \left[\max_{\substack{k,\ell \in \{1,2,\ldots,|\mathcal{A}|\} \\ \ell \neq k}} \prod_{r=L-R(\mathbf{s})+1}^{L} \frac{1}{\mu_r(\boldsymbol{\mathcal{C}}^H_{k,\ell}\,\boldsymbol{\mathcal{C}}_{k,\ell})} \right] \quad (1.13)$$

with $\Theta \triangleq \frac{4^{R(\mathbf{s})}}{\pi} \int_0^{\pi/2} (\sin^2\theta)^{R(\mathbf{s})}\, \mathrm{d}\theta$.

Proof. See Appendix A. □

Theorem 1 shows that the impact of MCA noise on the high-SNR performance of the IML (or ML) detector is similar to that of the Gaussian noise considered in [21]. Strictly speaking, the IML detector is able to completely counteract the "impulsiveness" of the noise in the high-SNR regime. Eq. (1.12) characterizes the performance of the IML detector for a given realization $\mathbf{s}$ of the vector $\tilde{\mathbf{s}}$, which means that the number of active relay is fixed to the value $N(\mathbf{s})$. In order to take into account the randomness in the number of active relays, the next step is to further average (1.12) with respect to $\tilde{\mathbf{s}}$, thus obtaining $\mathrm{ASEP}_{\mathrm{iml}}(\boldsymbol{\mathcal{R}}) \triangleq \mathrm{E}_{\tilde{\mathbf{s}}\,|\,\tilde{\boldsymbol{\mathcal{R}}}=\boldsymbol{\mathcal{R}}}\left[\mathrm{ASEP}_{\mathrm{iml}}(\tilde{\boldsymbol{\mathcal{R}}},\tilde{\mathbf{s}})\right]$. Accounting for the statistical characterization of $\tilde{\mathbf{s}}$ discussed in Section 1.2, one has

$$\mathrm{ASEP}_{\mathrm{iml}}(\boldsymbol{\mathcal{R}}) = \sum_{\mathbf{s}\in\{0,1\}^{N_{\max}}} \left\{ \prod_{n=1}^{N_{\max}} [P(\tilde{s}_n=1)]^{s_n} \cdot [1-P(\tilde{s}_n=1)]^{1-s_n} \right\} \mathrm{ASEP}_{\mathrm{iml}}(\boldsymbol{\mathcal{R}},\mathbf{s}) \quad (1.14)$$

where we recall that $P(\tilde{s}_n=1) = (1-\mathrm{ASEP}_n)^K$, with ASEP_n given by (1.6) and (1.7). To obtain an approximation of $\mathrm{ASEP}_{\mathrm{iml}}(\boldsymbol{\mathcal{R}})$ valid in the high-SNR regime, we observe that, if $\sigma^2\,\sigma_m^2 \ll \beta\,\sigma^2_{\tilde{f}_n}$, which is equivalent to $\gamma \gg \sigma_m^2/(\beta\,\sigma^2_{\tilde{f}_n})$, eq. (1.7) can be approximated [53] as $\mathrm{ASEP}_{n,\mathrm{RAY}}(\sigma^2\,\sigma_m^2) \approx (\alpha\,\sigma_m^2)/(2\,\beta\,\gamma\,\sigma^2_{\tilde{f}_n})$, for any[9] finite values of m. Hence, it follows from (1.4) and (1.6) that

$$\mathrm{ASEP}_n \approx \frac{\alpha}{2\,\beta\,\gamma\,\sigma^2_{\tilde{f}_n}} \frac{\mathrm{E}[\tilde{m}]\,\lambda^{-1}+\Gamma}{1+\Gamma} = \frac{\alpha}{2\,\beta\,\gamma\,\sigma^2_{\tilde{f}_n}} \quad (1.15)$$

where we have also used the fact that $\mathrm{E}[\tilde{m}] = \lambda$. Furthermore, at high SNR, it holds that $(1-\mathrm{ASEP}_n)^K \approx 1 - K\,\mathrm{ASEP}_n \approx 1$ and $1-(1-\mathrm{ASEP}_n)^K \approx K\,\mathrm{ASEP}_n$. Consequently, owing also to (1.12), the following upper bound on (1.14) can be written in the high-SNR

[9] If λ is small, the first few terms of the infinite sum in (1.6) dominates the value of ASEP_n.

region

$$\begin{aligned}\mathrm{ASEP}_{\mathrm{iml}}(\boldsymbol{\mathcal{R}}) \lessapprox & \sum_{\mathbf{s}\in\{0,1\}^{N_{\max}}} \left\{ \prod_{n=1}^{N_{\max}} \left[\frac{\alpha\, K}{2\,\beta\,\sigma^2_{\tilde{f}_n}} \right]^{1-s_n} \right\} \Upsilon(N(\mathbf{s})) \\ & \cdot \left[\prod_{r=1}^{R(\mathbf{s})} \frac{1}{\mu_r(\mathbf{S}\,\boldsymbol{\mathcal{R}}^H \boldsymbol{\mathcal{R}}\,\mathbf{S})} \right] \gamma^{-[R(\mathbf{s})+N_{\max}-N(\mathbf{s})]} \\ & = \sum_{n=0}^{N_{\max}} \mathrm{ASEP}^{(n)}_{\mathrm{iml}}(\boldsymbol{\mathcal{R}})\, \gamma^{-[\min(L,n+1)+N_{\max}-n]} \end{aligned} \tag{1.16}$$

where

$$\begin{aligned}\mathrm{ASEP}^{(n)}_{\mathrm{iml}}(\boldsymbol{\mathcal{R}}) \triangleq \Upsilon(n) & \left(\frac{\alpha\, K}{2\,\beta\,\sigma^2_{\tilde{f}_n}} \right)^{N_{\max}-n} \\ & \cdot \sum_{\substack{\mathbf{s}\,\in\,\{0,1\}^{N_{\max}} \\ \text{with } N(\mathbf{s})=n}} \left[\prod_{r=1}^{R(\mathbf{s})} \frac{1}{\mu_r(\mathbf{S}\,\boldsymbol{\mathcal{R}}^H \boldsymbol{\mathcal{R}}\,\mathbf{S})} \right] . \end{aligned} \tag{1.17}$$

The upper bound in (1.16) is expressed as a power sum in the average SNR γ, where the nth coefficient $\mathrm{ASEP}^{(n)}_{\mathrm{iml}}(\boldsymbol{\mathcal{R}})$ collects all the other relevant parameters for the $\binom{N_{\max}}{n}$ different network configurations with n active relays. Specifically, when $L \geq N_{\max}+1$, one has that $R_{\max} = N_{\max}+1$, hence it follows from (1.16) that $\min(L, n+1) + N_{\max} - n = N_{\max}+1$, for each $n \in \{0, 1, \ldots, N_{\max}\}$, thus obtaining

$$\mathrm{ASEP}_{\mathrm{iml}}(\boldsymbol{\mathcal{R}}) \lessapprox \left[\sum_{n=0}^{N_{\max}} \mathrm{ASEP}^{(n)}_{\mathrm{iml}}(\boldsymbol{\mathcal{R}}) \right] \gamma^{-(N_{\max}+1)} . \tag{1.18}$$

In this case, the asymptotic diversity order of the IML detector is equal to $R_{\max}$, i.e., the rank of the signature matrix $\boldsymbol{\mathcal{R}}$, which coincides with the number of potential relays plus one. On the other hand, when $L < N_{\max}+1$, one has $R_{\max} = L$, hence eq. (1.16) can be rewritten as

$$\mathrm{ASEP}_{\mathrm{iml}}(\boldsymbol{\mathcal{R}}) \lessapprox \mathrm{ASEP}^{(N_{\max})}_{\mathrm{iml}}(\boldsymbol{\mathcal{R}})\, \gamma^{-L} + o(\gamma^{-L}) . \tag{1.19}$$

The asymptotic diversity order of the IML detector is now equal to L, i.e., the rank of $\boldsymbol{\mathcal{R}}$, which is equal to the number of virtual antennas

in the underlying space-time code. Therefore, we can conclude that the asymptotic diversity order of the system is always given by $R_{\max} = \min(L, N_{\max}+1)$.

Eqs. (1.18) and (1.19) additionally show that the randomness in the number of active relays affects the coding gain of the system only when $L \geq N_{\max}+1$. Indeed, in the case of $L < N_{\max}+1$, the coding gain is the same of the case when *all* the potential relays are active in Phase II and depends on the nonzero eigenvalues of $\boldsymbol{\mathcal{R}}^H\boldsymbol{\mathcal{R}}$; in such a case, the coding gain is maximized when the product of the nonzero eigenvalues of $\boldsymbol{\mathcal{R}}^H\boldsymbol{\mathcal{R}}$ is maximized, which is tantamount to solving the constrained optimization problem

$$\boldsymbol{\mathcal{R}}_{\text{opt}} = \arg \max_{\boldsymbol{\mathcal{R}} \in \mathbb{C}^{L\times(N_{\max}+1)}} \prod_{r=1}^{R_{\max}} \mu_r(\boldsymbol{\mathcal{R}}^H\boldsymbol{\mathcal{R}}) \tag{1.20}$$

subject to $\text{trace}(\boldsymbol{\mathcal{R}}^H\boldsymbol{\mathcal{R}}) = \rho > 0$, where the imposed constraint avoids the trivial solution for which the Frobenius norm of $\boldsymbol{\mathcal{R}}$ is unbounded. Instead, in the case of $L \geq N_{\max}+1$, the coding gain is maximized when the product of the nonzero eigenvalues of $\mathbf{S}\,\boldsymbol{\mathcal{R}}^H\boldsymbol{\mathcal{R}}\,\mathbf{S}$ is maximized for all the possible configurations of active relays, which leads to the following constrained optimization problem

$$\boldsymbol{\mathcal{R}}_{\text{opt}} = \arg \max_{\boldsymbol{\mathcal{R}} \in \mathbb{C}^{L\times(N_{\max}+1)}} \prod_{r=1}^{R(\mathbf{s})} \mu_r(\mathbf{S}\,\boldsymbol{\mathcal{R}}^H\boldsymbol{\mathcal{R}}\,\mathbf{S}) \tag{1.21}$$

subject to $\text{trace}(\mathbf{S}\,\boldsymbol{\mathcal{R}}^H\boldsymbol{\mathcal{R}}\,\mathbf{S}) = \rho\, R(\mathbf{s})/R_{\max}$, for all the $2^{N_{\max}}$ different realizations $\mathbf{s}$ of $\tilde{\mathbf{s}}$. With regard to the solution of (1.20) and (1.21), we give the lemma:

Lemma 1. When $L < N_{\max}+1$ and, thus, $R_{\max} = L$, the solution of (1.20) obeys $\boldsymbol{\mathcal{R}}_{\text{opt}}\,\boldsymbol{\mathcal{R}}_{\text{opt}}^H = (\rho/L)\,\mathbf{I}_L$. On the other hand, when $L \geq N_{\max}+1$ and, thus, $R_{\max} = N_{\max}+1$, the solution of (1.21) is given by $\boldsymbol{\mathcal{R}}_{\text{opt}}^H\,\boldsymbol{\mathcal{R}}_{\text{opt}} = [\rho/(N_{\max}+1)]\,\mathbf{I}_{N_{\max}+1}$.

Proof. See Appendix B. □

It is noteworthy that the signatures (1.20) and (1.21) cannot be chosen by the relays locally, i.e., in a decentralized manner, but they must be assigned to them by a central unit, i.e., in a centralized fashion. To decentralize the coding method, the nth active relay can choose $\tilde{\mathbf{r}}_n$ at

random locally [21], without coordinating with other cooperating relays. The ASEP performance of a randomized scheme can be obtained by evaluating the ensemble average of (1.18) and (1.19) with respect to $\tilde{\boldsymbol{\mathcal{R}}}$. We directly defer to [21] for details on how to explicitly calculate such averages in the case of some specific randomization rules, such as real/complex Gaussian, uniform phase, real/complex spherical distribution, and antenna selection.

1.3.2 Finite-SNR analysis of the IML detector

Numerical results reported in Section 1.5 show that the behavior of the finite-SNR diversity order as a function of γ is not significantly affected by the randomness in the number of active relays for moderate-to-high SNR values. Thus, in order to also simplify the analysis, we refer herein to the case in which all the relays are active in Phase II, i.e., we consider the single realization[10] $\mathbf{s} = \mathbf{1}_{N_{\max}}$ of $\tilde{\mathbf{s}}$. In this case, for a given pair $(\mathbf{a}_k, \mathbf{a}_\ell)$, the finite-SNR diversity order $G_d^{\mathrm{iml}}(\gamma, k, \ell)$ of the IML detector can be obtained from (1.1) where $\mathrm{APEP}(\gamma)$ is replaced with

$$\mathrm{E}_{\tilde{\mathbf{m}}\,|\,\tilde{\mathbf{s}}=\mathbf{1}_{N_{\max}},\tilde{\boldsymbol{\mathcal{R}}}=\boldsymbol{\mathcal{R}}}\left\{\mathrm{E}_{\tilde{\mathbf{g}}\,|\,\tilde{\mathbf{m}},\tilde{\mathbf{s}}=\mathbf{1}_{N_{\max}},\tilde{\boldsymbol{\mathcal{R}}}=\boldsymbol{\mathcal{R}}}\left[\mathrm{PEP}_{\mathrm{iml}}(\tilde{\mathbf{h}},\tilde{\mathbf{m}})\right]\right\}.$$

Accounting for all possible pairwise errors, the finite-SNR diversity order of the IML detector is defined as

$$G_d^{\mathrm{iml}}(\gamma) \triangleq \min_{\substack{k,\,\ell\,\in\,\{1,\,2,\,\ldots,\,|\mathcal{A}|\}\\ \ell\,\neq\,k}} G_d^{\mathrm{iml}}(\gamma, k, \ell) \tag{1.22}$$

whose *exact* expression is given by the following theorem:

Theorem 2 (*IML finite-SNR diversity order*)**.** Let us define $\boldsymbol{\Phi}_{k,\ell} \triangleq \boldsymbol{\mathcal{C}}_{k,\ell}\,\boldsymbol{\mathcal{R}}\,\boldsymbol{\Sigma}_{\tilde{\mathbf{g}}}\,\boldsymbol{\mathcal{R}}^H\boldsymbol{\mathcal{C}}_{k,\ell}^H \in \mathbb{C}^{P\times P}$ and $\boldsymbol{\Lambda}_{\mathbf{m}} \triangleq \mathrm{diag}(\lambda^{m_1}/m_1!, \ldots, \lambda^{m_P}/m_P!) \in$

[10] The generalization of the forthcoming results to an arbitrary realization of the random vector $\tilde{\mathbf{s}}$ is straightforward.

$\mathbb{R}^{P\times P}$. It results that $G_d^{\mathrm{iml}}(\gamma)$ is given by

$$G_d^{\mathrm{iml}}(\gamma) = \min_{\substack{k,\,\ell\,\in\,\{1,\,2,\,\ldots,\,|\mathcal{A}|\} \\ \ell\,\neq\,k}} \frac{\displaystyle\sum_{m_1=0}^{+\infty}\sum_{m_2=0}^{+\infty}\cdots\sum_{m_P=0}^{+\infty} \det(\boldsymbol{\Lambda}_{\mathbf{m}}) \int_0^{\pi/2} u_1(\gamma,\theta,\mathbf{m})\, u_2(\gamma,\theta,\mathbf{m})\,\mathrm{d}\theta}{\displaystyle\sum_{m_1=0}^{+\infty}\sum_{m_2=0}^{+\infty}\cdots\sum_{m_P=0}^{+\infty} \det(\boldsymbol{\Lambda}_{\mathbf{m}}) \int_0^{\pi/2} u_1(\gamma,\theta,\mathbf{m})\,\mathrm{d}\theta} \tag{1.23}$$

with

$$u_1(\gamma,\theta,\mathbf{m}) \triangleq \det{}^{-1}\left(\mathbf{I}_P + \frac{\gamma}{4\,\sin^2\theta}\,\boldsymbol{\Sigma}_{\mathbf{m}}^{-1}\,\boldsymbol{\Phi}_{k,\ell}\right) \tag{1.24}$$

$$u_2(\gamma,\theta,\mathbf{m}) \triangleq \mathrm{trace}\left[\left(\frac{4\,\sin^2\theta}{\gamma}\,\boldsymbol{\Sigma}_{\mathbf{m}} + \boldsymbol{\Phi}_{k,\ell}\right)^{-1}\boldsymbol{\Phi}_{k,\ell}\right] \tag{1.25}$$

where $\mathrm{rank}(\boldsymbol{\Sigma}_{\mathbf{m}}^{-1}\,\boldsymbol{\Phi}_{k,\ell}) = \mathrm{rank}(\boldsymbol{\Phi}_{k,\ell}) = \mathrm{rank}(\boldsymbol{\mathcal{C}}_{k,\ell}\,\boldsymbol{\mathcal{R}}) = R_{\max} \leq P$, provided that $P \geq L$.

Proof. See Appendix C. □

As a first remark regarding Theorem 2, we observe that $\boldsymbol{\Sigma}_{\mathbf{m}} \succeq [\Gamma/(1+\Gamma)]\,\mathbf{I}_P$ and, thus, one gets

$$\left(\frac{4\,\Gamma\,\sin^2\theta}{\gamma\,(1+\Gamma)}\,\mathbf{I}_P + \boldsymbol{\Phi}_{k,\ell}\right)^{-1} \succeq \left(\frac{4\,\sin^2\theta}{\gamma}\,\boldsymbol{\Sigma}_{\mathbf{m}} + \boldsymbol{\Phi}_{k,\ell}\right)^{-1} \tag{1.26}$$

which, along with $\sin^2\theta \geq 0$, implies [61] that

$$u_2(\gamma,\theta,\mathbf{m}) \leq \lim_{\theta\to 0}\,\mathrm{trace}\left\{\left[\frac{4\,\Gamma\,\sin^2\theta}{\gamma\,(1+\Gamma)}\,\mathbf{I}_P + \boldsymbol{\Phi}_{k,\ell}\right]^{-1}\boldsymbol{\Phi}_{k,\ell}\right\}. \tag{1.27}$$

By invoking the limit formula and the properties of the Moore-Penrose inverse [62], one has

$$\begin{aligned} u_2(\gamma,\theta,\mathbf{m}) &\leq \mathrm{trace}\left[\left(\boldsymbol{\Sigma}_{\tilde{\mathbf{g}}}^{1/2}\,\boldsymbol{\mathcal{R}}^H\boldsymbol{\mathcal{C}}_{k,\ell}^H\right)^{\dagger}\left(\boldsymbol{\Sigma}_{\tilde{\mathbf{g}}}^{1/2}\,\boldsymbol{\mathcal{R}}^H\boldsymbol{\mathcal{C}}_{k,\ell}^H\right)\right] \\ &= \mathrm{trace}\left[\left(\boldsymbol{\mathcal{R}}^H\boldsymbol{\mathcal{C}}_{k,\ell}^H\right)^{\dagger}\left(\boldsymbol{\mathcal{R}}^H\boldsymbol{\mathcal{C}}_{k,\ell}^H\right)\right] \\ &= \mathrm{rank}\left[\left(\boldsymbol{\mathcal{R}}^H\boldsymbol{\mathcal{C}}_{k,\ell}^H\right)^{\dagger}\left(\boldsymbol{\mathcal{R}}^H\boldsymbol{\mathcal{C}}_{k,\ell}^H\right)\right] \\ &= \mathrm{rank}(\boldsymbol{\mathcal{C}}_{k,\ell}\,\boldsymbol{\mathcal{R}}) = R_{\max}\,. \end{aligned} \tag{1.28}$$

The first consequence of (1.28) is that $G_d^{\text{iml}}(\gamma) \leq R_{\max}$, where we recall that $R_{\max}$ is the asymptotic diversity order (see Subsection 1.3.1). Moreover, the functions $u_1(\gamma, \theta, \mathbf{m})$ and $u_2(\gamma, \theta, \mathbf{m})$ are non-decreasing and non-increasing, respectively, with respect to $\mathbf{m} = [m_1, m_2, \ldots, m_P] \in \mathbb{N}^P$, i.e., let $\overline{\mathbf{m}} \triangleq [\overline{m}_1, \overline{m}_2, \ldots, \overline{m}_P] \in \mathbb{N}^P$, if $m_p \leq \overline{m}_p$ for $p \in \{1, 2, \ldots, P\}$, then $\mathbf{\Sigma}_{\overline{\mathbf{m}}} \succeq \mathbf{\Sigma}_{\mathbf{m}}$ implying [61] that $u_1(\gamma, \theta, \mathbf{m}) \leq u_1(\gamma, \theta, \overline{\mathbf{m}})$ and $u_2(\gamma, \theta, \mathbf{m}) \geq u_2(\gamma, \theta, \overline{\mathbf{m}})$. With regard to the behavior of $G_d^{\text{iml}}(\gamma)$ for finite values of the SNR, it is seen that $u_1(\gamma, \theta, \mathbf{m})$ is a non-increasing function with respect to γ, i.e., if $\gamma_1 < \gamma_2$, then $u_1(\gamma_1, \theta, \mathbf{m}) \geq u_1(\gamma_2, \theta, \mathbf{m})$; whereas, the function $u_2(\gamma, \theta, \mathbf{m})$ is non-decreasing with respect to γ, i.e., $u_2(\gamma_1, \theta, \mathbf{m}) \leq u_2(\gamma_2, \theta, \mathbf{m})$ if $\gamma_1 < \gamma_2$. In highly-impulsive noise cases, this fact does not allow $G_d^{\text{iml}}(\gamma)$ to monotonously increase for raising values of γ, by leading to a fluctuating trend.

To gain more insight into this behavior, let us consider an M-term truncated version of the MCA noise model, with $M \geq 2$, which has been shown to be a good approximation for several scenarios of interest [60]. In this case, the diversity order (1.23) can be approximated as

$$G_d^{\text{iml}}(\gamma) \approx \min_{\substack{k,\, \ell \in \{1, 2, \ldots, |\mathcal{A}|\} \\ \ell \neq k}} \frac{\displaystyle\sum_{m_1=0}^{M-1} \sum_{m_2=0}^{M-1} \cdots \sum_{m_P=0}^{M-1} \det(\mathbf{\Lambda}_{\mathbf{m}})\, u_1(\gamma, \pi/2, \mathbf{m})\, u_2(\gamma, \pi/2, \mathbf{m})}{\displaystyle\sum_{m_1=0}^{M-1} \sum_{m_2=0}^{M-1} \cdots \sum_{m_P=0}^{M-1} \det(\mathbf{\Lambda}_{\mathbf{m}})\, u_1(\gamma, \pi/2, \mathbf{m})} \tag{1.29}$$

where we have additionally used the trapezoid rule[11] to approximate the integrals in (1.23). Let us consider the cases of near-Gaussian and highly-impulse noise separately.

Near-Gaussian noise case

Under the assumption that $(M-1)/\lambda \ll \Gamma$, i.e., the noise is near Gaussian, it results from (1.4) that

$$\sigma_{m_p}^2 \approx \sigma_0^2 = \frac{\Gamma}{1+\Gamma} \tag{1.30}$$

[11] Let $b > a$ and $f(x) \geq 0$, the following approximation $\int_a^b f(x)\,\mathrm{d}x \approx (1/2)\,(b-a)\,[f(a)+f(b)]$ is called the trapezoid rule.

for each $m_p \in \{0, 1, \ldots, M-1\}$ and $p \in \{1, 2, \ldots, P\}$. Thus, it follows from (1.24), (1.25), and (1.29) that

$$G_d^{\text{iml}}(\gamma) \approx \min_{\substack{k,\,\ell \in \{1,2,\ldots,|\mathcal{A}|\} \\ \ell \neq k}} \text{trace}\left[\left(\frac{4\,\sigma_0^2}{\gamma}\,\mathbf{I}_P + \mathbf{\Phi}_{k,\ell}\right)^{-1} \mathbf{\Phi}_{k,\ell}\right] \tag{1.31}$$

which is a non-decreasing function of the SNR approaching its asymptotic value $R_{\max}$ as $\gamma \to +\infty$.

As a case study, let us assume that: (i) the source and all the relays are (approximatively) at the same location, i.e., $\mathbf{\Sigma}_{\tilde{\mathbf{g}}} = \sigma_{\tilde{g}_0}^2\,\mathbf{I}_{N_{\max}+1}$; (ii) $L \leq N_{\max}+1$ and $\boldsymbol{\mathcal{R}}_{\text{opt}}\,\boldsymbol{\mathcal{R}}_{\text{opt}}^H = (\rho/L)\,\mathbf{I}_L$ (see Lemma 1);[12] (iii) the space-time code is complex orthogonal [31], i.e., $\boldsymbol{\mathcal{C}}^H(\mathbf{a})\,\boldsymbol{\mathcal{C}}(\mathbf{a}) = \|\mathbf{a}\|^2\,\mathbf{I}_L$, $\forall \mathbf{a} \in \mathbb{C}^K - \{\mathbf{0}_K\}$. Under these assumptions, it results that $\mathbf{\Phi}_{k,\ell} = [(\sigma_{\tilde{g}_0}^2\,\rho)/L]\,\boldsymbol{\mathcal{C}}_{k,\ell}\,\boldsymbol{\mathcal{C}}_{k,\ell}^H$, with $L \leq P$, and, hence, it follows from (1.31) that[13]

$$G_d^{\text{iml}}(\gamma) \approx \frac{L\,\tau\,\gamma}{L + \tau\,\gamma}\,, \quad \text{with } \tau \triangleq \frac{\rho\,(1+\Gamma)\,\Delta_{\min}^2\,\sigma_{\tilde{g}_0}^2}{4\,\Gamma} \tag{1.32}$$

where $\Delta_{\min}$ denotes the minimum distance between the blocks of symbols in $\mathcal{A}$. Eq. (1.32) clearly shows that $G_d^{\text{iml}}(\gamma)$ monotonously increases as a function of γ for reaching the asymptotic value $R_{\max} = L$.

Highly-impulsive noise case

Under the assumption that $\lambda\,\Gamma \ll 1$ with $\Gamma < 1$, i.e., the noise is highly impulsive, it results from (1.4) that

$$\sigma_{m_p}^2 \approx \frac{m_p}{\lambda\,(1+\Gamma)} \tag{1.33}$$

for each $m_p \in \{1, 2, \ldots, M-1\}$ and $p \in \{1, 2, \ldots, P\}$. In this case, using (1.33) and neglecting all the summands that tend to zero faster than λ,

[12] The case of $L > N_{\max}+1$ and $\boldsymbol{\mathcal{R}}_{\text{opt}}^H\,\boldsymbol{\mathcal{R}}_{\text{opt}} = [\rho/(N_{\max}+1)]\,\mathbf{I}_{N_{\max}+1}$ can be treated in a similar way.

[13] We have used the three facts that: (i) $(a\,\mathbf{I}_P + \boldsymbol{\mathcal{C}}_{k,\ell}\,\boldsymbol{\mathcal{C}}_{k,\ell}^H)^{-1} = a^{-1}[\mathbf{I}_P - \boldsymbol{\mathcal{C}}_{k,\ell}(\boldsymbol{\mathcal{C}}_{k,\ell}^H\,\boldsymbol{\mathcal{C}}_{k,\ell} + a\,\mathbf{I}_L)^{-1}\boldsymbol{\mathcal{C}}_{k,\ell}^H]$, where a is an arbitrary constant; (ii) $\text{trace}(\boldsymbol{\mathcal{C}}_{k,\ell}\,\boldsymbol{\mathcal{C}}_{k,\ell}^H) = \text{trace}(\boldsymbol{\mathcal{C}}_{k,\ell}^H\,\boldsymbol{\mathcal{C}}_{k,\ell})$; (iii) $\boldsymbol{\mathcal{C}}_{k,\ell}^H\,\boldsymbol{\mathcal{C}}_{k,\ell} = \|\mathbf{a}_k - \mathbf{a}_\ell\|^2\,\mathbf{I}_L$.

the diversity order given by (1.29) can be further approximated as

$$G_d^{\mathrm{iml}}(\gamma) \approx \min_{\substack{k,\,\ell \in \{1,2,\ldots,|\mathcal{A}|\} \\ \ell \neq k}} \frac{u_1(\gamma,\pi/2,\mathbf{0}_P)\,u_2(\gamma,\pi/2,\mathbf{0}_P) + \lambda \sum_{p=1}^{P} u_1(\gamma,\pi/2,\mathbf{e}_p)\,u_2(\gamma,\pi/2,\mathbf{e}_p)}{u_1(\gamma,\pi/2,\mathbf{0}_P) + \lambda \sum_{p=1}^{P} u_1(\gamma,\pi/2,\mathbf{e}_p)} \tag{1.34}$$

where $\mathbf{e}_p \in \mathbb{C}^P$ has the only nonzero entry $\{\mathbf{e}_p\}_p = 1$, for each $p \in \{1,2,\ldots,P\}$. To streamline our analysis, let us focus on the case study considered in Subsection 1.3.2, with the additional assumption that the space-time code is square ($L = P$),[14] i.e., when $\mathbf{\Phi}_{k,\ell} = [(\sigma^2_{\tilde{g}_0}\,\rho)/L]\,\|\mathbf{a}_k - \mathbf{a}_\ell\|^2\,\mathbf{I}_L$. In this case, it can be seen that (1.24) and (1.25) simplifies to

$$u_1(\gamma,\pi/2,\mathbf{e}_p) = \prod_{p=1}^{L} \left(1 + \frac{\rho\,\|\mathbf{a}_k - \mathbf{a}_\ell\|^2\,\sigma^2_{\tilde{g}_0}}{4\,L}\,\frac{\gamma}{\sigma^2_{m_p}}\right)^{-1} \tag{1.35}$$

$$u_2(\gamma,\pi/2,\mathbf{e}_p) = \sum_{p=1}^{L} \left(1 + \frac{4\,L}{\rho\,\|\mathbf{a}_k - \mathbf{a}_\ell\|^2\,\sigma^2_{\tilde{g}_0}}\,\frac{\sigma^2_{m_p}}{\gamma}\right)^{-1} \tag{1.36}$$

for each $p \in \{1,2,\ldots,P\}$. By substituting (1.35) and (1.36) in (1.34), and using (1.33), after some algebraic rearrangements, one has

$$G_d^{\mathrm{iml}}(\gamma) \approx \frac{\dfrac{\tau\,\gamma}{(1+\frac{\tau}{L}\,\gamma)^2} + \dfrac{L\,\lambda}{1+\frac{\tau}{L}\,\lambda\,\Gamma\,\gamma}\left[\dfrac{(L-1)\,\frac{\tau}{L}\,\gamma}{1+\frac{\tau}{L}\,\gamma} + \dfrac{\frac{\tau}{L}\,\lambda\,\Gamma\,\gamma}{1+\frac{\tau}{L}\,\lambda\,\Gamma\,\gamma}\right]}{\dfrac{1}{1+\frac{\tau}{L}\,\gamma} + \dfrac{L\,\lambda}{1+\frac{\tau}{L}\,\lambda\,\Gamma\,\gamma}} \tag{1.37}$$

Example 1. The exact value of $G_d^{\mathrm{iml}}(\gamma)$ in (1.23), and its approximations (1.29) and (1.34), are depicted in Fig. 1.1 (left-side plot) as a function of γ for different STBC rules, with QPSK signaling, i.e.,

[14] With respect to their nonsquare counterparts, square complex orthogonal code matrices require a much smaller processing delay, with the consequence of a slightly smaller maximum code rate [63].

$\tilde{a}_k = \{\pm 1/\sqrt{2} \pm j/\sqrt{2}\}$, for $k \in \{1, 2, \ldots, K\}$, $N_{\max} = L - 1$, $M = 2$, $\lambda = 10^{-3}$, $\Gamma = 0.1$, and $\sigma^2_{\tilde{g}_0} \triangleq d_{\mathrm{SD}}^{-2}$, where $d_{\mathrm{SD}} = 10$ meters is the distance between the source and the destination. Specifically, we considered as STBC rules the full-rate Alamouti complex code [64] of order $L = K = P = 2$, the complex orthogonal code of order $L = K = 3$ with code rate $K/P = 3/4$ [65], and, finally, the complex orthogonal code of order $L = K = 4$ with code rate $K/P = 4/8 = 1/2$ [8, Example 4.7.1]. In all these cases, the asymptotic diversity order is $R_{\max} = L$. It is seen that, for the 2×2 and 4×3 STBC matrices, the diversity order rises and falls between a maximum and a minimum before starting to monotonically increase for reaching the asymptotic values 2 and 3, respectively; such a fluctuating behavior completely disappears in the case of the 8×4 STBC matrix, where $G_d^{\mathrm{iml}}(\gamma)$ monotonously reaches its asymptotic value 4. It can be observed a satisfactory agreement among (1.23), (1.29), and (1.34): with reference to the Alamouti code, the simple formula (1.37), which exactly coincides with (1.34) for $L = P$, accurately captures the behavior of $G_d^{\mathrm{iml}}(\gamma)$, by showing only a slight discrepancy in the neighborhood of the local minimum.

After some straightforward but tedious calculations, it is shown that $G_d^{\mathrm{iml}}(\gamma)$ given by (1.37) has local maximum and minimum points at

$$\gamma_{\max}^{\mathrm{iml}} \approx \frac{L}{\tau\sqrt{\lambda}} \quad \text{and} \quad \gamma_{\min}^{\mathrm{iml}} \approx \frac{\sqrt{L}}{\lambda\,\tau\,\sqrt{\Gamma}} \tag{1.38}$$

respectively, which allow to directly link the extrema of $G_d^{\mathrm{iml}}(\gamma)$ to the parameters of noise and STBC. In the case of the Alamouti code (see Example 1), eq. (1.38) gives $\gamma_{\max}^{\mathrm{iml}} = 24.56$ dB and $\gamma_{\min}^{\mathrm{iml}} = 43$ dB, whereas their corresponding exact values numerically obtained from (1.23) are 24 dB and 42 dB, respectively.

1.4 Performance analysis of the MD detector

The diversity scheme considered in Section 1.3 requires that the destination node implements the decision rule (1.8) for ML detection of $\tilde{\mathbf{a}}$, by resorting to the M-term truncation of the noise pdf. For those systems with simple terminal units such as wireless sensor networks and practical *ad hoc* or multihop wireless networks, this processing may be too computationally expensive for large value of K, M, P, and/or $|\mathcal{A}|$.

Herein, we investigate the performance of a suboptimal scheme, which is based on the MD decision rule and, thus, involves a less processing burden at the destination.

Given $\tilde{\mathbf{h}} = \mathbf{h}$, the MD decision rule is defined as follows

$$\widehat{\mathbf{a}}_{\mathrm{md}} = \arg \min_{k \in \{1,2,\ldots,|\mathcal{A}|\}} \|\mathbf{y} - \boldsymbol{\mathcal{C}}_k \, \mathbf{h}\|^2 \tag{1.39}$$

which turns out to be optimal (in the minimum-error-probability sense) when the noise $\tilde{d}_p$ boils down to a circular symmetric complex Gaussian RV, for each $p \in \{1, 2, \ldots, P\}$. For the noise model at hand, this happens for asymptotically large values of λ and/or Γ.

In what follows, we study the cases of the high- and finite-SNR regimes separately, by again keeping the signature matrix $\tilde{\boldsymbol{\mathcal{R}}}$ fixed to $\boldsymbol{\mathcal{R}}$, with rank $R_{\max} = \min(L, N_{\max} + 1)$.

1.4.1 Analysis of the MD detector in the high-SNR region

As previously done in the IML case, for sufficiently high SNR values, the ASEP at the output of the MD decoder, given $\tilde{\mathbf{s}} = \mathbf{s}$, can be approximatively expressed as

$$\begin{aligned} \mathrm{ASEP}_{\mathrm{md}}(\boldsymbol{\mathcal{R}}, \mathbf{s}) \approx N_e \cdot & \max_{\substack{k, \ell \, \in \, \{1, 2, \ldots, |\mathcal{A}|\} \\ \ell \neq k}} \\ & \mathrm{E}_{\widetilde{\mathbf{m}} \,|\, \tilde{\mathbf{s}} = \mathbf{s}, \tilde{\boldsymbol{\mathcal{R}}} = \boldsymbol{\mathcal{R}}} \left\{ \mathrm{E}_{\tilde{\mathbf{g}} \,|\, \widetilde{\mathbf{m}}, \tilde{\mathbf{s}} = \mathbf{s}, \tilde{\boldsymbol{\mathcal{R}}} = \boldsymbol{\mathcal{R}}} \left[\mathrm{PEP}_{\mathrm{md}}(\tilde{\mathbf{h}}, \tilde{\mathbf{m}}) \right] \right\} \end{aligned} \tag{1.40}$$

where, from (1.39), we have that $\mathrm{PEP}_{\mathrm{md}}(\tilde{\mathbf{h}}, \tilde{\mathbf{m}}) \triangleq P(\{\mathbf{a}_k \to \mathbf{a}_\ell\}_{\mathrm{md}} \,|\, \tilde{\mathbf{h}}, \widetilde{\mathbf{m}})$, conditioned on $\tilde{\mathbf{h}} = \mathbf{h}$ and $\widetilde{\mathbf{m}} = \mathbf{m}$, is given by

$$\begin{aligned} \mathrm{PEP}_{\mathrm{md}}(\mathbf{h}, \mathbf{m}) &= \mathrm{Q}\left(\frac{\|\boldsymbol{\mathcal{C}}_{k,\ell} \, \mathbf{h}\|^2}{\sqrt{2\,\sigma^2} \, \|\boldsymbol{\Sigma}_{\mathbf{m}}^{1/2} \, \boldsymbol{\mathcal{C}}_{k,\ell} \, \mathbf{h}\|} \right) \leq \mathrm{Q}\left(\frac{\|\boldsymbol{\mathcal{C}}_{k,\ell} \, \mathbf{h}\|}{\sqrt{2\,\sigma^2 \, \mu_1(\boldsymbol{\Sigma}_{\mathbf{m}})}} \right) \\ &= \frac{1}{\pi} \int_0^{\pi/2} \exp\left(- \frac{\mathbf{h}^H \, \boldsymbol{\mathcal{C}}_{k,\ell}^H \, \boldsymbol{\mathcal{C}}_{k,\ell} \, \mathbf{h}}{4\,\sigma^2 \, \mu_1(\boldsymbol{\Sigma}_{\mathbf{m}}) \, \sin^2 \theta} \right) \mathrm{d}\theta \end{aligned} \tag{1.41}$$

where the Rayleigh-Ritz inequality $\|\boldsymbol{\Sigma}_{\mathbf{m}}^{1/2} \, \boldsymbol{\mathcal{C}}_{k,\ell} \, \mathbf{h}\|^2 \leq \mu_1(\boldsymbol{\Sigma}_{\mathbf{m}}) \, \|\boldsymbol{\mathcal{C}}_{k,\ell} \, \mathbf{h}\|^2$ has been invoked [61]. It is noteworthy that, by directly comparing (1.10) and (1.41), it results that, if the number of impulses affecting the destination is identical in each symbol period, i.e., $\boldsymbol{\Sigma}_{\mathbf{m}} = \sigma_{m_1}^2 \, \mathbf{I}_P$, the

MD detector has the same PEP performance of the IML one. More generally, it results that $\mathrm{PEP}_{\mathrm{ml}}(\mathbf{h}) \leq \mathrm{PEP}_{\mathrm{md}}(\mathbf{h}, \mathbf{m})$, which is a consequence of the fact that the ML detector minimizes the probability of error when the specific realization of $\widetilde{\mathbf{m}}$ is unknown. Given $\tilde{\boldsymbol{\mathcal{R}}} = \boldsymbol{\mathcal{R}}$ and $\tilde{\mathbf{s}} = \mathbf{s}$, the ASEP performance of the MD detector in the high-SNR region is given by the theorem:

Theorem 3 (*MD ASEP for a fixed number of active relays)***.** Under the same assumptions of Theorem 1, it results that

$$\mathrm{ASEP}_{\mathrm{md}}(\boldsymbol{\mathcal{R}}, \mathbf{s}) \lessapprox \Psi(\lambda, R(\mathbf{s}))\, \Upsilon(N(\mathbf{s})) \cdot \left[\prod_{r=1}^{R(\mathbf{s})} \frac{1}{\mu_r(\mathbf{S}\, \boldsymbol{\mathcal{R}}^H \boldsymbol{\mathcal{R}}\, \mathbf{S})}\right] \gamma^{-R(\mathbf{s})} \quad (1.42)$$

where

$$\Psi(\lambda, R(\mathbf{s})) \triangleq P\, \mathrm{E}\left[\left(\frac{\widetilde{m}_p\, \lambda^{-1} + \Gamma}{1 + \Gamma}\right)^{R(\mathbf{s})}\right] \quad (1.43)$$

whereas $\Upsilon(N(\mathbf{s}))$ and γ have been defined in Theorem 1.

Proof. See Appendix D. □

It is apparent from Theorems 1 and 3 that the upper bounds (1.12) and (1.42) on the ASEP performance of the IML and MD detectors, respectively, differ only for the presence of the function $\Psi(\lambda, R(\mathbf{s}))$. Therefore, following the same steps done in Subsection 1.3.1, one obtains

$$\begin{aligned}\mathrm{ASEP}_{\mathrm{md}}(\boldsymbol{\mathcal{R}}) &\triangleq \mathrm{E}_{\tilde{\mathbf{s}}\,|\,\tilde{\boldsymbol{\mathcal{R}}}=\boldsymbol{\mathcal{R}}}\left[\mathrm{ASEP}_{\mathrm{md}}(\tilde{\boldsymbol{\mathcal{R}}}, \tilde{\mathbf{s}})\right] \\ &\lessapprox \sum_{n=0}^{N_{\max}} \mathrm{ASEP}_{\mathrm{md}}^{(n)}(\boldsymbol{\mathcal{R}})\, \gamma^{-[\min(L, n+1)+N_{\max}-n]} \end{aligned} \quad (1.44)$$

where $\mathrm{ASEP}_{\mathrm{md}}^{(n)}(\boldsymbol{\mathcal{R}}) \triangleq \Psi(\lambda, R(\mathbf{s}))\, \mathrm{ASEP}_{\mathrm{iml}}^{(n)}(\boldsymbol{\mathcal{R}})$, which, compared to (1.16), shows that the IML and MD detectors have the same asymptotic diversity order $R_{\max}$ but different coding gains. In particular, it is shown in [43, Appendix I] that $\Psi(\lambda, R(\mathbf{s})) \geq 1$ and, additionally, that the function $\Psi(\lambda, R(\mathbf{s}))$ is monotonically decreasing in λ and monotonically increasing in $R(\mathbf{s})$. In other words, the coding gain of the MD detector is smaller than or equal to that of the IML one and the performance

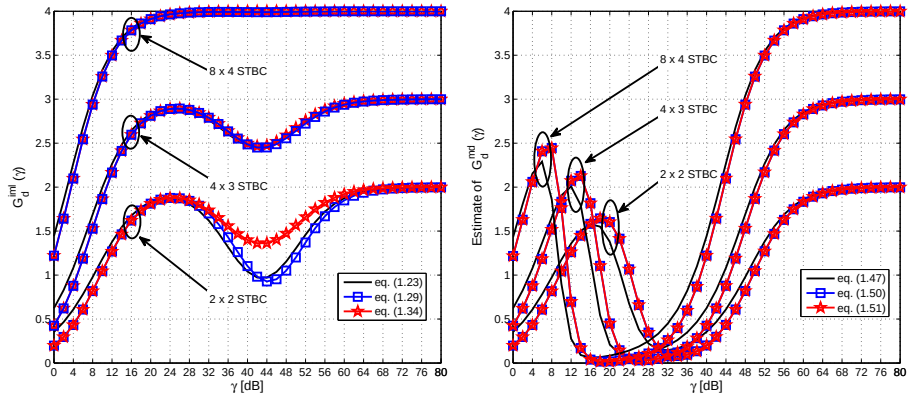

Figure 1.1: Very highly-impulsive noise: Diversity orders $G_d^{\rm iml}(\gamma)$ (left-side plot) and $\widehat{G}_d^{\rm md}(\gamma)$ (right-side plot) versus γ for different STBC rules (Examples 1 and 2: QPSK signaling, $N_{\max} = L-1$, $M=2$, $\lambda = 10^{-3}$, $\Gamma = 0.1$, and $\sigma^2_{\tilde{g}_0} \triangleq 10^{-2}$).

penalty enlarges for increasing values of $R(\mathbf{s})$; on the other hand, for a fixed value of $R(\mathbf{s})$, such a penalty is negligible in the case of near Gaussian noise, i.e., for high values of λ, while it becomes significant if the noise is highly impulsive, i.e., for small values of λ. However, the signature matrix $\boldsymbol{\mathcal{R}}_{\rm opt}$ given by (1.20) and (1.21) also maximizes the coding gain of the system with MD detection at the destination when $L < N_{\max}+1$ and $L \geq N_{\max}+1$, respectively. The ASEP performance of a randomized scheme with a specific probability distribution directly follows from (1.44) by using the results of [21].

1.4.2 Finite-SNR analysis of the MD detector

As done for the IML detector in Subsection 1.3.2, the finite-SNR performance of the MD detector is evaluated by considering the single realization $\mathbf{s} = \mathbf{1}_{N_{\max}}$ of the vector $\tilde{\mathbf{s}}$. In this case, for a given pair $(\mathbf{a}_k, \mathbf{a}_\ell)$, the exact expression of the finite-SNR diversity order $G_d^{\rm md}(\gamma, k, \ell)$ can be obtained from (1.1) where APEP(γ) is replaced with

$$\mathrm{E}_{\tilde{\mathbf{m}}\,|\,\mathbf{s}=\mathbf{1}_{N_{\max}},\tilde{\boldsymbol{\mathcal{R}}}=\boldsymbol{\mathcal{R}}} \left\{ \mathrm{E}_{\tilde{\mathbf{g}}\,|\,\tilde{\mathbf{m}},\mathbf{s}=\mathbf{1}_{N_{\max}},\tilde{\boldsymbol{\mathcal{R}}}=\boldsymbol{\mathcal{R}}} \left[\mathrm{PEP}_{\rm md}(\tilde{\mathbf{h}}, \tilde{\mathbf{m}}) \right] \right\} .$$

In this respect, by resorting to the upper bound in (1.41), we observe that

$$\begin{aligned}&\mathrm{E}_{\tilde{\mathbf{m}}\,|\,\mathbf{s}=\mathbf{1}_{N_{\max}},\tilde{\boldsymbol{\mathcal{R}}}=\boldsymbol{\mathcal{R}}}\left\{\mathrm{E}_{\tilde{\mathbf{g}}\,|\,\tilde{\mathbf{m}},\mathbf{s}=\mathbf{1}_{N_{\max}},\tilde{\boldsymbol{\mathcal{R}}}=\boldsymbol{\mathcal{R}}}\left[\mathrm{PEP}_{\mathrm{md}}(\tilde{\mathbf{h}},\tilde{\mathbf{m}})\right]\right\}\\ &\qquad\leq\frac{P}{\pi}\sum_{m_p=0}^{+\infty}p_{\tilde{m}_p}(m_p)\int_0^{\pi/2}\det{}^{-1}\left(\mathbf{I}_P+\gamma\,\frac{\boldsymbol{\Phi}_{k,\ell}}{4\,\sigma_{m_p}^2\sin^2\theta}\right)\mathrm{d}\theta\end{aligned}\tag{1.45}$$

where we have used (D.1) in Appendix D, with $\boldsymbol{\Phi}_{k,\ell}$ defined in Theorem 2, and the facts that $\mu_1(\boldsymbol{\Sigma}_{\tilde{\mathbf{m}}})=\max(\sigma^2_{\tilde{m}_1},\sigma^2_{\tilde{m}_2},\ldots,\sigma^2_{\tilde{m}_P})$ and the pmf of $\tilde{m}\triangleq\max(\tilde{m}_1,\tilde{m}_2,\ldots,\tilde{m}_P)$ can be upper bounded as in (D.4) in Appendix D. Similarly to (1.22), the finite-SNR diversity order of the MD detector is defined as

$$G_d^{\mathrm{md}}(\gamma)\triangleq\min_{\substack{k,\,\ell\,\in\,\{1,\,2,\,\ldots,\,|\mathcal{A}|\}\\ \ell\,\neq\,k}}G_d^{\mathrm{md}}(\gamma,k,\ell)\,.\tag{1.46}$$

In order to simplify the mathematical derivations, an estimate $\widehat{G}_d^{\mathrm{md}}(\gamma)$ of $G_d^{\mathrm{md}}(\gamma)$ is evaluated in the following theorem by using (1.1) and replacing $\mathrm{APEP}(\gamma)$ with the upper bound in (1.45). The good agreement between $\widehat{G}_d^{\mathrm{md}}(\gamma)$ and $G_d^{\mathrm{md}}(\gamma)$ is demonstrated in Section 1.5 through Monte Carlo simulations.

Theorem 4 (Estimate of the MD finite-SNR diversity order)**.** It results that $\widehat{G}_d^{\mathrm{md}}(\gamma)$ is given by

$$\widehat{G}_d^{\mathrm{md}}(\gamma)=\min_{\substack{k,\,\ell\,\in\,\{1,\,2,\,\ldots,\,|\mathcal{A}|\}\\ \ell\,\neq\,k}}\frac{\displaystyle\sum_{m_p=0}^{+\infty}\frac{\lambda^{m_p}}{m_p!}\int_0^{\pi/2}v_1(\gamma,\theta,m_p)\,v_2(\gamma,\theta,m_p)\,\mathrm{d}\theta}{\displaystyle\sum_{m_p=0}^{+\infty}\frac{\lambda^{m_p}}{m_p!}\int_0^{\pi/2}v_1(\gamma,\theta,m_p)\,\mathrm{d}\theta}\tag{1.47}$$

with

$$v_1(\gamma,\theta,m_p)\triangleq\det{}^{-1}\left(\mathbf{I}_P+\frac{\gamma}{4\,\sigma_{m_p}^2\sin^2\theta}\,\boldsymbol{\Phi}_{k,\ell}\right)\tag{1.48}$$

$$v_2(\gamma,\theta,m_p)\triangleq\mathrm{trace}\left[\left(\frac{4\,\sigma_{m_p}^2\sin^2\theta}{\gamma}\,\mathbf{I}_P+\boldsymbol{\Phi}_{k,\ell}\right)^{-1}\boldsymbol{\Phi}_{k,\ell}\right]\tag{1.49}$$

where $\mathbf{\Phi}_{k,\ell}$ has been defined in Theorem 2.

Proof. The proof is omitted since it can be carried out by proceeding as in Appendix C. □

Similarly to (1.27) and (1.28), it can be shown that $v_2(\gamma, \theta, m_p) \leq R_{\max}$, which implies that $\widehat{G}_d^{\mathrm{md}}(\gamma) \leq R_{\max}$, where $R_{\max}$ is the asymptotic diversity order. Moreover, the functions $v_1(\gamma, \theta, m_p)$ and $v_2(\gamma, \theta, m_p)$ are non-decreasing and non-increasing, respectively, with respect to $m_p \in \mathbb{N}$.

As previously done for the IML detector, we approximate the diversity order (1.47) by considering an M-term truncated version of the MCA noise model, with $M \geq 2$, thus obtaining

$$\widehat{G}_d^{\mathrm{md}}(\gamma) \approx \min_{\substack{k,\,\ell \,\in\, \{1,2,\ldots,|\mathcal{A}|\} \\ \ell \neq k}} \frac{\displaystyle\sum_{m_p=0}^{M-1} \frac{\lambda^{m_p}}{m_p!}\, v_1(\gamma, \pi/2, m_p)\, v_2(\gamma, \pi/2, m_p)}{\displaystyle\sum_{m_p=0}^{M-1} \frac{\lambda^{m_p}}{m_p!}\, v_1(\gamma, \pi/2, m_p)} \tag{1.50}$$

where we have again used the trapezoid rule to approximate the integrals in (1.47). In the sequel, the cases of near-Gaussian and highly-impulse noise are studied separately.

Near-Gaussian noise case

If $(M-1)/\lambda \ll \Gamma$, the approximation (1.30) holds and, then, it follows from (1.48), (1.49), and (1.50) that $\widehat{G}_d^{\mathrm{md}}(\gamma) \approx G_d^{\mathrm{iml}}(\gamma)$, where $G_d^{\mathrm{iml}}(\gamma)$ is given by (1.31). In other words, when the noise is near Gaussian, the MD and IML detectors achieve the same finite-SNR diversity order, which is a monotonous increasing function of the SNR [see also the particular case (1.32)].

Highly-impulsive noise case

If $\lambda\Gamma \ll 1$ with $\Gamma < 1$, approximation (1.33) holds and, hence, neglecting all the summands in (1.50) that tend to zero faster than λ,

one obtains

$$\widehat{G}_d^{\mathrm{md}}(\gamma) \approx \min_{\substack{k,\ell \in \{1,2,\ldots,|\mathcal{A}|\} \\ \ell \neq k}} \frac{v_1(\gamma,\pi/2,0)\, v_2(\gamma,\pi/2,0) + \lambda\, v_1(\gamma,\pi/2,1)\, v_2(\gamma,\pi/2,1)}{v_1(\gamma,\pi/2,0) + \lambda\, v_1(\gamma,\pi/2,1)} \tag{1.51}$$

Under the same assumptions for which (1.35) and (1.36) hold, eqs. (1.48) and (1.49) boil down to[15]

$$v_1(\gamma,\pi/2,m_p) = \left(1 + \frac{\rho\,\|\mathbf{a}_k - \mathbf{a}_\ell\|^2\,\sigma_{\tilde{g}_0}^2}{4\,L}\,\frac{\gamma}{\sigma_{m_p}^2}\right)^{-L} \tag{1.52}$$

$$v_2(\gamma,\pi/2,m_p) = L\left(1 + \frac{4\,L}{\rho\,\|\mathbf{a}_k - \mathbf{a}_\ell\|^2\,\sigma_{\tilde{g}_0}^2}\,\frac{\sigma_{m_p}^2}{\gamma}\right)^{-1}. \tag{1.53}$$

By substituting (1.52) and (1.53) in (1.51), one obtains

$$\widehat{G}_d^{\mathrm{md}}(\gamma) \approx \frac{\dfrac{\tau\,\gamma}{(1+\frac{\tau}{L}\,\gamma)^{L+1}} + \dfrac{\tau\,\lambda^2\,\Gamma\,\gamma}{(1+\frac{\tau}{L}\,\lambda\,\Gamma\,\gamma)^{L+1}}}{\dfrac{1}{(1+\frac{\tau}{L}\,\gamma)^{L}} + \dfrac{\lambda}{(1+\frac{\tau}{L}\,\lambda\,\Gamma\,\gamma)^{L}}}. \tag{1.54}$$

Example 2. The diversity order $\widehat{G}_d^{\mathrm{md}}(\gamma)$ given by (1.47), and its approximations (1.50) and (1.51), are depicted in Fig. 1.1 (right-side plot) as a function of γ, by using the same setting of Example 1. All the curves show a very good agreement between estimated and approximate results. We recall that the simple formula (1.54) exactly coincides with (1.51) for $L = P$. It is apparent that, as in the IML case (see left-side plot of Fig. 1.1), the function $\widehat{G}_d^{\mathrm{md}}(\gamma)$ is characterized by a fluctuating trend. However, $\widehat{G}_d^{\mathrm{md}}(\gamma)$ exhibits wider fluctuations than that of the IML one, which do not smooth as $R_{\max}$ increases, thus deteriorating the system performance; differently from the IML case, it is noteworthy that the diversity order of the MD detector can be smaller than 1 over a wide region of SNR values, i.e., $\widehat{G}_d^{\mathrm{md}}(\gamma) < 1$ for $\gamma_{\mathrm{lower}}^{\mathrm{md}} < \gamma < \gamma_{\mathrm{upper}}^{\mathrm{md}}$.

[15] Additionally, such expressions also hold if the complex orthogonal code matrix is nonsquare, i.e., $L < P$.

Starting from (1.54) and putting aside the threshold $\gamma_{\text{lower}}^{\text{md}}$ that falls into a SNR regime of no practical interest in many communication scenarios, it can be verified that

$$\gamma_{\text{upper}}^{\text{md}} = \frac{L}{\tau\,\lambda\,\Gamma\,(L-1)} \tag{1.55}$$

which diminishes for increasing values of L. In the case of the Alamouti code (Example 1), eq. (1.55) gives $\gamma_{\text{upper}}^{\text{md}} = 49.58$ dB, whereas its corresponding exact value numerically obtained from (1.47) is 50 dB.

1.5 Monte Carlo performance analysis

We present a Monte Carlo numerical analysis of the cooperative schemes considered in Sections 1.3 and 1.4 to validate and complete our theoretical performance analyses, with reference to both centralized and decentralized relaying, denoted with the subscripts "C" and "D" in the plots, respectively. In the former case, the signature matrix $\tilde{\boldsymbol{\mathcal{R}}}$ is chosen according to Lemma 1, i.e., the source and each active relay transmit a preassigned column of the STBC matrix $\boldsymbol{\mathcal{C}}(\tilde{\mathbf{a}})$; in the latter case, $\tilde{\boldsymbol{\mathcal{R}}} = [\rho/(L\,N)]^{1/2}\tilde{\boldsymbol{\mathcal{N}}}$, where the entries of $\tilde{\boldsymbol{\mathcal{N}}} \in \mathbb{C}^{L\times N}$ are i.i.d. $\mathcal{CN}(0,1)$, i.e., the source and each active relay transmit a linear combination of the columns of $\boldsymbol{\mathcal{C}}(\tilde{\mathbf{a}})$ with complex Gaussian coefficients. In all the experiments, we adopted the following simulation setting. All the relay nodes are uniformly and independently distributed in a circle of radius 10 meters centered around the destination node. The distance d_{SD} between the source and the destination is 10 meters, and $\sigma_{\tilde{g}_0}^2 \triangleq d_{\text{SD}}^{-2}$. For $n \in \{1, 2, \ldots, N_{\max}\}$, we assumed that $\sigma_{\tilde{f}_n}^2 \triangleq d_{\text{SR},n}^{-2}$ and $\sigma_{\tilde{g}_n}^2 \triangleq d_{\text{RD},n}^{-2}$, where $d_{\text{SR},n}$ is the distance between the source and the nth relay, whereas $d_{\text{RD},n}$ is the distance between the nth relay and the destination. We simulated three different impulsive noise environments: near-Gaussian with $(\lambda,\Gamma) = (1, 0.1)$, highly-impulsive with $(\lambda,\Gamma) = (10^{-2}, 0.1)$, and very highly-impulsive with $(\lambda,\Gamma) = (10^{-3}, 0.1)$. We studied the performances of ML, IML, and MD detectors in terms of ABER and diversity order as a function of the SNR. As a reference, the ABER of the optimum detector for the classical Rayleigh-fading channel affected by AWGN with variance σ^2, which is referred to as "Gauss" in the plots, was additionally reported. For each of the 10^6 independent Monte Carlo run carried out (wherein, besides the network configuration, channel coefficients,

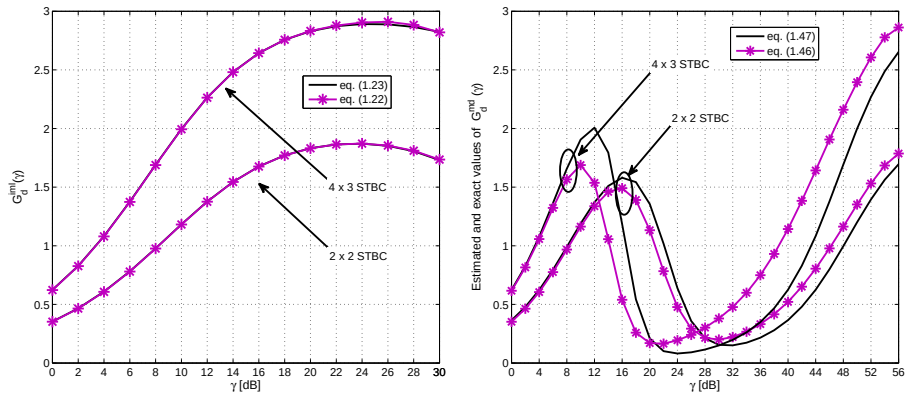

Figure 1.2: Very highly-impulsive noise: Comparison between (1.22)–(1.23) (left-side plot) and (1.46)–(1.47) (right-side plot) versus γ for different STBC rules (Example 3: QPSK signaling, $N_{\max} = L - 1$, $\lambda = 10^{-3}$, $\Gamma = 0.1$, and $\sigma^2_{\tilde{g}_0} \triangleq 10^{-2}$).

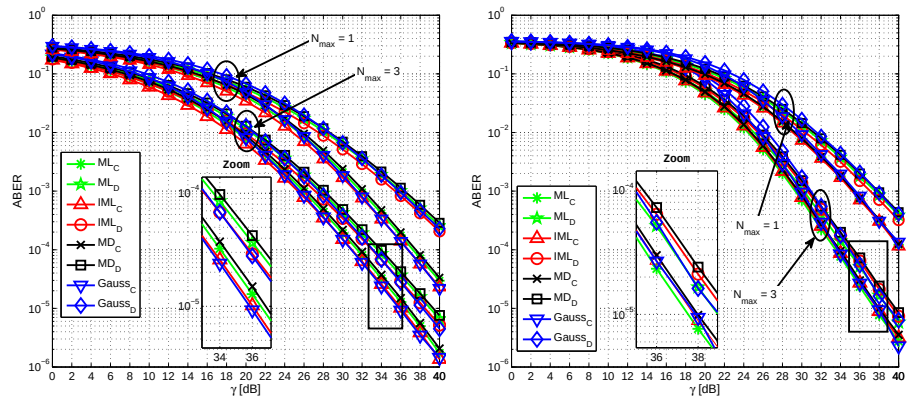

Figure 1.3: Near-Gaussian noise: ABER versus SNR (Example 4: 2×2 Alamouti complex code, $N_{\max} = 1$ and $N_{\max} = 3$ potential relays): in the left-side plot, the number of active relays in Phase II is fixed; in the right-side plot, the number of active relays in Phase II is randomly time-varying.

impulsive noise, data sequences, and randomization coefficients are randomly generated), an independent record of 10^2 symbols was considered to evaluate the ABER and the APEP to be used in (1.1).

Example 3: Finite-SNR diversity order analysis of the IML and MD

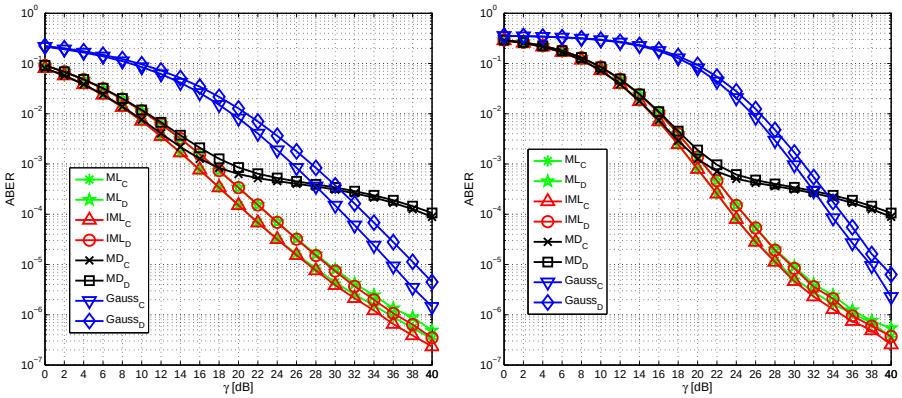

Figure 1.4: Very highly-impulsive noise: ABER versus SNR (Example 4: 2×2 Alamouti complex code and $N_{\max} = 3$ potential relays): in the left-side plot, the number of active relays in Phase II is fixed to 3; in the right-side plot, the number of active relays in Phase II is randomly time-varying.

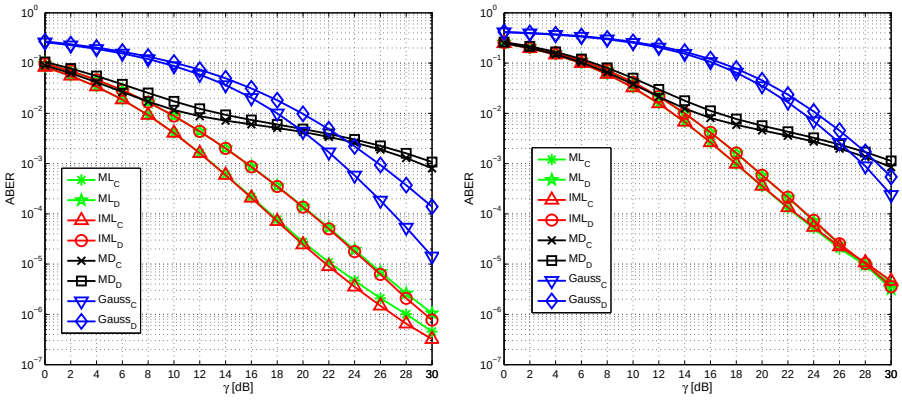

Figure 1.5: Highly-impulsive noise: ABER versus SNR (Example 5: 4×3 complex orthogonal code and $N_{\max} = 2$ potential relays): in the left-side plot, the number of active relays in Phase II is fixed to 2; in the right-side plot, the number of active relays in Phase II is randomly time-varying.

detectors for different STBC rules

In this example, the left-side plot of Fig. 1.2 shows the comparison between the diversity order $G_d^{\text{iml}}(\gamma)$ defined by (1.22), which was evaluated by using (1.1) and averaging the exact expression of $\text{PEP}_{\text{iml}}(\mathbf{h}, \mathbf{m})$

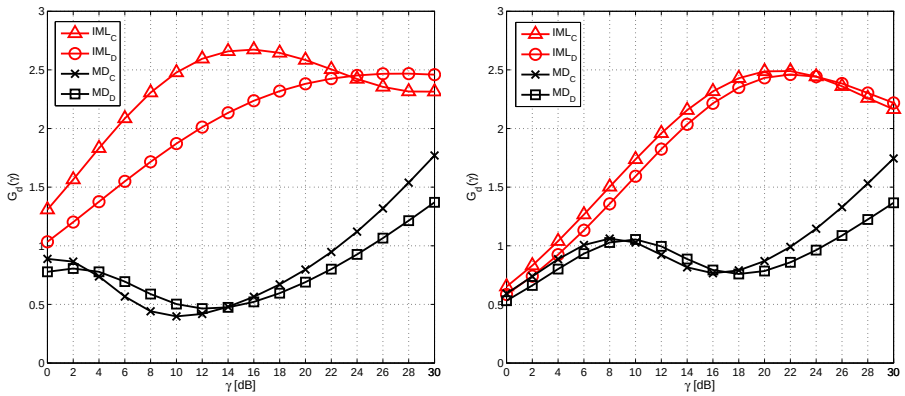

Figure 1.6: Highly-impulsive noise: Diversity order versus SNR (Example 5: 4×3 complex orthogonal code and $N_{\max} = 2$ potential relays): in the left-side plot, the number of active relays in Phase II is fixed to 2; in the right-side plot, the number of active relays in Phase II is randomly time-varying.

reported in (1.10), and its expression given by (1.23). We resorted to the same simulation setting of Examples 1 and 2. It is confirmed that the result (1.23) of Theorem 2 is exact. Additionally, we reported in the right-side plot of Fig. 1.2 the comparison between the estimated diversity order $\widehat{G}_d^{\mathrm{md}}(\gamma)$ (see Theorem 4) and its exact counterpart $G_d^{\mathrm{md}}(\gamma)$ defined by (1.46), which was evaluated by using (1.1) and averaging the exact expression of $\mathrm{PEP}_{\mathrm{md}}(\mathbf{h}, \mathbf{m})$ reported in (1.41). All the curves show a good agreement between exact and approximate results for both the considered STBC rules, thus demonstrating that $\widehat{G}_d^{\mathrm{md}}(\gamma)$ is good candidate to substitute $G_d^{\mathrm{md}}(\gamma)$ when theoretical findings are of concern.

Example 4: ABER analysis with Alamouti STBC ($L = 2$)

In this example, it was used a QPSK signaling and the full-rate Alamouti code of order $L = K = P = 2$ [64], as in Example 1. Figs. 1.3 and 1.4 refer to the case of near-Gaussian and very highly-impulsive noise, respectively. In this case, the asymptotic diversity order of all the schemes under comparison is equal to $R_{\max} = \min\{L, N_{\max} + 1\} = 2$ for both the values of $N_{\max}$. In the left-side plot, the number of active relays in Phase II is kept fixed, whereas in the right-side plot, the number of active relays in Phase II is randomly time-varying according to the statistical distribution of the vector $\tilde{\mathbf{s}}$ discussed in Section 1.2.

It is apparent from all the figures that the ABER curves of the IML detector strictly follow the corresponding ones of the ML detector. In particular, independently of the detecting structure employed at the destination, the complex Gaussian decentralized scheme pays a performance degradation with respect to its centralized counterpart in both the noise environments, that becomes slight by increasing the number of relays. Moreover, with reference to the very highly-impulse noise case, the fluctuating trend of the finite-SNR diversity order of the MD detector significantly penalizes the ABER performance of such a detector in both its centralized and decentralized versions. Finally, the randomness in the number of active relays impacts on both the coding gain and the diversity order of the detectors in both noise environments; in particular, it is worth noticing that, for moderate-to-high SNR values, such an impact on the diversity order is not significant, i.e., each ABER curve in the left-side plots of Figs. 1.3 and 1.4 exhibits a similar slope to the corresponding curve in the right-side plots.

Example 5: ABER and finite-SNR diversity order analysis with orthogonal STBC of order $L = 3$

In this example, it was used a BPSK signaling, i.e., $\tilde{a}_k = \{\pm 1\}$, for $k \in \{1, 2, \ldots, K\}$, to reduce the implementation complexity of the ML detector. We considered as STBC rule the complex orthogonal code of order $L = K = 3$ code rate is $K/P = 3/4$ [65]. The ABER curves of Fig. 1.5 and the finite-SNR diversity order results in Fig. 1.6, the latter ones were obtained by using (1.1) and averaging (1.10) and (1.41), refer to the case of $N_{\max} = 2$ active relays for highly-impulsive noise. In this case, the asymptotic diversity order of all the schemes under comparison is equal to $R_{\max} = \min\{L, N_{\max} + 1\} = 3$. In the left-side plot, the number of active relays in Phase II is kept fixed to 2, whereas in the right-side plot, the number of active relays in Phase II is randomly time-varying according to the statistical distribution of $\tilde{\mathbf{s}}$ discussed in Section 1.2. Besides confirming the results of Example 4, it is also apparent from Fig. 1.5 that, in the case of highly-impulsive noise, the larger is the diversity order, the more evident is the performance penalty of the MD detector with respect to the ML and IML ones in terms of coding gain. This is in accordance with the theoretical results derived in Subsections 1.3.2 and 1.4.2. Finally, it can be argued from Fig. 1.6 that, for $\gamma > 16$ dB, the diversity order of the MD detector when the number of relays is randomly time-varying approximatively

exhibits the same behavior of the case in which the number of relays is fixed, whereas the randomness in the number of active relays tends to smooth the difference between the diversity order of the centralized and decentralized IML detectors.

1.6 Conclusions

In this first chapter, we studied the performance of distributed Space-Time Block Coding (STBC) schemes involving multiple decode-and-forward (D&F) relays in the presence of Middleton Class-A (MCA) impulsive noise, by considering both optimal and suboptimal detecting structures at the destination. Our analytical analysis and simulation results show that the principal adverse impact of highly-impulsive noise on the system performance is to significantly slow down the rate of convergence of the diversity order to its asymptotic value $R_{\max} = \min(L, N_{\max}+1)$. This effect is much more evident for the MD detector, which additionally pays a significant performance penalty with respect to the ML and IML detectors in terms of coding gain. Future research issues consist of applying our general framework to different relaying strategies and suboptimal detectors with memoryless nonlinearity.

Chapter 2

Decision Maker Approaches for Cooperative Spectrum Sensing: Participate or Not Participate in Sensing?

2.1 Introduction

Cognitive Radio (CR) [66], [67], [68], is considered the enabling technology of the Dynamic Spectrum Access (DSA) paradigm which is envisaged to solve the current radio spectrum inefficiency problem and satisfy the increased demand for bandwidth. This objective is achieved by allowing the unlicensed users, referred to as Cognitive Users (CUs), to dynamically exploit the spectrum opportunities, also referred to as Spectrum Holes, namely the portions of the radio spectrum temporarily not occupied by the licensed users, referred to as Primary Users (PUs), which have the priority for using the spectrum.

Spectrum Sensing [69], [70], is the key functionality of CR networks since it enables the CU to discover the spectrum opportunities in the surrounding radio environment, namely to discriminate between the presence or the absence of the PU. One of the main objectives of spectrum sensing techniques is to guarantee an high detection accuracy for avoiding PU interference. However, this objective is difficult to achieve due to the wireless-channel impairments, such as multipath fading and shadowing, that severely affect the sensing reliability. Thus, recently, *cooper-*

ative spectrum sensing has been proposed as an effective way to improve the sensing performance by exploiting the spatial diversity among the CUs. By cooperation, CUs share their local sensing information through links, referred to as reporting channels (RCs), and a decision maker combines these sensing statistics to take the cooperative decision about the presence of the PU [17, 19, 71–74].

The cooperative sensing techniques available in literature are mainly based on two different *decision approaches*, according to the role of the decision maker. In the first approach, referred to as *Combining Decision* (CD), the role of the decision maker is only to combine the sensing information collected from its cooperators, without participating in the sensing of the monitored band. Differently, in the second approach, referred to as *Sensing & Combining Decision* (SCD), the decision maker combines not only the sensing information of its cooperators, but also its own local sensing information.

Traditionally, the choice between the CD and SCD approaches is based on the adopted cooperative sensing architecture [19]. More in detail, CD is adopted in centralized cooperative sensing architectures[1], whereas SCD is adopted in distributed cooperative sensing architectures[2]. This choice is mainly historical, due to the application of the classical centralized versus distributed paradigm in CR scenarios. Nevertheless, in the appealing context of the CR Ad-Hoc Networks (CRAHNs) [18], the aforementioned choice to associate the CD and the SCD approaches to centralized and distributed cooperative sensing architectures, respectively, is not mandatory. Hence, any arbitrary cooperative sensing technique can be implemented according to either the CD or the SCD approach, regardless of the underlying cooperative sensing architecture.

As we prove through the work [75], the adoption of the CD or the SCD approach deeply affects the performance of the considered cooperative sensing technique, in terms of detection accuracy and, consequently, in terms of PU interference avoidance [19]. However, the key issue of

[1] Centralized cooperative sensing architecture denotes a cooperative sensing based on a central entity, referred to as Fusion Center (FC), that handles the entire cooperative process. In infrastructure-based networks, the CR base-station is naturally the FC, whereas in CRAHNs any CU can act as FC [19].

[2] Distributed cooperative sensing architecture denotes a cooperative sensing that does not rely on a central entity that handles the cooperative process, but the task is distributed among the CUs acting as decision makers.

choosing the decision approach that guarantees the higher detection accuracy independently of the underlying cooperative sensing architecture is still an open problem.

For this reason, in this work, we derive the criteria for an effective *decision-approach selection*. To the best of our knowledge, this is the first work that addresses this issue.

Specifically, we prove that the detection accuracy of a cooperative spectrum sensing technique exhibits a threshold behavior as a function of the adopted decision approach: *it exists a threshold value that determines two different operating regions, depending on the sensing and reporting channel parameters*. In one region, the higher detection accuracy is assured by implementing the cooperative sensing technique according to the CD approach, whereas in the other region, the higher detection accuracy is guaranteed by the SCD approach, regardless of the underlying cooperative sensing architecture and the adopted sensing technique[3].

The rest of the chapter is organized as follows. In Sec. 2.2, we present the problem statement, along with the contributions of the paper. In Sec. 2.3, we describe the system model. In Sec. 2.4 we present intermediate results that will be used in Sec. 2.5 to prove the existence of the threshold behavior in the detection accuracy. We validate the analytical results by simulation in Sec. 2.6. In Sec. 2.7, we conclude the paper, and, finally, some proofs are demonstrated in the appendices.

2.2 Problem Statement and Contributions

In the following, we first present some definitions used through the paper, then we formulate the problem statement along with the contributions of the work.

2.2.1 Problem Statement

Let us consider a typical cooperative sensing scenario in which M CUs cooperate to take the decision about the PU presence on the monitored band. In the rest of the paper, we consider an equal number M

[3]In Sec. **??**, we prove that the adopted cooperative sensing technique influences only the value of the threshold, not its existence.

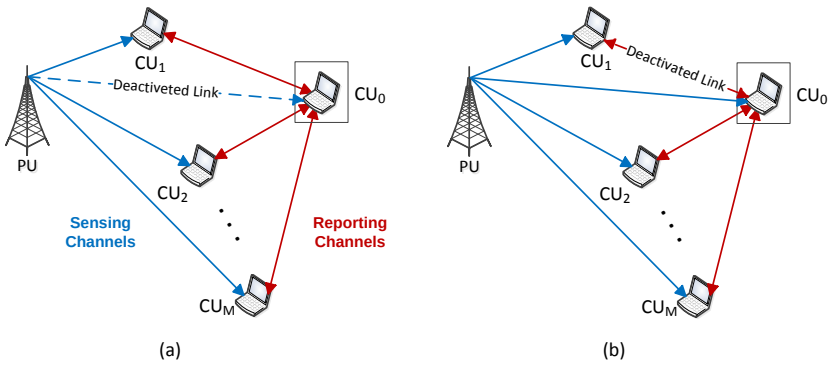

Figure 2.1: (*a*) Combining Decision (CD) Approach; (*b*) Sensing & Combining Decision (SCD) Approach.

of cooperative CUs in both the CD and the SCD approaches for a fair comparison.

Definition 1. *Combining Decision (CD) Approach.* The decision maker combines, according to a certain criterion, only the local sensing data of its cooperators, without participating in the sensing of the monitored band, as depicted in Fig. 2.1-(a).

Remark 1. Definition 1 implies that all the M sensing statistics are sent from the CU neighbors to the decision maker through the reporting channels, since the decision maker does not participate in the sensing of the monitored band. Thus, in Fig. 2.1-(a), the sensing link between the decision maker and the arbitrary PU is denoted as *deactivated*.

Definition 2. *Sensing & Combining Decision (SCD) Approach.* The decision maker combines, according to a certain criterion, both the sensing data received from its cooperators and its own local sensing data, as depicted in Fig. 2.1-(b).

Remark 2. Definition 2 implies that $(M-1)$ sensing statistics (rather than M) are sent from the CU neighbors to the decision maker through the reporting channels, since a sensing statistic is locally available at the decision maker. Thus, in Fig. 2.1-(b), the reporting channel between the decision maker and the arbitrary CU_1 is denoted as *deactivated*.

In Remarks 3 and 4 we discuss the applicability of the CD and SCD approaches in both centralized and distributed cooperative sensing architectures.

Remark 3. CD is the traditional approach adopted in centralized cooperative sensing architectures. In fact, in such a case, the decision maker (CU_0 in Fig. 2.1-a), acts only as FC and the other CUs perform local sensing and report the results back to CU_0 [19]. Differently, adopting the SCD approach in centralized cooperative sensing architectures constitutes a new hybrid solution, in which the decision maker CU_0 not only acts as FC, but it also participates in the sensing of the band.

Remark 4. SCD is the traditional approach adopted in distributed cooperative sensing architectures. In fact, in such a case, each CU exchanges its sensing information with its neighbors and then it combines its local data with the received sensing data for deciding on the PU presence[4] [19]. Differently, adopting the CD approach in distributed cooperative sensing architectures constitutes a new hybrid solution, in which an arbitrary CU combines the received sensing data, without participating in the sensing of the monitored channel band.

Problem Definition:. To analytically single out the criteria establishing how to choose the decision approach that guarantees the higher detection accuracy independently of the underlying cooperative sensing architecture. From Definitions 1 and 2, this problem can be reformulated as to analytically single out the criteria establishing when it is more advantageous in terms of detection accuracy to use the local sensing statistic of the decision maker, by allowing it to participate in the sensing process, than to involve another CU in the cooperative process.

[4]Traditionally, in distributed cooperative sensing architectures, the CUs repeat the described process to converge to a unified decision [19]. In this work, we focus on enhancing the reliability of the decision made by each CU by selecting the effective decision approach, since, clearly, this enhances in turn the reliability of the possible unified decision. Moreover, we observe that reaching a unified decision could be not practicable for two main reasons: *i*) in dynamic PU environments, the long decision delays induced by the iterative nature of the unified-decision techniques could not be tolerable; *ii*) if the RCs are not ideal, the underlying assumption of the unified-decision techniques, i.e., to have a reliable decision exchange among the CUs, is violated. Hence, in these scenarios, enhancing the reliability of the decision made by each CU is even more important.

2.2.2 Contributions

In this work, we solve the aforementioned decision approach problem through a theoretical analysis, by adopting the realistic multipath frequency-selective channel model for the RCs. To guarantee generality to the proposed analysis, we consider three different cooperative sensing techniques, implemented according to both the decision approaches: the optimal Likelihood Ratio-Test (LRT) based on the Neyman-Pearson criterion [76] used as benchmark, and two techniques, based on a Linear (L) and Widely-Linear (WL) processing.

We observe that the CD design of a L and a WL cooperative technique able to work in presence of temporal dispersive RCs has been recently proposed in literature [72, 77], as we discuss in Sec. 2.4. Differently, to the best of our knowledge, no technique designed according to the SCD approach able to work in presence of temporal dispersive RCs is available in literature. Motivated by this, to carry out the theoretical comparison between the two decision approaches, in this paper we also design both a L and WL cooperative techniques according to the SCD approach for dispersive RCs (see Sec. 2.4).

In a nutshell, the contribution of the work is threefold: *i*) we design two cooperative techniques for the SCD approach, able to counteract the RC temporal dispersion; *ii*) we analytically derive the criteria for choosing the decision approach assuring the higher detection accuracy, independently of the underlying cooperative sensing architecture; *iii*) we analytically prove that the detection accuracy exhibits a threshold behavior as a function of the adopted decision approach, and we provide the closed-form expression of the threshold value.

2.3 System Model

Here we first describe the system model at each CU, then the system model for both the CD and the SCD approaches, by accounting for temporal dispersive RCs.

Notations: $\mathcal{H}_0$ and $\mathcal{H}_1$ denote the hypotheses of absence and presence of the PU, respectively; the fields of complex and real numbers are denoted with $\mathbb{C}$ and $\mathbb{R}$; matrices [vectors] are denoted with upper case [lower case] boldface letters (e.g., $\mathbf{X}$ or $\mathbf{x}$); the field of $m \times n$ complex [real] matrices is denoted as $\mathbb{C}^{m\times n}$ [$\mathbb{R}^{m\times n}$], with $\mathbb{C}^m$ [$\mathbb{R}^m$] used as a shorthand for $\mathbb{C}^{m\times 1}$ [$\mathbb{R}^{m\times 1}$]; the superscripts $*$, T, H, -1 and $\dagger$ de-

note the conjugate, the transpose, the Hermitian (conjugate transpose), the inverse of a matrix and the Moore-Penrose inverse (generalized inverse) [78], respectively; the subscripts c and sc denote the CD and the SCD approaches, respectively; $\mathbf{I}_m \in \mathbb{R}^{m\times m}$, $\mathbf{0}_{m\times n} \in \mathbb{R}^{m\times n}$ and $\mathbf{1}_m \in \mathbb{R}^m \triangleq [1,\ldots,1]^T$ denote the identity matrix, the null matrix and the unitary vector, respectively; trace($\mathbf{X}$) and rank($\mathbf{X}$) represent the trace and the rank of the matrix $\mathbf{X}$; $\mathcal{R}(\mathbf{X})$ and $\mathcal{N}(\mathbf{X})$ denote the range and the null space of $\mathbf{X}$; for any $\mathbf{a} \in \mathbb{C}^m$, $||\mathbf{a}||_2^2 \triangleq \sqrt{\mathbf{a}^H\mathbf{a}}$ denotes the Euclidean norm; $\mathbf{A} = \text{diag}(\mathbf{A}_{11}\mathbf{A}_{22}\ldots\mathbf{A}_{nn})$ is a diagonal matrix with elements $\mathbf{A}_{ii}$ on the main diagonal; E[$\cdot$] and Var[$\cdot$] denote the statistical mean and variance, respectively; Re[$\cdot$] denotes the real part.

2.3.1 The Local Sensing Model

We consider a CR network with M cooperative CUs. The base-band received signal $x_i(k)$ at the i-th CU is [19, 72]:

$$x_i(k) = \begin{cases} v_i(k) & \mathcal{H}_0 \\ g_i\, s(k) + v_i(k) & \mathcal{H}_1 \end{cases} \tag{2.1}$$

where $s(k)$ is the PU's transmitted signal, g_i is the complex channel coefficient that models the sensing channel (SC) between the PU and the i-th CU, $v_i(k) \sim \mathcal{CN}(0,\sigma_i^2)$ is the complex zero-mean Additive White Gaussian Noise (AWGN), assumed circular (or proper) [79], i.e., $E[v_i(n)\, v_i(m)] = 0, \forall n,m \in Z$. Each CU adopts an energy detector as local sensing technique, i.e., $u_i(q) = \frac{1}{N}\sum_{k=qN_s}^{qN_s+N-1} |x_i(k)|^2$ [80], where $N = \lfloor \tau\, f_s \rfloor$ is the number of samples available in the sensing time τ, f_s is the sampling frequency and $N_s > N$ denotes the period of the sensing process. According to the Central Limit Theorem, for large N, $u_i(q)$ is approximated by a Gaussian random variable (r.v.) under both the hypotheses $\mathcal{H}_0$ and $\mathcal{H}_1$ [72, 80, 81], with mean $E[u_i(q)|\mathcal{H}_j] \triangleq \nu_{i|\mathcal{H}_j}$ and variance $\text{Var}[u_i(q)|\mathcal{H}_j] \triangleq \zeta_{i|\mathcal{H}_j}$ given by, respectively [72]:

$$\nu_{i|\mathcal{H}_j} = \begin{cases} \sigma_i^2 & \mathcal{H}_0 \\ |g_i|^2\breve{\mathcal{E}}_s + \sigma_i^2 & \mathcal{H}_1 \end{cases}, \; \zeta_{i|\mathcal{H}_j} = \begin{cases} \frac{\sigma_i^4}{N} & \mathcal{H}_0 \\ \frac{2\,|g_i|^2\breve{\mathcal{E}}_s\sigma_i^2+\sigma_i^4}{N} & \mathcal{H}_1 \end{cases} \tag{2.2}$$

where, $\breve{\mathcal{E}}_s = E_s/N = \sum_{k=0}^{N-1} |s(k)|^2/N$ is the PU transmitted energy normalized with respect to the sensing samples[5] N.

[5] $s(k)$ is assumed deterministic and unknown as in [72, 77, 81]. However, if $s(k)$ is modeled as a sequence of i.i.d. r.vv., $u_i(q)$ is still approximated by a Gaussian

2.3.2 The SCD Approach Model

Let us consider an arbitrary CU, say CU_0, acting as decision maker according to the SCD approach and combining M sensing statistics. From Definition 2, it follows that $(M-1)$ sensing statistics are received from $(M-1)$ cooperative CUs, whereas one sensing statistic is locally available. Without loss of generality, let us denote the $(M-1)$ cooperative CUs as $\mathrm{CU}_2, \ldots, \mathrm{CU}_M$. The base-band signal at CU_0 RF front-end, received from the i-th CU, can be written as:

$$y_i(l) = \begin{cases} u_0(l), & \text{if } i = 0 \\ \sum_{n=0}^{L_{g_i}-1} u_i(l-n)h_i(n) + n_i(l), & \text{if } i \in \{2, \ldots, M\} \end{cases} \tag{2.3}$$

where l-th is the arbitrary sampling instant at the CU_0 side, $n_i(l) \sim \mathcal{CN}(0, \delta_i^2)$ is the complex, circular, zero-mean, spatially un-correlated, AWGN at the CU_0 side, $\{h_i(n)\}_{n=0}^{L_{g_i}-1}$ is the finite multipath channel impulse response with length L_{g_i} that models the RC between the i-th CU and CU_0, and $u_0(l)$ is the CU_0 local sensing statistic. It is reasonable to assume that geographically distributed CUs experience independent fading. Therefore, $u_i(l_1)$ and $u_j(l_2)$, $i \neq j$, are spatially uncorrelated under each hypothesis [72] and independent of the noise too. To simplify the notation, L_g denotes the largest channel length, i.e., $L_g = \max_{i=2}^{M} L_{g_i}$. At CU_0, due to the dispersive RCs, we jointly elaborate L_e received samples for each CU, i.e., $\mathbf{y}_i(l) \triangleq [y_i(l)\, y_i(l-1) \ldots y_i(l-L_e+1)]^T \in \mathbb{C}^{L_e}$, which, by using (2.3), is equal to:

$$\mathbf{y}_i(l) = \begin{cases} \mathbf{H}_0\, \mathbf{u}_0(l), & \text{if } i = 0 \\ \mathbf{H}_i\, \mathbf{u}_i(l) + \mathbf{n}_i(l), & \text{if } i \in \{2, \ldots, M\} \end{cases} \tag{2.4}$$

In (2.4), for $i \neq 0$, $\mathbf{H}_i \in \mathcal{C}^{L_e \times (L_e+L_g-1)}$ is a Toeplitz upper triangular matrix with first row $[h_i(0) \ldots h_i(L_g-1)\, 0 \ldots 0]$ and first column $[h_i(0)\, 0 \ldots 0]^T$, $\mathbf{H}_0 \in \mathcal{R}^{L_e \times (L_e+L_g-1)}$ is the Toeplitz matrix with first row and first column equal to $[1\, 0 \ldots 0]^T$, $\mathbf{u}_i(l) \triangleq [u_i(l) \ldots u_i(l-L_e-L_g+2)]^T \in \mathbb{R}^{L_e+L_g-1}$ and $\mathbf{n}_i(l) \triangleq [n_i(l) \ldots n_i(l-L_e+1)]^T \in \mathbb{C}^{L_e}$. By defining $\mathbf{H}_{\mathrm{sc}} \triangleq \mathrm{diag}[\mathbf{H}_0\, \overline{\mathbf{H}}]$, with $\overline{\mathbf{H}} \triangleq \mathrm{diag}[\mathbf{H}_2 \ldots \mathbf{H}_M] \in \mathbb{C}^{(M-1)L_e \times (M-1)(L_e+L_g-1)}$, $\mathbf{u}_{\mathrm{sc}}(l) \triangleq [\mathbf{u}_0^T(l)\, \overline{\mathbf{u}}^T(l)]^T$, with $\overline{\mathbf{u}}(l) \triangleq [\mathbf{u}_2^T(l) \ldots \mathbf{u}_M^T(l)]^T \in \mathbb{R}^{(M-1)(L_e+L_g-1)}$, $\mathbf{n}_{\mathrm{sc}}(l) \triangleq [\mathbf{0}_{L_e}^T\, \overline{\mathbf{n}}^T(l)]^T$, with

r.v. [80], and the subsequent analysis continues to hold.

$\overline{\mathbf{n}}(l) \triangleq [\mathbf{n}_2^T(l) \dots \mathbf{n}_M^T(l)]^T \in \mathbb{C}^{(M-1)L_e}$, and $\overline{\mathbf{y}}(l) \triangleq [\mathbf{y}_2^T(l) \dots \mathbf{y}_M^T(l)]^T$, (2.4) is rewritten as[6]:

$$\mathbf{y}_{\text{sc}}(l) \in \mathbb{C}^{ML_e} \triangleq [\mathbf{y}_0^T(l) \ \overline{\mathbf{y}}^T(l)]^T = \mathbf{H}_{\text{sc}}\mathbf{u}_{\text{sc}}(l) + \mathbf{n}_{\text{sc}}(l) \tag{2.5}$$

By using (2.2) and (2.5), the mean $\boldsymbol{\mu}_{\text{sc}|\mathcal{H}_j} \triangleq E[\mathbf{y}_{\text{sc}}(l)|\mathcal{H}_j] \in \mathbb{C}^{ML_e}$ and the covariance matrix $\mathbf{C}_{\mathbf{y}_{\text{sc}}|\mathcal{H}_j} \triangleq E[(\mathbf{y}_{\text{sc}}(l) - \boldsymbol{\mu}_{\text{sc}})(\mathbf{y}_{\text{sc}}(l) - \boldsymbol{\mu}_{\text{sc}})^H|\mathcal{H}_j] \in \mathbb{C}^{ML_e \times ML_e}$ of the Gaussian random vector $\mathbf{y}_{\text{sc}}(l)$ are equal to, respectively:

$$\boldsymbol{\mu}_{\text{sc}|\mathcal{H}_j} = \mathbf{H}_{\text{sc}}\, E[\mathbf{u}_{\text{sc}}(l)|\mathcal{H}_j] = \mathbf{H}_{\text{sc}}\, \boldsymbol{\eta}_{\text{sc},\mathcal{H}_j} \tag{2.6}$$

$$\mathbf{C}_{\mathbf{y}_{\text{sc}}|\mathcal{H}_j} = \mathbf{H}_{\text{sc}}\, \mathbf{C}_{\mathbf{u}_{\text{sc}}|\mathcal{H}_j}\, \mathbf{H}_{\text{sc}}^H + \mathbf{R}_{\mathbf{n}_{\text{sc}}} \tag{2.7}$$

In (2.6), $\boldsymbol{\eta}_{\text{sc}|\mathcal{H}_j} \triangleq E[\mathbf{u}(l)|\mathcal{H}_j] = [\boldsymbol{\eta}_{0|\mathcal{H}_j}^T\, \overline{\boldsymbol{\eta}}_{\mathcal{H}_j}^T]^T$, with $\overline{\boldsymbol{\eta}}_{\mathcal{H}_j}$ defined as $\overline{\boldsymbol{\eta}}_{\mathcal{H}_j} \triangleq [\boldsymbol{\eta}_{2|\mathcal{H}_j}^T \dots \boldsymbol{\eta}_{M|\mathcal{H}_j}^T]^T$ and $\boldsymbol{\eta}_{k|\mathcal{H}_j} = \nu_{k|\mathcal{H}_j}\, \mathbf{1}_{\{L_e+L_g-1\}}$.
In (2.7), $\mathbf{R}_{\mathbf{n}_{\text{sc}}} \triangleq E[\mathbf{n}_{\text{sc}}(l)\, \mathbf{n}_{\text{sc}}^H(l)] \in \mathbb{R}^{ML_e \times ML_e}$ is the noise covariance matrix equals to:

$$\mathbf{R}_{\mathbf{n}_{\text{sc}}} = \text{diag}[\mathbf{0}_{L_e \times L_e} \mathbf{R}_{\mathbf{n}_2} \dots \mathbf{R}_{\mathbf{n}_M}] \triangleq \text{diag}[\mathbf{0}_{L_e \times L_e}\, \mathbf{R}_{\overline{\mathbf{n}}}] \tag{2.8}$$

with $\mathbf{R}_{\mathbf{n}_i} \triangleq E[\mathbf{n}_i(l)\, \mathbf{n}_i^H(l)] = \delta_i^2 \mathbf{I}_{\{L_e \times L_e\}}$ and $\mathbf{R}_{\overline{\mathbf{n}}} \in \mathbb{R}^{(M-1)L_e \times (M-1)L_e} \triangleq \text{diag}[\mathbf{R}_{\mathbf{n}_2} \dots \mathbf{R}_{\mathbf{n}_M}]$, whereas $\mathbf{C}_{\mathbf{u}_{\text{sc}}|\mathcal{H}_j} \triangleq E[(\mathbf{u}_{\text{sc}}(l) - \boldsymbol{\eta}_{\text{sc}})(\mathbf{u}_{\text{sc}}(l) - \boldsymbol{\eta}_{\text{sc}})^H|\mathcal{H}_j] \in \mathbb{R}^{M(L_e+L_g-1) \times M(L_e+L_g-1)}$ is the sensing covariance matrix equals to:

$$\begin{aligned} \mathbf{C}_{\mathbf{u}_{\text{sc}}|\mathcal{H}_j} &= \text{diag}[\mathbf{C}_{\mathbf{u}_0|\mathcal{H}_j} \mathbf{C}_{\mathbf{u}_2|\mathcal{H}_j} \dots \mathbf{C}_{\mathbf{u}_M|\mathcal{H}_j}] \\ &\triangleq \text{diag}[\mathbf{C}_{\mathbf{u}_0|\mathcal{H}_j}\, \mathbf{C}_{\overline{\mathbf{u}}|\mathcal{H}_j}] \end{aligned} \tag{2.9}$$

with $\mathbf{C}_{\mathbf{u}_i|\mathcal{H}_j} \triangleq E[(\mathbf{u}_i(l) - \boldsymbol{\eta}_i)(\mathbf{u}_i(l) - \boldsymbol{\eta}_i)^H|\mathcal{H}_j] = \zeta_{i|\mathcal{H}_j}\, \mathbf{I}_{\{L_e+L_g-1\}}$ and $\mathbf{C}_{\overline{\mathbf{u}}|\mathcal{H}_j} \triangleq \text{diag}[\mathbf{C}_{\mathbf{u}_2|\mathcal{H}_j} \dots \mathbf{C}_{\mathbf{u}_M|\mathcal{H}_j}]$. By exploiting (2.5), $\mathbf{C}_{\mathbf{y}_{\text{sc}}|\mathcal{H}_j}$ in (2.7) is equivalently expressed as:

$$\mathbf{C}_{\mathbf{y}_{\text{sc}}|\mathcal{H}_j} = \begin{bmatrix} \mathbf{C}_{\mathbf{y}_0|\mathcal{H}_j} & \mathbf{0}_{L_e \times (M-1)L_e} \\ \mathbf{0}_{(M-1)L_e \times L_e} & \mathbf{C}_{\overline{\mathbf{y}}|\mathcal{H}_j} \end{bmatrix} \tag{2.10}$$

where

$$\mathbf{C}_{\mathbf{y}_0|\mathcal{H}_j} \in \mathbb{R}^{L_e \times L_e} \triangleq \mathbf{H}_0\, \mathbf{C}_{\mathbf{u}_0|\mathcal{H}_j}\, \mathbf{H}_0^H = \zeta_{0|\mathcal{H}_j}\, \mathbf{I}_{\{L_e\}} \tag{2.11}$$

[6]The transmissions of different CUs are assumed orthogonal, [72, 77, 81].

$$\mathbf{C}_{\overline{\mathbf{y}}|\mathcal{H}_j} \in \mathbb{C}^{(M-1)L_e \times (M-1)L_e} \triangleq \overline{\mathbf{H}}\,\mathbf{C}_{\overline{\mathbf{u}}|\mathcal{H}_j}\,\overline{\mathbf{H}}^H + \mathbf{R}_{\overline{\mathbf{n}}} \tag{2.12}$$

Finally, since the pseudo-covariance matrix which is defined as $\mathbf{C}_{\mathbf{y}^*_{\rm sc}|\mathcal{H}_j} \triangleq E[(\mathbf{y}_{\rm sc}(l)-\boldsymbol{\mu})\,(\mathbf{y}_{\rm sc}(l)-\boldsymbol{\mu})^T|\mathcal{H}_j] \in \mathbb{C}^{ML_e \times ML_e}$ of $\mathbf{y}_{\rm sc}(l)$ is not null, $\mathbf{y}_{\rm sc}(l)$ is improper [79], and $\mathbf{C}_{\mathbf{y}^*_{\rm sc}|\mathcal{H}_j}$ is given by:

$$\mathbf{C}_{\mathbf{y}^*_{\rm sc}|\mathcal{H}_j} = \mathbf{H}_{\rm sc}\mathbf{C}_{\mathbf{u}_{\rm sc}|\mathcal{H}_j}\mathbf{H}^T_{\rm sc} = \begin{bmatrix} \mathbf{C}_{\mathbf{y}_0|\mathcal{H}_j} & \mathbf{0}_{L_e\times(M-1)L_e} \\ \mathbf{0}_{(M-1)L_e\times L_e} & \mathbf{C}_{\overline{\mathbf{y}}^*|\mathcal{H}_j} \end{bmatrix} \tag{2.13}$$

where, we exploited the circular property of $\mathbf{n}_{\rm sc}(l)$, i.e., $\mathbf{R}_{\mathbf{n}^*_{\rm sc}} = 0$, $\mathbf{C}_{\mathbf{y}_0|\mathcal{H}_j}$ is given in (2.11) and, finally,

$$\mathbf{C}_{\overline{\mathbf{y}}^*|\mathcal{H}_j} \in \mathbb{C}^{(M-1)L_e \times (M-1)L_e} = \overline{\mathbf{H}}\,\mathbf{C}_{\overline{\mathbf{u}}|\mathcal{H}_j}\,\overline{\mathbf{H}}^T \tag{2.14}$$

2.3.3 The CD Approach Model

Let us consider now CU_0 acting as decision maker according to the CD approach and combining M sensing statistics. From Definition 1, all the M sensing statistics are received from the M cooperative CUs, denoted without loss of generality as $\mathrm{CU}_1,\ldots,\mathrm{CU}_M$. Hence, the base-band signal at CU_0 RF front-end received from the i-th CU can be written as:

$$y_i(l) = \sum_{n=0}^{L_{g_i}-1} u_i(l-n)h_i(n) + n_i(l),\ i \in \{1,2,\ldots,M\} \tag{2.15}$$

Remark 5. (2.15) differs from (2.4) for the presence of the CU_1 sensing statistic and the absence of the decision maker sensing statistic $u_0(l)$. In fact, according to Definition 1, the decision maker CU_0 does not participate in the sensing of the monitored band and another CU, labeled without loss of generality as CU_1, is involved in the cooperative sensing process. We underline that the number of cooperators is fixed to M in both the approaches for a fair comparison. Clearly, the definitions of $\overline{\mathbf{H}}$, $\overline{\mathbf{u}}(l)$ and $\overline{\mathbf{y}}(l)$, given above, are kept unchanged since they involve the cooperative CUs common to both the approaches, i.e., $\mathrm{CU}_2,\ldots,\mathrm{CU}_M$.

Similarly to Sec. 2.3.1, by denoting with $\mathbf{H}_1 \in \mathcal{C}^{L_e\times(L_e+L_g-1)}$ the Toeplitz upper triangular matrix with first row $[h_1(0)\ldots h_1(L_g{-}1)0\ldots0]$ and first column $[h_1(0)0\ldots0]^T$, $\mathbf{H}_{\rm c} \triangleq \mathrm{diag}[\mathbf{H}_1\,\overline{\mathbf{H}}]$, $\mathbf{u}_c(l) \triangleq [\mathbf{u}_1^T(l)\,\overline{\mathbf{u}}^T(l)]^T$, $\mathbf{n}_c(l) \triangleq [\mathbf{n}_1^T(l)\,\overline{\mathbf{n}}^T(l)]^T$, (2.15) is reformulated as follows:

$$\mathbf{y}_c(l) \in \mathbb{C}^{ML_e} = [\mathbf{y}_1^T(l)\ \ \overline{\mathbf{y}}^T(l)]^T = \mathbf{H}_c\mathbf{u}_c(l) + \mathbf{n}_c(l) \tag{2.16}$$

The mean $\boldsymbol{\mu}_{\mathrm{c}|\mathcal{H}_j} \in \mathbb{C}^{ML_e}$ and covariance matrix $\mathbf{C}_{\mathbf{y}_c|\mathcal{H}_j} \triangleq E[(\mathbf{y}_c(l) - \boldsymbol{\mu}_c)(\mathbf{y}_c(l) - \boldsymbol{\mu}_c)^H|\mathcal{H}_j] \in \mathbb{C}^{ML_e \times ML_e}$ of the Gaussian vector $\mathbf{y}_c(l)$ are equal to:

$$\boldsymbol{\mu}_{\mathrm{c}|\mathcal{H}_j} \triangleq E[\mathbf{y}_c(l)|\mathcal{H}_j] = \mathbf{H}_c\, E[\mathbf{u}_c(l)|\mathcal{H}_j] = \mathbf{H}_c\, \boldsymbol{\eta}_{\mathrm{c},\mathcal{H}_j} \tag{2.17}$$

$$\mathbf{C}_{\mathbf{y}_c|\mathcal{H}_j} = \mathbf{H}_c \mathbf{C}_{\mathbf{u}_c|\mathcal{H}_j} \mathbf{H}_c^H + \mathbf{R}_{\mathbf{n}_c} = \begin{bmatrix} \mathbf{C}_{\mathbf{y}_1|\mathcal{H}_j} & \mathbf{0}_{L_e \times (M-1)L_e} \\ \mathbf{0}_{(M-1)L_e \times L_e} & \mathbf{C}_{\overline{\mathbf{y}}|\mathcal{H}_j} \end{bmatrix} \tag{2.18}$$

In (2.17), $\boldsymbol{\eta}_{\mathrm{c}|\mathcal{H}_j} \triangleq E[\mathbf{u}_c(l)|\mathcal{H}_j] = [\boldsymbol{\eta}_{1|\mathcal{H}_j}^T\, \overline{\boldsymbol{\eta}}_{\mathcal{H}_j}^T]^T$. In (2.18), $\mathbf{C}_{\overline{\mathbf{y}}|\mathcal{H}_j}$ is given by (2.12), $\mathbf{R}_{\mathbf{n}_c} \in \mathbb{R}^{ML_e \times ML_e} \triangleq E[\mathbf{n}_c(l)\, \mathbf{n}_c^H(l)] = \mathrm{diag}[\mathbf{R}_{\mathbf{n}_1}\, \mathbf{R}_{\overline{\mathbf{n}}}]$ and

$$\mathbf{C}_{\mathbf{y}_1|\mathcal{H}_j} \in \mathbb{C}^{L_e \times L_e} = \mathbf{H}_1\, \mathbf{C}_{\mathbf{u}_1|\mathcal{H}_j}\, \mathbf{H}_1^H + \mathbf{R}_{\mathbf{n}_1} \tag{2.19}$$

Finally, the no-null pseudo-covariance matrix which is defined as $\mathbf{C}_{\mathbf{y}_c^*|\mathcal{H}_j} \triangleq E[(\mathbf{y}_c(l) - \boldsymbol{\mu}_c)(\mathbf{y}_c(l) - \boldsymbol{\mu}_c)^T|\mathcal{H}_j] \in \mathbb{C}^{ML_e \times ML_e}$ of $\mathbf{y}_c(l)$ is:

$$\mathbf{C}_{\mathbf{y}_c^*|\mathcal{H}_j} = \mathbf{H}_c \mathbf{C}_{\mathbf{u}_c|\mathcal{H}_j} \mathbf{H}_c^T = \begin{bmatrix} \mathbf{C}_{\mathbf{y}_1^*|\mathcal{H}_j} & \mathbf{0}_{L_e \times (M-1)L_e} \\ \mathbf{0}_{(M-1)L_e \times L_e} & \mathbf{C}_{\overline{\mathbf{y}}^*|\mathcal{H}_j} \end{bmatrix} \tag{2.20}$$

with $\mathbf{C}_{\overline{\mathbf{y}}^*|\mathcal{H}_j}$ reported in (2.14) and $\mathbf{C}_{\mathbf{y}_1^*|\mathcal{H}_j} = \mathbf{H}_1\, \mathbf{C}_{\mathbf{u}_1|\mathcal{H}_j}\, \mathbf{H}_1^T$.

2.4 Cooperative Spectrum Sensing Techniques

Here, after brief descriptions of the cooperative WL, L and LRT techniques, we specialize them for both the CD and SCD approaches in presence of temporal dispersive RCs.

2.4.1 The Widely Linear Cooperative Technique

A WL cooperative technique consists in processing jointly, according to a certain criterion, the received vector at the radio front-end of an arbitrary CU and its conjugate version [72,77], regardless of the decision approach. Hence, by defining the augmented received vector as $\mathbf{y}_{\mathrm{a}}(l) \triangleq [\mathbf{y}^T(l)\, \mathbf{y}^H(l)]^T \in \mathbb{C}^{2ML_e}$, and the augmented processing vector as $\mathbf{f}^T \triangleq [\mathbf{t}^T\, \mathbf{q}^T]$, the WL test statistic can be written as:

$$d_{\mathrm{wl}}(l) = \mathbf{t}^H\, \mathbf{y}(l) + \mathbf{q}^H\, \mathbf{y}^*(l) = \mathbf{f}^H\, \mathbf{y}_{\mathrm{a}}(l) \tag{2.21}$$

with $\mathbf{q} = \mathbf{t}^*$, since $\mathbf{f}$ exhibits the conjugate symmetric property for real sensing data $\{u_i(q)\}$, [72]. For this, $d_{\mathrm{wl}}(l)$ results real.

Remark 6. In (2.21), $\mathbf{y}(l)$ is $\mathbf{y}_{\text{sc}}(l)$ given by (2.5), if the SCD is adopted, otherwise $\mathbf{y}(l)$ is $\mathbf{y}_c(l)$ given by (2.16). In the following, we omit the subscripts "c" and "sc" for describing the WL strategy regardless of the considered decision approach.

Since $\mathbf{y}(l)$ and $\mathbf{y}^*(l)$ are Gaussian, $d_{\text{wl}}(l)$ is Gaussian as well, with mean $\mu_{\text{wl}|\mathcal{H}_j} \triangleq E[d_{\text{wl}}(l)|\mathcal{H}_j]$ and variance $\varphi^2_{\text{wl}|\mathcal{H}_j} \triangleq \text{Var}[d_{\text{wl}}(l)|\mathcal{H}_j]$ equal to, respectively:

$$\mu_{\text{wl}|\mathcal{H}_j} = \mathbf{f}^H E[\mathbf{y}_{\text{a}}(l)|\mathcal{H}_j] \triangleq \mathbf{f}^H \widetilde{\boldsymbol{\mu}}_{\mathcal{H}_j} \tag{2.22}$$

$$\varphi^2_{\text{wl}|\mathcal{H}_j} = \mathbf{f}^H E[(\mathbf{y}_{\text{a}}(l) - \widetilde{\boldsymbol{\mu}})(\mathbf{y}_{\text{a}}(l) - \widetilde{\boldsymbol{\mu}})^H|\mathcal{H}_j]\mathbf{f} \triangleq \mathbf{f}^H \mathbf{C}_{\mathbf{y}_{\text{a}}|\mathcal{H}_j} \boldsymbol{f} \tag{2.23}$$

By denoting with $\mathbf{H}_{\text{a}} \triangleq [\mathbf{H}^T \mathbf{H}^H]^T$, $\widetilde{\boldsymbol{\mu}}_{\mathcal{H}_j} \in \mathbb{C}^{2ML_e}$ in (2.22) can be equivalently expressed as:

$$\widetilde{\boldsymbol{\mu}}_{\mathcal{H}_j} \triangleq E[\mathbf{y}_{\text{a}}(l)|\mathcal{H}_j] = \mathbf{H}_{\text{a}} \boldsymbol{\eta}_{\mathcal{H}_j} = [\boldsymbol{\mu}^T_{\mathcal{H}_j} \boldsymbol{\mu}^H_{\mathcal{H}_j}]^T \tag{2.24}$$

where, $\mathbf{H}$, $\boldsymbol{\eta}_{\mathcal{H}_j}$ and $\boldsymbol{\mu}_{\mathcal{H}_j}$ are given by (2.5) and (2.6) if the SCD is adopted, otherwise they are given by (2.16) and (2.17). By denoting with $\mathbf{R}_{\mathbf{n}_a} \triangleq \text{diag}[\mathbf{R}_{\mathbf{n}} \mathbf{R}_{\mathbf{n}}] \in \mathbb{R}^{2ML_e \times 2ML_e}$, the augmented covariance matrix $\boldsymbol{\mathcal{C}}_{\mathbf{y}_a|\mathcal{H}_j} \in \mathbb{C}^{2ML_e \times 2ML_e}$ in (2.23) of the received vector $\mathbf{y}_{\text{a}}$ can be equivalently expressed as:

$$\boldsymbol{\mathcal{C}}_{\mathbf{y}_{\text{a}}|\mathcal{H}_j} = \mathbf{H}_{\text{a}} \mathbf{C}_{\mathbf{u}|\mathcal{H}_j} \mathbf{H}^H_{\text{a}} + \mathbf{R}_{\mathbf{n}_{\text{a}}} = \begin{bmatrix} \mathbf{C}_{\mathbf{y}|\mathcal{H}_j} & \mathbf{C}_{\mathbf{y}^*|\mathcal{H}_j} \\ \mathbf{C}^*_{\mathbf{y}^*|\mathcal{H}_j} & \mathbf{C}^*_{\mathbf{y}|\mathcal{H}_j} \end{bmatrix} \tag{2.25}$$

with[7] $\mathbf{C}_{\mathbf{y}|\mathcal{H}_j}$ and $\mathbf{C}_{\mathbf{y}^*|\mathcal{H}_j}$ given by (2.10) and (2.13) for the SCD, otherwise by (2.18) and (2.20). Then, the decision on the PU presence is taken by comparing $d_{\text{wl}}(l)$ with a threshold γ_{wl}:

$$d_{\text{wl}}(l) \underset{\mathcal{H}_0}{\overset{\mathcal{H}_1}{\gtrless}} \gamma_{\text{wl}} \tag{2.26}$$

where γ_{wl} can be set to obtain a targeted false-alarm probability [72]. Clearly, the performance of the WL technique depends on the selected optimization criterion used to design $\mathbf{f}$. According to [72], we single

[7] Since a covariance matrix is positive definite, except in some degenerate cases of no interest, it is reasonable to assume the covariance matrices $\mathbf{C}_{\mathbf{y}|\mathcal{H}_j}$ and $\mathbf{C}_{\mathbf{y}^*|\mathcal{H}_j}$ invertible, in both the adopted decision approaches.

out $\mathbf{f}$ by maximizing the Deflection Coefficient (DC), i.e., the variance-normalized distance between the expectations of $d_{\text{wl}}(l)$. To avoid undetermined solutions, the DC is maximized under the $\mathbf{f}$ unit-norm constraint:

$$\max_{\mathbf{f}} \left\{ m^2_{\text{wl}}(\mathbf{f}) \triangleq \frac{[\mu_{\text{wl}|\mathcal{H}_1} - \mu_{\text{wl}|\mathcal{H}_0}]^2}{\varphi^2_{\text{wl}|\mathcal{H}_1}} \right\} = \\ = \max_{\mathbf{f}} \frac{[\mathbf{f}^H(\widetilde{\boldsymbol{\mu}}_{\mathcal{H}_1} - \widetilde{\boldsymbol{\mu}}_{\mathcal{H}_0})]^2}{\mathbf{f}^H \boldsymbol{C}_{\mathbf{y}_{\text{a}}|\mathcal{H}_1} \mathbf{f}}, \text{ subject to } \mathbf{f}^H\mathbf{f} = 1 \tag{2.27}$$

The WL Technique for the CD Approach

By adopting the CD approach, the solution of (2.27) coincides with the solution derived in [72] for a centralized cooperative sensing architecture. In fact, as underlined in Sec. 2.2, by using the CD approach in a centralized cooperative sensing architecture, Definition 1 agrees with the traditional decision approach. Hence the system model (2.16) formally coincides with the system model presented in [72]. For the sake of completeness, here we report the mentioned solution:

$$\mathbf{f}_{\text{wl-c}} = \begin{bmatrix} \mathbf{t}_{\text{wl-c}} \\ \mathbf{t}^*_{\text{wl-c}} \end{bmatrix} = \frac{\mathbf{C}^{-1}_{\mathbf{y}_{\text{c,a}}|\mathcal{H}_1} (\widetilde{\boldsymbol{\mu}}_{\text{c}|\mathcal{H}_1} - \widetilde{\boldsymbol{\mu}}_{\text{c}|\mathcal{H}_0})}{||\mathbf{C}^{-1}_{\boldsymbol{y}_{\text{c,a}}|\mathcal{H}_1} (\widetilde{\boldsymbol{\mu}}_{\text{c}|\mathcal{H}_1} - \widetilde{\boldsymbol{\mu}}_{\text{c}|\mathcal{H}_0})||^2_2} \tag{2.28}$$

with $\mathbf{C}_{\mathbf{y}_{\text{c,a}}|\mathcal{H}_1}$ and $\widetilde{\boldsymbol{\mu}}_{\text{c}|\mathcal{H}_j}$ given by (2.25) and (2.24), respectively (Remark 6). The maximized DC assured by $\mathbf{f}_{\text{wl-c}}$ is equal to:

$$m^2_{\text{wl-c}}(\mathbf{f}_{\text{wl-c}}) = (\widetilde{\boldsymbol{\mu}}_{\text{c}|\mathcal{H}_1} - \widetilde{\boldsymbol{\mu}}_{\text{c}|\mathcal{H}_0})^H \mathbf{C}^{-1}_{\mathbf{y}_{\text{c,a}}|\mathcal{H}_1} (\widetilde{\boldsymbol{\mu}}_{\text{c}|\mathcal{H}_1} - \widetilde{\boldsymbol{\mu}}_{\text{c}|\mathcal{H}_0}) \tag{2.29}$$

The WL Technique for the SCD Approach

By adopting the SCD approach, we can not proceed as in [72] to determine the solution of (2.27), since $\mathbf{C}_{\mathbf{y}_{\text{sc,a}}|\mathcal{H}_j} \in \mathbb{C}^{2ML_e \times 2ML_e}$ is rank-deficient, and hence, not invertible (Proposition 1). In Propositions 1 and 2, we show intermediate results, used in Theorem 5 to derive the solution of (2.27).

Proposition 1. The rank of the augmented covariance matrix $\mathbf{C}_{\mathbf{y}_{\text{sc,a}}|\mathcal{H}_j}$ is $(2\,M - 1)\,L_e$.

Proof. See Appendix E. □

We observe that the rank-deficiency of $\mathbf{C}_{\mathbf{y}_{\text{sc,a}}|\mathcal{H}_j}$ is a consequence of the stacked procedure (Appendix E and footnote 7).

Proposition 2. The optimized WL processing vector $\mathbf{f}_{\text{wl-sc}}$, maximizing the deflection coefficient when the SCD approach is adopted, is the solution of the following constrained maximization problem:

$$\max_{\mathbf{f}_{\text{sc}}} m^2_{\text{wl-sc}}(\mathbf{f}_{\text{sc}}) = \max_{\mathbf{f}_{\text{sc}}} \frac{[\mathbf{f}_{\text{sc}}^H(\widetilde{\boldsymbol{\mu}}_{\text{sc}|\mathcal{H}_1} - \widetilde{\boldsymbol{\mu}}_{\text{sc}|\mathcal{H}_0})]^2}{\mathbf{f}_{\text{sc}}^H \mathbf{C}_{\mathbf{y}_{\text{sc,a}}|\mathcal{H}_1} \mathbf{f}_{\text{sc}}},$$
$$\text{subject to} \quad \begin{cases} \mathbf{f}_{\text{sc}} \in \mathcal{R}(\boldsymbol{C}_{\mathbf{y}_{\text{sc,a}}|\mathcal{H}_1}) \\ \mathbf{f}_{\text{sc}}^H \mathbf{f}_{\text{sc}} = 1 \end{cases} \tag{2.30}$$

Proof. Since $\mathcal{R}(\mathbf{C}_{\mathbf{y}_{\text{sc,a}}|\mathcal{H}_1}) = \mathcal{R}(\mathbf{C}^H_{\mathbf{y}_{\text{sc,a}}|\mathcal{H}_1})$ and $\mathcal{N}(\mathbf{C}_{\mathbf{y}_{\text{sc,a}}|\mathcal{H}_1})$ are complementary orthogonal subspaces [78], any vector $\mathbf{f}_{\text{sc}} \in \mathbb{C}^{2\,M\,L_e}$ can be uniquely decomposed as $\mathbf{f}_{\text{sc}} = \mathbf{f}_{\mathcal{R}(\mathbf{C}_{\mathbf{y}_{\text{sc,a}}|\mathcal{H}_1})} + \mathbf{f}_{\mathcal{N}(\mathbf{C}_{\mathbf{y}_{\text{sc,a}}|\mathcal{H}_1})}$. The DC is not affected by $\mathbf{f}_{\mathcal{N}(\mathbf{C}_{\mathbf{y}_{\text{sc,a}}|\mathcal{H}_1})}$ since $(\widetilde{\boldsymbol{\mu}}_{\text{sc}|\mathcal{H}_1} - \widetilde{\boldsymbol{\mu}}_{\text{sc}|\mathcal{H}_0}) \in \mathcal{R}(\mathbf{H}_{\text{sc,a}}) \subseteq \mathcal{R}(\mathbf{C}_{\mathbf{y}_{\text{sc,a}}|\mathcal{H}_1})$, with $\widetilde{\boldsymbol{\mu}}_{\text{sc}|\mathcal{H}_j}$ in (2.24). Hence, the processing vector $\mathbf{f}_{\text{wl-sc}}$ maximizing the DC can be equivalently obtained by solving the problem (2.30). □

Theorem 5. The optimized WL processing vector $\mathbf{f}_{\text{wl-sc}}$, maximizing the deflection coefficient when the SCD approach is adopted, has the following expression:

$$\mathbf{f}_{\text{wl-sc}} = \begin{bmatrix} \mathbf{t}_{\text{wl-sc}} \\ \mathbf{t}^*_{\text{wl-sc}} \end{bmatrix} = \frac{\mathbf{C}^{\dagger}_{\mathbf{y}_{\text{sc,a}}|\mathcal{H}_1}(\widetilde{\boldsymbol{\mu}}_{\text{sc}|\mathcal{H}_1} - \widetilde{\boldsymbol{\mu}}_{\text{sc}|\mathcal{H}_0})}{||\mathbf{C}^{\dagger}_{\mathbf{y}_{\text{sc,a}}|\mathcal{H}_1}(\widetilde{\boldsymbol{\mu}}_{\text{sc}|\mathcal{H}_1} - \widetilde{\boldsymbol{\mu}}_{\text{sc}|\mathcal{H}_0})||_2^2} \tag{2.31}$$

where $\mathbf{C}^{\dagger}_{\mathbf{y}_{\text{sc,a}}|\mathcal{H}_1}$ is the Moore-Penrose inverse [78] of the augmented covariance matrix (2.25) and $\widetilde{\boldsymbol{\mu}}_{\text{sc}|\mathcal{H}_j}$ is given by (2.24).

Proof. See Appendix F □

By substituting (2.31) in the DC expression, it results that the maximized DC is equal to:

$$m^2_{\text{wl-sc}}(\mathbf{f}_{\text{wl-sc}}) = (\widetilde{\boldsymbol{\mu}}_{\text{sc}|\mathcal{H}_1} - \widetilde{\boldsymbol{\mu}}_{\text{sc}|\mathcal{H}_0})^H \mathbf{C}^{\dagger}_{\mathbf{y}_{\text{sc,a}}|\mathcal{H}_1}(\widetilde{\boldsymbol{\mu}}_{\text{sc}|\mathcal{H}_1} - \widetilde{\boldsymbol{\mu}}_{\text{sc}|\mathcal{H}_0}) \tag{2.32}$$

2.4.2 The Linear Cooperative Technique

The L cooperative technique consists in processing linearly, according to a certain criterion, the received vector at the radio front-end of an arbitrary CU [72], regardless of the adopted decision approach. By denoting with $\mathbf{w}$ the processing vector and accounting for Remark 6, the L complex test statistic is:

$$d(l) = \mathbf{w}^H \mathbf{y}(l) \tag{2.33}$$

The PU decision is taken by comparing the real part of $d(l)$ with a decision threshold γ_{l} [72]:

$$\text{Re}[d(l)] \underset{<}{\overset{>}{}}^{\mathcal{H}_1}_{\mathcal{H}_0} \gamma_{\text{l}} \tag{2.34}$$

where the real-part operator accounts for the real-nature of the transmitted symbols $\{u_i(q)\}$. Since $\mathbf{y}(l)$ is Gaussian, $\text{Re}[d(l)]$ is Gaussian too. By following similar reasonings as in [72], the mean $\mu_{\text{l}|\mathcal{H}_j}$ and the variance $\varphi^2_{\text{l}|\mathcal{H}_j}$ of $\text{Re}[d(l)]$ are equal to:

$$\mu_{\text{l}|\mathcal{H}_j} \triangleq E[\text{Re}[d(l)]|\mathcal{H}_j] = \text{Re}(\mathbf{w}^H \boldsymbol{\mu}_{\mathcal{H}_j}) \tag{2.35}$$

$$\varphi^2_{\text{l}|\mathcal{H}_j} \triangleq \text{Var}[\text{Re}[d(l)]|\mathcal{H}_j] = \frac{\mathbf{w}^H \mathbf{C}_{\mathbf{y}|\mathcal{H}_j} \mathbf{w} + \text{Re}[\mathbf{w}^H \mathbf{C}_{\mathbf{y}^*|\mathcal{H}_j} \mathbf{w}^*]}{2} \tag{2.36}$$

In (2.35), $\boldsymbol{\mu}_{\mathcal{H}_j}$ is given by (2.6) for the SCD approach, otherwise by (2.17). In (2.36), $\mathbf{C}_{\mathbf{y}|\mathcal{H}_j}$ and $\mathbf{C}_{\mathbf{y}^*|\mathcal{H}_j}$ are given by (2.10) and (2.13) for the SCD approach, otherwise by (2.18) and (2.20). As for the WL case, $\mathbf{w}$ is designed to maximize the DC:

$$\begin{aligned} &\max_{\mathbf{w}} m^2_{\text{l}}(\mathbf{w}) = \max_{\mathbf{w}} \left\{ \frac{|\mathbf{w}^H(\boldsymbol{\mu}_{\mathcal{H}_1} - \boldsymbol{\mu}_{\mathcal{H}_0})|^2}{\mathbf{w}^H \mathbf{C}_{\mathbf{y}|\mathcal{H}_1} \mathbf{w}} \right\} \\ &\text{subject to } \mathbf{w}^H \mathbf{w} = 1 \end{aligned} \tag{2.37}$$

The L Technique for the CD Approach

For the reasons underlined for the WL case, by adopting the CD approach, the solution of (2.37) coincides with the one derived in [72]. For the sake of completeness, here we report the mentioned solution:

$$\mathbf{w}_{\text{l-c}} = \frac{\mathbf{C}^{-1}_{\mathbf{y}_c|\mathcal{H}_1}(\boldsymbol{\mu}_{\text{c}|\mathcal{H}_1} - \boldsymbol{\mu}_{\text{c}|\mathcal{H}_0})}{||\mathbf{C}^{-1}_{\mathbf{y}_c|\mathcal{H}_1}(\boldsymbol{\mu}_{\text{c}|\mathcal{H}_1} - \boldsymbol{\mu}_{\text{c}|\mathcal{H}_0})||^2_2} \tag{2.38}$$

where $\boldsymbol{\mu}_{\mathrm{c}|\mathcal{H}_j}$ and $\mathbf{C}_{\mathbf{y}_c|\mathcal{H}_j}$ are reported in (2.17) and (2.18), respectively. The maximized DC assured by $\mathbf{w}_{\text{l-c}}$ is equal to:

$$m_{\mathrm{l}}^2(\mathbf{w}_{\text{l-c}}) = (\boldsymbol{\mu}_{\mathrm{c}|\mathcal{H}_1} - \boldsymbol{\mu}_{\mathrm{c}|\mathcal{H}_0})^H \mathbf{C}^{-1}_{\mathbf{y}_c|\mathcal{H}_1}(\boldsymbol{\mu}_{\mathrm{c}|\mathcal{H}_1} - \boldsymbol{\mu}_{\mathrm{c}|\mathcal{H}_0}) \tag{2.39}$$

The L Technique for the SCD Approach

By adopting the SCD approach, differently from the WL case, we can proceed similarly to [72] to determine the solution of (2.37), since $\mathbf{C}_{\mathbf{y}_{\mathrm{sc}}|\mathcal{H}_j}$ in (2.7) is invertible (footnote 7). For the sake of brevity we omit every step and we report only the result:

$$\mathbf{w}_{\text{l-sc}} = \frac{\mathbf{C}^{-1}_{\mathbf{y}_{\mathrm{sc}}|\mathcal{H}_1}(\boldsymbol{\mu}_{\mathrm{sc}|\mathcal{H}_1} - \boldsymbol{\mu}_{\mathrm{sc}|\mathcal{H}_0})}{||\mathbf{C}^{-1}_{\mathbf{y}_{\mathrm{sc}}|\mathcal{H}_1}(\boldsymbol{\mu}_{\mathrm{sc}|\mathcal{H}_1} - \boldsymbol{\mu}_{\mathrm{sc}|\mathcal{H}_0})||_2^2} \tag{2.40}$$

with $\boldsymbol{\mu}_{\mathrm{sc}|\mathcal{H}_j}$ and $\mathbf{C}_{\mathbf{y}_{\mathrm{sc}}|\mathcal{H}_j}$ given by (2.6) and (2.7), respectively. By substituting (2.40) in the DC definition, it results that the maximized DC is equal to:

$$m^2_{\text{l-sc}}(\mathbf{w}_{\text{l-sc}}) = (\boldsymbol{\mu}_{\mathrm{sc}|\mathcal{H}_1} - \boldsymbol{\mu}_{\mathrm{sc}|\mathcal{H}_0})^H \mathbf{C}^{-1}_{\mathbf{y}_{\mathrm{sc}}|\mathcal{H}_1}(\boldsymbol{\mu}_{\mathrm{sc}|\mathcal{H}_1} - \boldsymbol{\mu}_{\mathrm{sc}|\mathcal{H}_0}) \tag{2.41}$$

2.4.3 The LRT-Based Cooperative Technique

According to the Neyman-Pearson criterion, the optimum test consists in comparing the likelihood ratio of $\mathbf{y}(l)$ with a threshold to make the decision on the PU presence [76].

The LRT-Based Technique for the CD Approach

The LRT-based statistic $d_{\text{c-LRT}}(l)$, after some algebraic manipulations, assumes the quadratic form:

$$\begin{aligned} d_{\text{c-LRT}}(l) = {} & \mathbf{y}^H_{\mathrm{c,a}}(l) \left[\mathbf{C}^{-1}_{\mathbf{y}_{\mathrm{c,a}}|\mathcal{H}_0} - \mathbf{C}^{-1}_{\mathbf{y}_{\mathrm{c,a}}|\mathcal{H}_1}\right] \mathbf{y}_{\mathrm{c,a}}(l) + \\ & + 2\,\mathrm{Re}\left[\left(\widetilde{\boldsymbol{\mu}}^H_{\mathrm{c}|\mathcal{H}_1}\mathbf{C}^{-1}_{\mathbf{y}_{\mathrm{c,a}}|\mathcal{H}_1} - \widetilde{\boldsymbol{\mu}}^H_{\mathrm{c}|\mathcal{H}_0}\mathbf{C}^{-1}_{\mathbf{y}_{\mathrm{c,a}}|\mathcal{H}_0}\right)\mathbf{y}_{\mathrm{c,a}}(l)\right] \end{aligned} \tag{2.42}$$

with $\mathbf{C}_{\mathbf{y}_{\mathrm{c,a}}|\mathcal{H}_j}$ and $\widetilde{\boldsymbol{\mu}}_{\mathrm{c}|\mathcal{H}_j}$ given by (2.25) and (2.24). To derive (2.42), we used the PDF expression [82] of improper Gaussian random vectors and accounted for the definition of $\mathbf{y}_{\mathrm{c,a}}(l)$.

The LRT-Based Technique for the SCD Approach

The LRT-based statistic $d_{\text{sc-LRT}}(l)$, after some algebraic manipulations, assumes the quadratic form:

$$\begin{aligned} d_{\text{sc-LRT}}(l) &= \mathbf{y}_{\text{sc,a}}^{H}(l)\left[\mathbf{C}^{\dagger}_{\mathbf{y}_{\text{sc,a}}|\mathcal{H}_0} - \mathbf{C}^{\dagger}_{\mathbf{y}_{\text{sc,a}}|\mathcal{H}_1}\right]\mathbf{y}_{\text{sc,a}}(l) + \\ &+ 2\,\text{Re}\left[\left(\widetilde{\boldsymbol{\mu}}^{H}_{\text{sc}|\mathcal{H}_1}\,\mathbf{C}^{\dagger}_{\mathbf{y}_{\text{sc,a}}|\mathcal{H}_1} - \widetilde{\boldsymbol{\mu}}^{H}_{\text{sc}|\mathcal{H}_0}\mathbf{C}^{\dagger}_{\mathbf{y}_{\text{sc,a}}|\mathcal{H}_0}\right)\mathbf{y}_{\text{sc,a}}(l)\right] \end{aligned} \tag{2.43}$$

In (2.43), since $\mathbf{C}_{\mathbf{y}_{\text{sc,a}}|\mathcal{H}_j}$ is rank-deficient, we used the degenerate PDF expression [83] of improper Gaussian random vectors.

Remark 7. Since, as well known, finding the optimal threshold for the LRT test is not mathematically tractable, to prove that the LRT-based technique exhibits the threshold behavior as a function of the adopted decision approach we proceed numerically in Sec. 2.6.

2.5 The Decision Approach Threshold Behavior

Here, we prove the main result of this paper: the detection accuracy exhibits a threshold behavior as a function of the adopted decision approach, regardless of the underlying cooperative sensing architecture. Then, the analytical results are discussed at the end of the section.

2.5.1 Threshold Behavior for the WL Cooperative Technique

To prove the main result of Sec. 2.5.1, i.e., Theorem 6, Proposition 3 is needed. For this, let us introduce the following definitions of the matrices $\overline{\boldsymbol{\Omega}} \in \mathbb{C}^{(M-1)L_e\times(M-1)L_e}$ and $\boldsymbol{\Omega}_{\text{c}} \in \mathbb{C}^{L_e\times L_e}$:

$$\begin{aligned} \overline{\boldsymbol{\Omega}} &\triangleq \left(\mathbf{C}_{\overline{\mathbf{y}}|\mathcal{H}_1} - \mathbf{C}_{\overline{\mathbf{y}}^*|\mathcal{H}_1}(\mathbf{C}^{*}_{\overline{\mathbf{y}}|\mathcal{H}_1})^{-1}\mathbf{C}^{*}_{\overline{\mathbf{y}}^*|\mathcal{H}_1}\right)^{-1} \\ \boldsymbol{\Omega}_{\text{c}} &\triangleq \left(\mathbf{C}_{\mathbf{y}_1|\mathcal{H}_1} - \mathbf{C}_{\mathbf{y}_1^*|\mathcal{H}_1}(\mathbf{C}^{*}_{\mathbf{y}_1|\mathcal{H}_1})^{-1}\mathbf{C}^{*}_{\mathbf{y}_1^*|\mathcal{H}_1}\right)^{-1} \end{aligned} \tag{2.44}$$

with $\mathbf{C}_{\overline{\mathbf{y}}|\mathcal{H}_j}$, $\mathbf{C}_{\overline{\mathbf{y}}^*|\mathcal{H}_j}$, $\mathbf{C}_{\mathbf{y}_1|\mathcal{H}_j}$ and $\mathbf{C}_{\mathbf{y}_1^*|\mathcal{H}_j}$ given by (2.12), (2.14), (2.19) and (2.20), respectively.

Proposition 3. The optimized WL sub-vectors $\mathbf{t}_{\text{wl-c}}$ and $\mathbf{t}_{\text{wl-sc}}$ for the CD and SCD approaches, given in (2.28) and (2.31), respectively, can

be expressed as:

$$\begin{aligned}\mathbf{t}_{\text{wl-c}} &= \frac{\boldsymbol{\Sigma}_{\text{wl-c}}\left(\boldsymbol{\eta}_{\text{c}|\mathcal{H}_1}-\boldsymbol{\eta}_{\text{c}|\mathcal{H}_0}\right)}{\sqrt{2}\left|\left|\boldsymbol{\Sigma}_{\text{wl-c}}\left(\boldsymbol{\eta}_{\text{c}|\mathcal{H}_1}-\boldsymbol{\eta}_{\text{c}|\mathcal{H}_0}\right)\right|\right|_2^2}\\ \mathbf{t}_{\text{wl-sc}} &= \frac{\boldsymbol{\Sigma}_{\text{wl-sc}}\left(\boldsymbol{\eta}_{\text{sc}|\mathcal{H}_1}-\boldsymbol{\eta}_{\text{sc}|\mathcal{H}_0}\right)}{\sqrt{2}\left|\left|\boldsymbol{\Sigma}_{\text{wl-sc}}\left(\boldsymbol{\eta}_{\text{sc}|\mathcal{H}_1}-\boldsymbol{\eta}_{\text{sc}|\mathcal{H}_0}\right)\right|\right|_2^2}\end{aligned} \tag{2.45}$$

with $\boldsymbol{\eta}_{\text{c}|\mathcal{H}_j}$ and $\boldsymbol{\eta}_{\text{sc}|\mathcal{H}_j}$ reported in (2.17) and (2.6), respectively, and $\boldsymbol{\Sigma}_{\text{wl-c}}$ and $\boldsymbol{\Sigma}_{\text{wl-sc}}$ are equal to, respectively,

$$\boldsymbol{\Sigma}_{\text{wl-c}} = \begin{bmatrix} \boldsymbol{\Omega}_{\text{c}}\,\mathbf{H}_1 - \mathbf{C}^{-1}_{\mathbf{y}_1|\mathcal{H}_1}\mathbf{C}_{\mathbf{y}_1^*|\mathcal{H}_1}\boldsymbol{\Omega}_{\text{c}}^*\,\mathbf{H}_1^* & \mathbf{0}_{L_e\times(M-1)\,(L_e+L_g-1)} \\ \mathbf{0}_{(M-1)L_e\times(L_e+L_g-1)} & \overline{\boldsymbol{\Omega}}\,\overline{\mathbf{H}} - \mathbf{C}^{-1}_{\overline{\mathbf{y}}|\mathcal{H}_1}\mathbf{C}_{\overline{\mathbf{y}}^*|\mathcal{H}_1}\overline{\boldsymbol{\Omega}}^*\,\overline{\mathbf{H}}^* \end{bmatrix} \tag{2.46}$$

$$\boldsymbol{\Sigma}_{\text{wl-sc}} = \begin{bmatrix} \frac{1}{2}\,\mathbf{C}^{-1}_{\mathbf{y}_0|\mathcal{H}_1}\mathbf{H}_0 & \mathbf{0}_{L_e\times(M-1)\,(L_e+L_g-1)} \\ \mathbf{0}_{(M-1)\,L_e\times(L_e+L_g-1)} & \overline{\boldsymbol{\Omega}}\,\overline{\mathbf{H}} - \mathbf{C}^{-1}_{\overline{\mathbf{y}}|\mathcal{H}_1}\mathbf{C}_{\overline{\mathbf{y}}^*|\mathcal{H}_1}\overline{\boldsymbol{\Omega}}^*\,\overline{\mathbf{H}}^* \end{bmatrix} \tag{2.47}$$

In (2.46) and (2.47), $\mathbf{C}_{\mathbf{y}_0|\mathcal{H}_j}$ is given in (2.12), $\overline{\mathbf{H}}$ and $\mathbf{H}_1$ are defined in Sec. 2.3.

Proof. See Appendix G. □

Theorem 6. The WL cooperative technique implemented according to the SCD approach assures higher (lower) detection accuracy than the WL cooperative technique implemented according to the CD approach if and only if $\theta_{\text{wl}} > 1$ ($\theta_{\text{wl}} < 1$), where θ_{wl} is a positive[8] scalar quantity equals to:

$$\theta_{\text{wl}} \triangleq \frac{\left(\nu_{0|\mathcal{H}_1}-\nu_{0|\mathcal{H}_0}\right)^2\zeta^{-1}_{0|\mathcal{H}_1}L_e}{2\left(\nu_{1|\mathcal{H}_1}-\nu_{1|\mathcal{H}_0}\right)^2\mathbf{1}^T_{\{L_e+L_g-1\}}\text{Re}\left[\mathbf{H}_1^H\left(\boldsymbol{\Omega}_{\text{c}}\,\mathbf{H}_1-\mathbf{C}^{-1}_{\mathbf{y}_1|\mathcal{H}_1}\mathbf{C}_{\mathbf{y}_1^*|\mathcal{H}_1}\boldsymbol{\Omega}_{\text{c}}^*\mathbf{H}_1^*\right)\right]\mathbf{1}_{\{L_e+L_g-1\}}} \tag{2.48}$$

In (2.48), $\nu_{k|\mathcal{H}_j}$ and $\zeta_{k|\mathcal{H}_j}$ are given by (2.2).

Proof. See Appendix H. □

Remark 8. As proved in Appendix H, when $\theta_{\text{wl}} = 1$ the detection accuracy assured by the WL cooperative technique implemented according to the CD approach coincides with the detection accuracy assured by the WL technique implemented according to the SCD approach. Thus, $\theta_{\text{wl}} = 1$ constitutes the searched threshold value of the WL detection accuracy.

[8]The positive nature of θ_{wl} is discussed in Appendix H.

Corollary 1. The threshold θ_{wl} (2.48) depends only on the statistics and the channel characteristics of CU_0 and CU_1.

Proof. It follows directly from the proof of Theorem 6 given in Appendix H. □

Remark 9. The results of Corollary 1 agree with the intuition. In fact, the $(M-1)$ cooperative CUs, denoted with $\text{CU}_2,\ldots,\text{CU}_M$, affect the performance of both the CD and SCD implementations of the WL technique in the same way. This means that, although the performance of both the implementations improves as the number M of cooperative CUs grows, the threshold value does not change, as confirmed by the numerical results in Sec. 2.6.

Remark 10. From (2.48), it is immediate to verify that if $L_{g_1} \to \infty$ (with $L_e < \infty$), i.e., if the RC established in the CD approach between CU_1 and CU_0 has a infinite memory, $\theta_{\text{wl}} \to 0$. This means that the CD approach outperforms the SCD one, i.e., it assures higher detection accuracy than the SCD approach, regardless of the CU_1 sensing channel conditions. In other words, it is always more advantageous in terms of detection accuracy involving another CU in the cooperative process rather than using the local sensing statistic of the decision maker CU_0, independently of the sensing channel conditions. This surprising result suggests that frequency-selective fading on the RC introduces degrees of freedom that the CD approach is able to exploit. In practice, it is enough $L_{g_1} >> 1$, in the order of 10 in operative conditions of practical interest, to assure this behavior (see Sec. 2.6).

Remark 11. From (2.48), it results that if the noise power on the CU_0 sensing channel goes to infinity, $\sigma_0^2 \to \infty$, $\theta_{\text{wl}} \to 0$, i.e., the CD approach assures higher detection accuracy than the SCD one, regardless of the CU_1 RC conditions. Hence, it is more convenient involving CU_1 in the cooperative process rather than using the local statistic of CU_0, affected by deep noise. Clearly, if $\sigma_1^2 \to \infty$, $\theta_{\text{wl}} \to \infty$, i.e., the CD approach behavior is inverted with respect to the one described. In practice, it is enough $\sigma_1^2 >> \sigma_0^2$, to assure this behavior in operative conditions of practical interest (see Sec. 2.6).

Remark 12. When the noise power δ_1^2 of CU_1 at CU_0 side goes to infinite, i.e., $\delta_1^2 \to +\infty$, $\theta_{\text{wl}} \to +\infty$ as well, i.e., the SCD approach outperforms the CD one. This suggests that if the RC noise power increases

significantly, it is more advantageous using the sensing statistic of CU_0, not affected by the RC impairments, than involving another CU in the cooperative process, independently of the SC conditions. In practice, it is enough $\delta_1^2 >> 0$ to assure this behavior in operative conditions of practical interest (see Sec. 2.6).

Corollary 2. If $L_{g_1} \to 1$, i.e., if the RC established between CU_1 and CU_0 in the CD approach is not temporal dispersive, we have:

$$\lim_{L_{g_1}\to 1} \theta_{\mathrm{wl}} = \frac{|g_0|^4 \, \zeta_{0|\mathcal{H}_1}^{-1}}{|g_1|^4 \frac{2\,|h_1|^2}{2\,|h_1|^2\,\zeta_{1|\mathcal{H}_1}+\delta_1^2}} \tag{2.49}$$

Proof. By using (2.19), (2.20) and $\mathbf{H}_1 = h_1\,\mathbf{I}_{L_e}$ when $L_{g_1} \to 1$, (2.49) is achieved. □

Remark 13. From (2.49) it results that:

$$\lim_{\delta_1^2\to 0} \left\{ \lim_{L_{g_1}\to 1} \theta_{\mathrm{wl}} \right\} = \frac{|g_0|^4 \, \zeta_{0|\mathcal{H}_1}^{-1}}{|g_1|^4 \, \zeta_{1|\mathcal{H}_1}^{-1}} \tag{2.50}$$

Therefore, when the RC between CU_1 and CU_0 is ideal, the detection accuracy threshold depends only on the sensing channel propagation effects of CU_0 and CU_1, as expected.

2.5.2 Threshold Behavior for the L Cooperative Technique

To prove the main result of Sec. 2.5.2, i.e., Theorem 7, Proposition 4 is needed.

Proposition 4. The optimized L vectors $\mathbf{w}_{\text{l-c}}$ and $\mathbf{w}_{\text{l-sc}}$ for the CD and the SCD approaches, given in (2.38) and (2.40), respectively, can be expressed as:

$$\begin{aligned} \mathbf{w}_{\text{l-c}} &= \frac{\boldsymbol{\Sigma}_{\text{l-c}} \left(\boldsymbol{\eta}_{\text{c}|\mathcal{H}_1} - \boldsymbol{\eta}_{\text{c}|\mathcal{H}_0}\right)}{||\boldsymbol{\Sigma}_{\text{l-c}} \left(\boldsymbol{\eta}_{\text{c}|\mathcal{H}_1} - \boldsymbol{\eta}_{\text{c}|\mathcal{H}_0}\right)||_2^2} \\ \mathbf{w}_{\text{l-sc}} &= \frac{\boldsymbol{\Sigma}_{\text{l-sc}} \left(\boldsymbol{\eta}_{\text{sc}|\mathcal{H}_1} - \boldsymbol{\eta}_{\text{sc}|\mathcal{H}_0}\right)}{||\boldsymbol{\Sigma}_{\text{l-sc}} \left(\boldsymbol{\eta}_{\text{sc}|\mathcal{H}_1} - \boldsymbol{\eta}_{\text{sc}|\mathcal{H}_0}\right)||_2^2} \end{aligned} \tag{2.51}$$

with $\boldsymbol{\eta}_{\mathrm{c}|\mathcal{H}_j}$ and $\boldsymbol{\eta}_{\mathrm{sc}|\mathcal{H}_j}$ reported in (2.17) and (2.6), respectively, and $\boldsymbol{\Sigma}_{\text{l-c}}$ and $\boldsymbol{\Sigma}_{\text{l-sc}}$ equal to:

$$\boldsymbol{\Sigma}_{\text{l-c}} = \begin{bmatrix} \mathbf{C}^{-1}_{\mathbf{y}_{1|\mathcal{H}_1}} \mathbf{H}_1 & \mathbf{0}_{L_e \times (M-1)(L_e+L_g-1)} \\ \mathbf{0}_{(M-1)L_e \times (L_e+L_g-1)} & \mathbf{C}^{-1}_{\overline{\mathbf{y}}|\mathcal{H}_1} \overline{\mathbf{H}} \end{bmatrix} \tag{2.52}$$

$$\boldsymbol{\Sigma}_{\text{l-sc}} = \begin{bmatrix} \mathbf{C}^{-1}_{\mathbf{y}_{0|\mathcal{H}_1}} \mathbf{H}_0 & \mathbf{0}_{L_e \times (M-1)(L_e+L_g-1)} \\ \mathbf{0}_{(M-1)L_e \times (L_e+L_g-1)} & \mathbf{C}^{-1}_{\overline{\mathbf{y}}|\mathcal{H}_1} \overline{\mathbf{H}} \end{bmatrix} \tag{2.53}$$

Proof. The proof follows after some algebraic manipulations, by exploiting (2.38) and (2.40) and by using the lemma for the inverse of a partitioned matrix [61]. □

Theorem 7. The L cooperative technique implemented according to the SCD approach assures higher (lower) detection accuracy than the L cooperative technique implemented according to the CD approach, if and only if $\theta_{\text{l}} > 1$ ($\theta_{\text{l}} < 1$), where θ_{l} is a positive scalar quantity equal to:

$$\theta_{\text{l}} \triangleq \frac{\left(\nu_{0|\mathcal{H}_1} - \nu_{0|\mathcal{H}_0}\right)^2 \zeta^{-1}_{0|\mathcal{H}_1} L_e}{\left(\nu_{1|\mathcal{H}_1} - \nu_{1|\mathcal{H}_0}\right)^2 \mathbf{1}^T_{\{L_e+L_g-1\}} \mathbf{H}_1^H \mathbf{C}^{-1}_{\mathbf{y}_1|\mathcal{H}_1} \mathbf{H}_1 \mathbf{1}_{\{L_e+L_g-1\}}} \tag{2.54}$$

Proof. The proof is achieved by reasoning as for Theorem 6 and by using (2.51). □

Remark 14. Similarly to the WL case, when $\theta_{\text{l}} = 1$ the detection accuracy assured by the L cooperative technique implemented according to the CD approach coincides with the detection accuracy assured by the L technique implemented according to the SCD approach. Thus, $\theta_{\text{l}} = 1$ constitutes the searched threshold value of the L detection accuracy.

Corollary 3. The threshold θ_{l} (2.54) depends only on the statistics and the channel characteristics of CU_0 and CU_1.

Proof. It follows directly from Theorem 7. □

Remark 15. The results of Corollary 3 agree with the intuition. In fact, the $(M-1)$ cooperative CUs, denoted with $\mathrm{CU}_2, \ldots, \mathrm{CU}_M$, affect the performance of both the CD and SCD implementations of the L technique in the same way. This means that, although the performance

of both the implementations improves as the number M of cooperative CUs grows, the threshold value does not change, as confirmed by the numerical results in Sec. 2.6. Moreover, Remarks 10, 11 and 12 hold also for the L cooperative technique.

Corollary 4. If $L_{g_1} \to 1$, i.e., if the RC established between CU_1 and CU_0 in the CD approach is not temporal dispersive, we have:

$$\lim_{L_{g_1}\to 1} \theta_{\mathrm{l}} = \frac{|g_0|^4 \, \zeta_{0|\mathcal{H}_1}^{-1}}{|g_1|^4 \frac{|h_1|^2}{|h_1|^2 \zeta_{1|\mathcal{H}_1} + \delta_1^2}} \tag{2.55}$$

Proof. The proof follows the same guidelines used for Corollary 2. □

If $\delta_1^2 \to 0$, θ_{l} is given by (2.50) and Remark 13 still holds.

2.5.3 Result Discussion

Stemming from the developed analysis, we can make some considerations. For example, if the local noise levels on the SCs and/or the RCs are known a priori (possibly from experimental measurements when the primary system is turned off, or from some previous experience), then it is possible to have a-priori insights to choose the decision approach for an arbitrary cooperative technique. In other words, having some a-priori information on the environment provides guidelines on the decision approach to adopt. This is very important, since the choice between the two approaches affects not only the detection accuracy of an arbitrary cooperative sensing technique, but also the entire CR network efficiency/performance, involving crucial trade-off reasonings. In fact, in the CD approach, the decision maker is not involved in the sensing process, thus being able to perform other CR tasks during its cooperators' sensing time. However, since another CU is involved in the cooperative process, the coordination cost increases. Differently, in the SCD approach, the decision maker is directly involved in the sensing process. Consequently, the coordination cost decreases but the decision maker cannot perform other CR tasks during its cooperators' sensing time.

2.6 Performance Evaluation

Here, we validate the derived analytical results by extensive Monte Carlo simulations. Specifically, first, we validate the proposed WL and

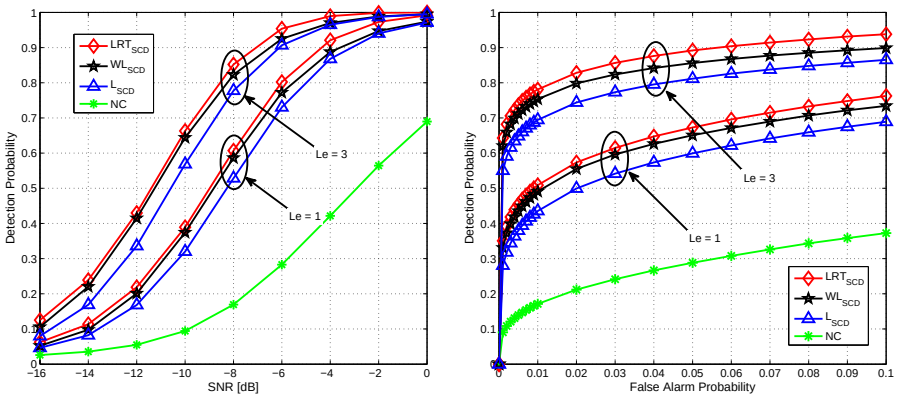

Figure 2.2: Experiment 1: Detection Probability (P_{det}) versus the SNR (left-side plot) and versus the False-Alarm Probability (P_f) (right-side plot), for different values of L_e, for the SCD approach.

L cooperative sensing techniques implemented by adopting the SCD approach[9], then we validate the existence of the threshold behavior in the detection accuracy as a function of the adopted decision approach, for all the sensing techniques considered in Sec. 2.4. Each experiment consists in 10^6 independent Monte Carlo runs, and in each run the noise samples, the sensing channels $\{g_i\}_{i=1}^{M}$ and the tap values of the FIR filters, modeling the RCs, are randomly and independently generated according to a zero-mean complex Gaussian distribution. For simplicity, $s(k) = 1$. The average SNR at each CU is defined as [72, 81]: $\{\text{SNR}_i\}_{i=1}^{M} = E[|g_i|^2]\, E_s/(N\, \sigma_i^2)$.

Experiment 1: the left-side of Fig. 2.2 shows the detection probability P_{det} versus (vs) the SNR, for a fixed value of the false-alarm probability $P_f = 10^{-2}$ and for two different values of L_e[10]. The noise variances of

[9]The WL and L cooperative sensing techniques implemented by adopting the CD approach do not need to be validated, since as highlighted in Sec. 2.4, they perform as the techniques in [72].

[10]Let us recall the main notations adopted through the paper: L_e is the number of jointly elaborated received samples for each CU, N is the number of samples available in the sensing time, M is the number of cooperative CUs, L_{g_i} is the length of the finite multi-path channel impulse response between the i-th CU and CU_0, $L_g \triangleq \max_{i=2}^{M} L_{g_i}$, δ_i^2 is the noise variance for the i-th RC, and finally σ_i^2 is the noise variance for the i-th sensing channel.

each CU at CU_0 side are set equal to $\delta_2^2 = 0.1$, $\delta_3^2 = 0.2$ and $\delta_4^2 = 0.4$. Moreover, an additional non-cooperative (NC) sensing technique is considered, in which CU_0 takes the decision based only on its local energy. The results show that the cooperative techniques perform notably better than the NC one, as expected, and that the WL detector outperforms the L one in operative conditions of practical interest, i.e., for low SNR values, assuring so less interference on the PU. The WL gain is justified by its capacity to exploit the information contained in the statistical pseudocovariance of the received signal. Plus, for both the L_e values, the WL detector performs almost comparable with the optimal LRT, but with a significantly lower computational complexity.

Instead, the right side of Fig. 2.2 shows P_{det} vs P_f, with the same previous simulation setting. The SNR is different for each CU to analyze how different sensing capabilities can affect the global decision, and it is set as: $\text{SNR}_0 = -8$ dB, $\text{SNR}_2 = -8.6$ dB, $\text{SNR}_3 = -9.2$ dB, $\text{SNR}_4 = -10$ dB. The results confirm the performance gain of the WL detector with respect to the L one, and the capability of the cooperative strategies, implemented by adopting the SCD approach, to counteract the channel impairments.

In the following, we conduct several experiments to substantiate the threshold behavior of the detection accuracy as a function of the adopted decision approach, by varying different sensing and reporting channel parameters encapsulated in the non-linear forms (2.48) and (2.54). For all the experiments, $P_f = 10^{-2}$, $N = 60$.

Experiment 2: Figs. 2.4, show P_{det} vs the ratio σ_1^2/σ_0^2 between the noise variances of CU_0 and CU_1 on the SCs, for all the considered cooperative sensing techniques and for different values of L_e, when $M = 3$. The results are obtained by fixing $\text{SNR}_0 = -8$ dB, i.e., by fixing σ_0^2, and letting σ_1^2 to vary. The SNR and the noise variances are set as follows: $\text{SNR}_2 = -8.6$ dB, $\text{SNR}_3 = -9.2$ dB, $\delta_1^2 = 0.8$, $\delta_2^2 = 0.2$ and $\delta_3^2 = 0.4$. In the figures, the red squares denote the points in which the two decision approaches perform the same, i.e, the threshold values in terms of σ_1^2/σ_0^2. The results confirm the presence of the threshold behavior for the detection accuracy, regardless of the considered cooperative sensing technique. In particular, for all the considered techniques, when L_e increases, the threshold value in terms of σ_1^2/σ_0^2 decreases. This agrees with the intuition, in fact, when L_e increases, the SCD approach bene-

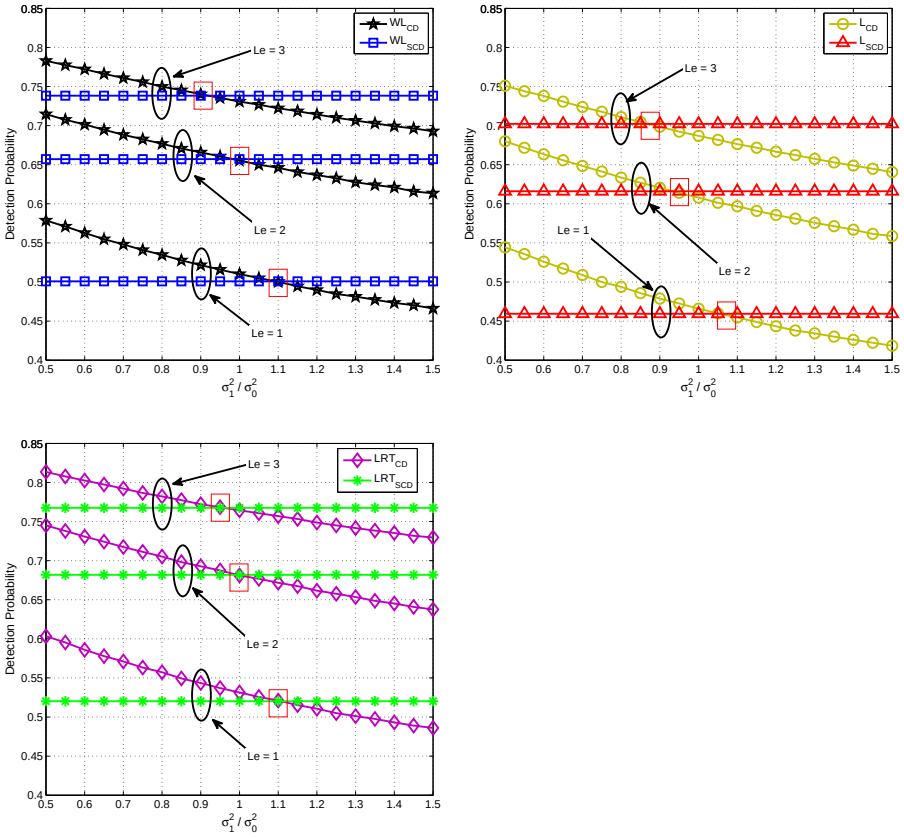

Figure 2.3: Experiment 2: Detection Probability (P_{det}) versus the ratio between the noise variances of CU_0 and CU_1 on the Sensing Channels (σ_1^2/σ_0^2), for different values of L_e, and for the WL strategy (upper-left-side plot), L strategy (upper-right-side plot), and LRT strategy (lower-side plot).

fits from processing an increased number of local sensing statistics not affected by the RC impairments. Hence, for smaller values of σ_1^2/σ_0^2, the SCD is able to outperform the CD. Moreover, it is confirmed the validity of Remark 11 for all the considered cooperative techniques.

Experiment 3: Figs. 2.4, show P_{det} vs σ_1^2/σ_0^2, for different values of M, when $L_e = 2$, $\text{SNR}_4 = -10$ dB, $\delta_4^2 = 0.6$, and the remaining parameters are set according to Experiment 3. For all the cooperative techniques, the results show that when the number M of cooperative

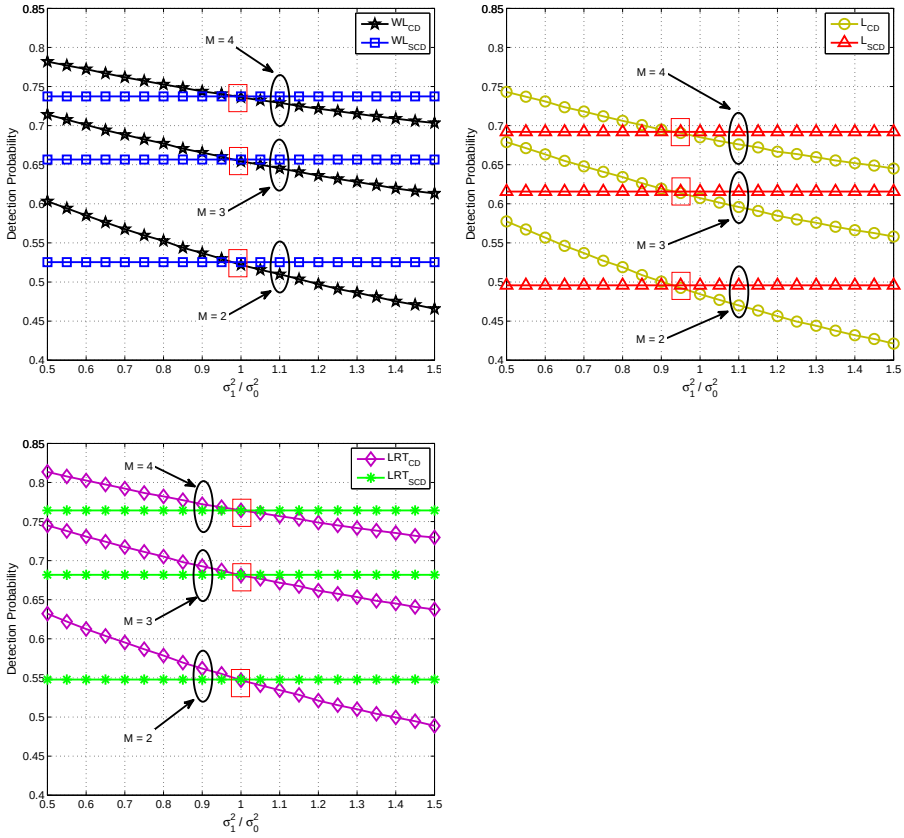

Figure 2.4: Experiment 3: Detection Probability (P_{det}) versus the ratio between the noise variances of CU_0 and CU_1 on the Sensing Channels (σ_1^2/σ_0^2), for different values of M, and for the WL strategy (upper-left-side plot), L strategy (upper-right-side plot), and LRT strategy (lower-side plot).

SCUs increases, the threshold value in terms of σ_1^2/σ_0^2 does not change. This agrees with the analytical results (Corollary 1 and 3), assuring that cooperative CUs different from CU_0 and CU_1 affect the performance of both the decision approaches in the same way.

Experiment 4: Figs. 2.5, show P_{det} vs δ_1^2, i.e., vs the CU_1 noise variance at CU_0 side, for all the considered cooperative sensing techniques and for different values of L_{g_1}, when $M = 3$ and $M = 4$, $L_e = 1$, and $\sigma_1^2/\sigma_0^2 = 1$. The SNRs are set according to Experiment 1 (right-

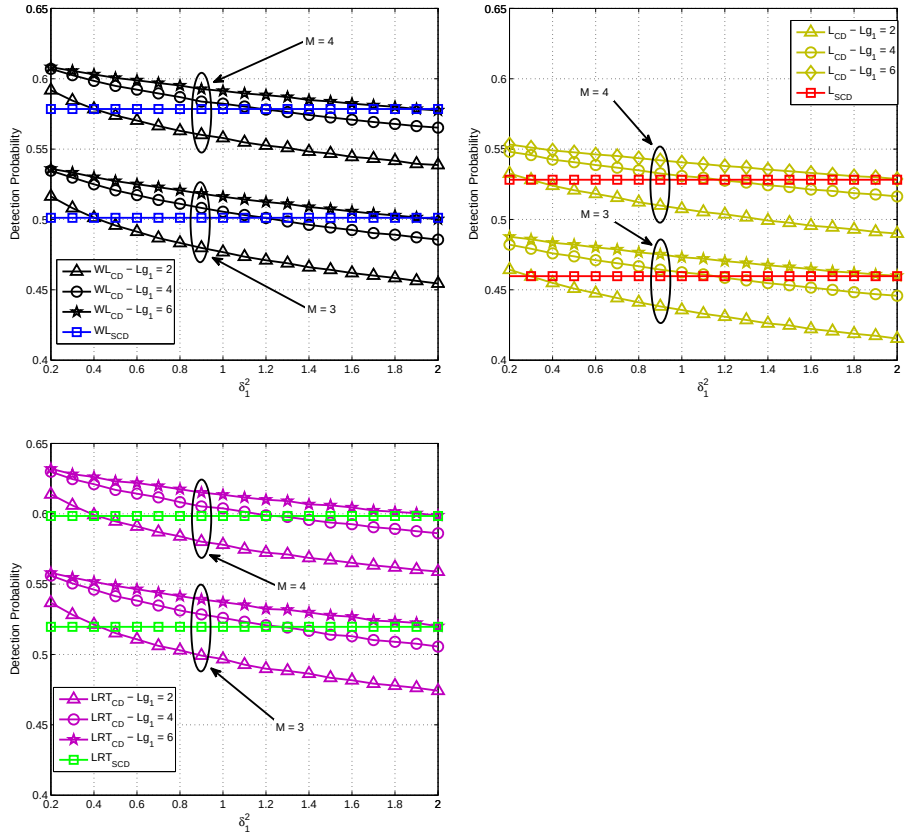

Figure 2.5: Experiment 4: Detection Probability (P_{det}) versus the noise variance at CU_0 on the Reporting Channel corresponding to CU_1 (δ_1^2), for different values of L_{g_1}, and for the WL strategy (upper-left-side plot), L strategy (upper-right-side plot), and LRT strategy (lower-side plot).

side plot) and the noise variances of the remain CUs are set equal to $\delta_2^2 = 0.2$, $\delta_3^2 = 0.4$ and $\delta_4^2 = 0.6$. Clearly, the performances of the cooperative techniques implemented by adopting the SCD approach do not depend on L_{g_1} and δ_1^2, as confirmed by the performance curves parallel to the abscissa axis. The results show that when L_{g_1} increases, the threshold value in terms of δ_1^2 increases as well, in agreement with Remark 10 and Corollary 3 for all the considered cooperative techniques. This means that when L_{g_1} increases, the CD approach assures higher detection accuracy than the SCD one for a wider range of δ_1^2 values. It

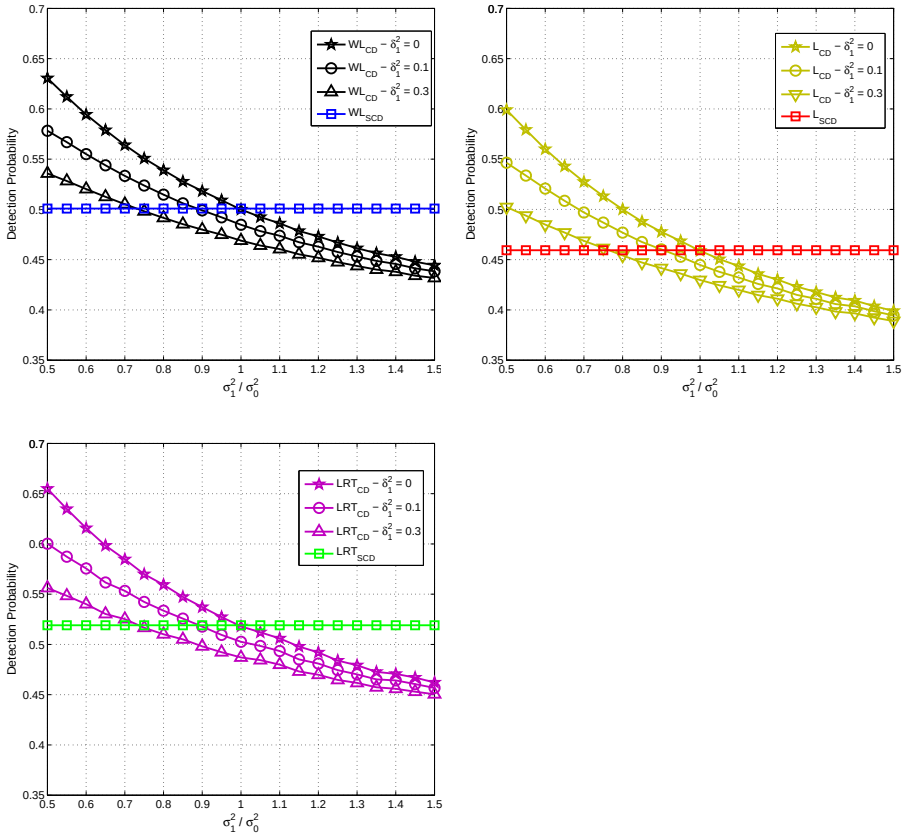

Figure 2.6: Experiment 5: Detection Probability (P_{det}) versus the ratio between the noise variances of CU_0 and CU_1 on the Sensing Channels (σ_1^2/σ_0^2) when $L_{g_1} \to 1$, and for the WL strategy (upper-left-side plot), L strategy (upper-right-side plot), and LRT strategy (lower-side plot).

is confirmed that the multipath fading on the RC introduces degrees of freedom that the cooperative strategies implemented according to the CD approach are able to exploit.

Experiment 5: Finally, Figs. 2.6, show P_{det} vs σ_1^2/σ_0^2, when $L_{g_1} \to 1$, i.e., when the RC between CU_0 and CU_1 is not temporal dispersive, for different values of the CU_1 noise power δ_1^2 at the CU_0 side, $M = 3$ and $L_e = 1$ (the SNRs and $\{\delta_i\}_{i=2}^3$ are set as in the previous experiment). The results confirm again the presence of the threshold behavior for

the detection accuracy, regardless of the considered cooperative sensing technique. Moreover, when δ_1^2 increases, the threshold value in terms of σ_1^2/σ_0^2 decreases, as expected. This means that the SCD approach outperforms the CD one for smaller value of σ_1^2/σ_0^2. In fact, when δ_1^2 increases, the propagation conditions on the RC between CU_1 and CU_0 worsen, and therefore, it is enough a small degradation of the CU_1 sensing conditions (increased σ_1^2) to have a significant performance loss by adopting the CD approach with respect to the SCD one (Remark 12).

2.7 Conclusions

Cooperative spectrum sensing techniques are mainly based on two different decision approaches, according to the role of the decision maker: the *Combining Decision* approach and the *Sensing & Combining Decision* approach. The choice of the decision approach deeply affects the performance of any cooperative spectrum sensing technique. Thus, in this chapter, by accounting for the effects of realistic channel propagation, a theoretical analysis has been developed to single out the criteria for choosing the decision approach that maximizes the detection accuracy of an arbitrary cooperative technique, regardless of the underlying cooperative sensing architecture. Specifically, it has been proved that the detection accuracy exhibits a threshold behavior as a function of the adopted decision approach, i.e., it exists a threshold value depending on the sensing and reporting channel parameters that determines two different operating regions. In one region, the higher detection accuracy is assured by implementing the cooperative sensing technique according to the *Combining Decision* approach, whereas in the other region, the higher detection accuracy is guaranteed by the *Sensing & Combining Decision* approach, regardless of the underlying cooperative sensing architecture. Closed-form expressions of the threshold are analytically derived, and practical insights for the decision approach selection have been provided.

Chapter 3

Spatio-Temporal Spectrum Sensing Design for Cognitive Radio Networks with Primary-User Mobility

3.1 Introduction

In Cognitive Radio Networks, spectrum opportunities can be classified as temporal or spatial opportunities [84]: a temporal opportunity is defined as the time interval in which the PU is inactive, whereas a spatial opportunity is defined as the time interval in which the PU is active while the CU is located outside the PU protection range (PrR). In fact, to avoid harmful interference against the PU receiver, the CU must be able to detect the PU transmitter within a range, referred to as protection range (see Fig. 3.1), determined by the PU transmission range and CU interference range; therefore, when the CU is located outside the PrR it is allowed to use the spectrum even when the PU is active.

The main objective in spectrum sensing design is to select the sensing time that provides the maximum percentage of discovered spectrum opportunities without introducing an excessive overhead. In fact, there exists a trade-off between the percentage of discovered spectrum

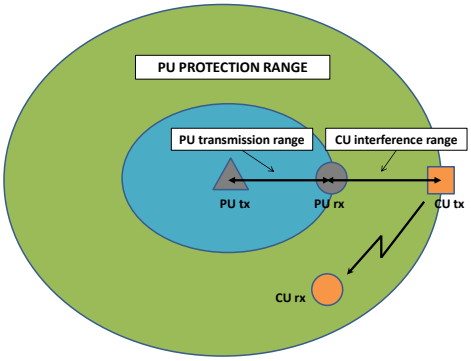

Figure 3.1: Protection range of the Primary User in cognitive radio networks.

opportunities, which increases with the sensing time, and the sensing efficiency, given by the ratio of the transmission time and the sensing period, which conversely decreases with the sensing time; the combination of these two factors determines the transmission capacity achieved by the CU that measures the efficiency in using opportunistically a given spectrum band. For this reason, a key issue in spectrum sensing design is the optimization of the sensing time that maximizes the transmission capacity achieved by the CU, while limiting the interference against the PU.

Traditionally, this issue has been addressed only with reference to the temporal spectrum sensing scenario [80], [85], where the CU is assumed inside the PrR of the PU, thus only the temporal opportunities can be considered, due to the temporal activity of the PUs. This assumption is reasonable for large-scale PU networks, as for example when the PU transmitter is the tower of a TV broadcasting system or the base-station of a cellular system. However, the aforementioned sensing issue becomes more challenging with reference to the spatio-temporal spectrum sensing scenario, recently considered in the literature [86], [87], [88]. In fact, in this scenario not only the temporal activity but also the spatial distribution of the PUs within a network region is taken into account, namely the PU network topology, whereby the CU can be also assumed outside the PrR of the active PU, as shown in Fig. 3.2. Thus, both the temporal and spatial dimension of the spectrum environment are jointly considered in the spatio-temporal sensing framework, that is more suitable and

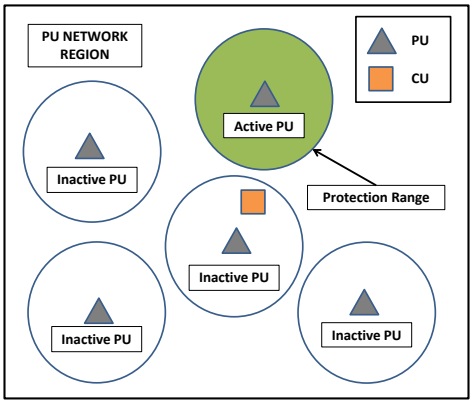

Figure 3.2: Spatio-temporal spectrum scenario in cognitive radio networks.

appealing for studying the scenario of a small-scale PU network, such as wireless microphone, emergency, military and sensors networks, which has recently gained attention in the literature [89], [90].

In the spatio-temporal spectrum scenario, also the spatial opportunities can be potentially exploited, thus the maximum transmission capacity that is possible to achieve is higher than that corresponding to the temporal spectrum scenario. However, due to the limited sensing accuracy, not only the temporal but also the spatial opportunities can be missed. In fact, when the CU is located outside the PrR, it can still detect the transmission of the PU[1], but without the knowledge of the PU position it will decide incorrectly for the absence of the spectrum opportunity. This sensing problem, referred to as spatial false-alarm problem [91], assumes considerable importance since it can have a great impact on the actual transmission capacity achieved by the CU. A viable solution is to increase the sensing time while satisfying a constraint on the detection probability when the CU is located inside the PrR, so that the communication of the PU is sufficiently protected from harmful interference. Contrary, the sensing efficiency decreases, thus it is very important to properly select the sensing time in the spatio-temporal spectrum scenario.

[1]It is because, given the strict PU detection constraint at the boundary of the protection range, the detection probability does not decrease efficiently as the distance between PU and CU increases.

3.1.1 Motivations and Contributions

The spatio-temporal spectrum sensing design problem has not been already investigated in the literature; in particular, the last recent works only assume that the PUs are in static positions. The aforementioned sensing issue becomes even more interesting but also challenging in the presence of PU mobility. In fact, the PU movement creates a spatial distribution where each point of the network region is visited at a specific rate, depending on the mobility pattern. This mobility effect can deeply influence the percentage of discovered spatial opportunities, and consequently also the transmission capacity achieved by the CU. Therefore, a key issue in spatio-temporal spectrum sensing design is the *optimization of the sensing time that maximizes the actual transmission capacity achieved by the CU with a limited sensing accuracy and in the presence of PU mobility, while satisfying the PU interference constraints.*

For this reason, in this work, we provide a theoretical analysis of the spatio-temporal spectrum sensing framework in the presence of PU mobility with the goal to address the aforementioned sensing issue, by completing and extending the preliminary results of [92].

More specifically, the contributions of this work can be summarized as follows. First of all, we extend the spatio-temporal spectrum sensing model to the mobile PU network scenario. Then, for the considered scenario, we introduce the mobility-aware sensing enabled capacity that is a new performance metric for CR networks that measures the actual transmission capacity achieved by the CU with a limited sensing accuracy. In particular, when the CU is located inside the PrR, we limit the interference against the PU, caused by the missed-detection sensing errors, with a constraint on the detection probability that is satisfied by selecting the proper value of the decision threshold. Moreover, we limit the further interference against the PU, due to the PU reappearance during the transmission stage, with a constraint on the interference probability that is satisfied by selecting a maximum transmission time, which depends on both traffic and mobility statistics of the PU. Then, by analyzing the framework for a generic PU mobility model, we theoretically prove the existence of a single optimal sensing time that maximizes the mobility-aware sensing enabled capacity. Finally, with reference to the well-known and widely adopted mobility models [93], [94], i.e., the Random Walk mobility Model (RWM) and the Random Way-Point mobility Model (RWPM), we carry-out the performance assessment to validate

the theoretical results. Moreover, through several experiments we provide interesting guidelines for spectrum sensing design that show how the optimal sensing time, which depend on the adopted mobility model, should be set in according to the radio environment conditions, such as the signal-to-noise-ratio, the protection range, the statistics of the PU temporal activity and the number of cooperative users.

The rest of the work is organized as follows. In Section 3.1.2, we discuss the related works. In Section 3.2, we present the spatio-temporal spectrum sensing model with the PU mobility, while in Section 3.3, we define the performance metrics. These metrics are analyzed in Section 3.4, where it is proved the existence of a single optimal sensing time that maximizes the mobility-aware sensing enabled capacity. The theoretical analysis is validated by simulations in Section 3.5, where several experiments are also provided. Finally, in Section 3.6, we draw the conclusions.

3.1.2 Related works

Recently, several works appeared in the literature that address several issues in the spatio-temporal spectrum scenario. In [86], the authors propose a joint spatial-temporal cooperative sensing scheme that exploits the information from the spatial sensing, i.e., both the position and the transmit power of the PU, to improve the accuracy of the temporal sensing. By accounting for the spectrum heterogeneity, in [88] the authors propose a two-dimensional sensing framework that exploits the correlations in time and space of the sensing results to improve the detection performance. However, these works assume that the PUs are in static positions. The effects of PU mobility on both the detection capability and maximum transmission capacity achieved by the CU are studied in [95], where in [96] the authors derived the optimal transmission time that maximizes the sensing efficiency, while satisfying the PU interference constraint, and a maximum sensing time threshold over which the sensing accuracy does not improve; however, these works do not take into account the spatial false-alarm problem, neither the effects of the PU mobility on the percentage of discovered spatial opportunities.

3.2 System Model

In this section, we first describe the PU and CR network models, the PU temporal activity model, and we give some definitions. Then, we present the spatio-temporal spectrum sensing model with the PU mobility features.

3.2.1 Network and Traffic Models

PU Network Model: For the sake of simplicity, we consider a network with a single PU transmitting on a given channel. Initially, the PU is placed randomly inside a square network region $\mathbf{A}$ of size $[0, a] \times [0, a]$, then it moves in according to a general mobility model. $f_{\boldsymbol{X}_{\mathrm{PU}}}(\boldsymbol{x}_{\mathrm{PU}})$ denotes the probability density function (pdf) of the PU steady-state spatial distribution, with $\boldsymbol{X}_{\mathrm{PU}}$ representing the random PU position.

CR Network Model: The CU is assumed static and randomly placed inside the network region $\mathbf{A}$. $f_{\boldsymbol{X}_{\mathrm{CU}}}(\boldsymbol{x}_{\mathrm{CU}})$ denotes the pdf of the CU spatial distribution, with $\boldsymbol{X}_{\mathrm{CU}}$ representing the random CU position.

PU Temporal Activity Model: The PU temporal activity is modeled as a two state (ON-OFF) Markov chain, where the processes of arrivals and departures are Poisson distributed with arrival rate λ_{off} and departure rate λ_{on}. In the ON state the PU is active, whereas in the OFF state the PU is inactive, and these two temporal events have the following probabilities:

$$P_{\mathrm{on}} = \frac{\lambda_{\mathrm{off}}}{\lambda_{\mathrm{on}} + \lambda_{\mathrm{off}}}, \quad P_{\mathrm{off}} = 1 - P_{\mathrm{on}} = \frac{\lambda_{\mathrm{on}}}{\lambda_{\mathrm{on}} + \lambda_{\mathrm{off}}}. \tag{3.1}$$

3.2.2 Definitions

Definition 3. *Inside spatial event.* The CU is located inside the PrR of the PU if the random distance $S \triangleq ||\boldsymbol{X}_{\mathrm{CU}} - \boldsymbol{X}_{\mathrm{PU}}||$ is not greater than the radius of the PrR, denoted as R, that is a known parameter. This spatial event, denoted as $\mathcal{I}$, has the following probability:

$$P(\mathcal{I}) = P(S \leq R) = \int_0^R f_S(s)\, ds \tag{3.2}$$

where $f_S(s)$ is the pdf of the random variable S, which depends on the adopted PU mobility model [95].

Definition 4. *Outside spatial event.* The CU is located outside the PrR of the PU if the distance S is greater than R. This spatial event, denoted as $\mathcal{O}$, has the following probability:

$$P(\mathcal{O}) = 1 - P(\mathcal{I}) = \int_{R}^{\sqrt{2}a} f_S(s)\, ds. \tag{3.3}$$

3.2.3 Spectrum Sensing Model

In the spatio-temporal spectrum scenario, the sensing problem is modeled as a composite hypothesis testing [87], [88], [91], which discriminate between the presence or the absence of a spectrum opportunity. In particular, by accounting also for the PU mobility statistics, we have the following spectrum sensing model:

$$\mathcal{H}_0 : \begin{cases} \mathcal{T}_0 : & y(n) = v(n) \\ \mathcal{S}_0 : & y(n) = \sqrt{P_r(s,g)}\, x(n) + v(n) \end{cases} \quad n = 1, 2, \ldots, N \tag{3.4}$$

$$\mathcal{H}_1 : y(n) = \sqrt{P_r(s,g)}\, x(n) + v(n) \quad n = 1, 2, \ldots, N \tag{3.5}$$

where $\mathcal{H}_0 = \mathcal{T}_0 \cup \mathcal{S}_0$ denotes the presence of a spectrum opportunity, i.e., a temporal opportunity when the PU is inactive ($\mathcal{T}_0$), which is independent on the PU position, or a spatial opportunity ($\mathcal{S}_0 = \mathcal{T}_1 \cap \mathcal{O}$) when the PU is active ($\mathcal{T}_1$) and the CU is located outside the PrR ($\mathcal{O}$), with $s \in (R, \sqrt{2}a]$ the distance from the PU. Instead, $\mathcal{H}_1 = \mathcal{T}_1 \cap \mathcal{I}$ denotes the absence of a spectrum opportunity, with $s \in (0, R]$.

We assume that the PU transmitted signal $x(n)$ is deterministic but not known, the noise $v(n) \sim \mathcal{CN}(0, \sigma_v^2)$ is a circularly symmetric complex Gaussian (CSCG) random process with power P_v, where $N = \lfloor T_s f_s \rfloor$ is the number of samples collected during the sensing time T_s, and f_s is the sampling frequency which depends on the channel bandwidth. The received power from the PU at a given distance $S = s$ and for a given channel power gain $G = g$, due to the combination of both multipath and shadow fading, is defined as:

$$P_r(s, g) = P_t \left(\frac{1}{s}\right)^{\rho} g \tag{3.6}$$

where P_t is the PU transmitted power measured at a reference distance, ρ is the path-loss exponent. Finally, the signal-to-noise ratio (SNR) is defined as $\gamma(s, g) = P_r(s, g)/P_v$. In the considered model we assume that

both the overall channel power gain, due to the fading effects, and the distance between PU and CU remain stationary during the sensing time T_s, namely we assume a *slow-mobility scenario* that can be reasonable for pedestrian or slow vehicular patterns [97].

Moreover, we assume an energy detector as a local sensing technique:

$$Y = \frac{1}{N}\sum_{n=1}^{N} |y(n)|^2 \underset{<\mathcal{H}_0}{\overset{\geq\mathcal{H}_1}{}} \epsilon \tag{3.7}$$

where ϵ is the decision threshold. According to the Central Limit Theorem (CLT), for large N, the sensing statistic Y can be approximated as a real Gaussian random variable under both the hypothesis $\mathcal{H}_0$ and $\mathcal{H}_1$. More specifically, in according to the previous assumptions, under the hypothesis $\mathcal{T}_0$, the mean value and the variance of the sensing statistic are given as follows:

$$E[Y|\mathcal{T}_0] = P_v, \quad \mathrm{Var}[Y|\mathcal{T}_0] = \frac{1}{N}P_v^2 \tag{3.8}$$

whereas, under the hypothesis $\mathcal{T}_1$ and conditioned on $S = s$ and $G = g$, we have:

$$\begin{aligned} E[Y|\mathcal{T}_1, S = s, G = g] &= (1 + \gamma(s, g))\, P_v \\ \mathrm{Var}[Y|\mathcal{T}_1, S = s, G = g] &= (1 + 2\gamma(s, g))\, \frac{P_v^2}{N} \end{aligned} \tag{3.9}$$

3.3 Performance Metrics

In this section, we define the performance metrics for the proposed spectrum sensing framework that will be mathematically analyzed in Section 3.4.

3.3.1 Missed Spectrum Opportunities

Due to the limited sensing accuracy, a percentage of both temporal and spatial opportunities can be missed. Thus, to measure the actual use of the licensed channel, we need to account for the sensing errors that cause the loss of spectrum opportunities. To this aim, we can define the following false-alarm probabilities:

Definition 5. *Temporal False-Alarm Probability*: the probability that the sensing statistic exceeds the decision threshold, conditioned on the event that the PU is inactive ($\mathcal{T}_0$). By accounting for (3.8), it is given as follows:

$$P_{f,t} = P(Y > \epsilon \,|\mathcal{T}_0) = Q\left(\left(\frac{\epsilon - P_v}{P_v}\right)\sqrt{T_s f_s}\right) \tag{3.10}$$

where $Q(\cdot)$ denotes the Q-function [98], whose expression is written as $Q(x) = (1/\sqrt{2\pi})\int_x^{+\infty} \exp(-\frac{u^2}{2})\, du$. This probability measures the percentage of missed temporal opportunities.

Definition 6. *Spatial False-Alarm Probability*: the joint probability that the sensing statistic exceeds the threshold and the CU is located outside the PrR ($\mathcal{O}$), conditioned on the event that the PU is active ($\mathcal{T}_1$). By accounting for (3.3), it is given as follows [91]:

$$P_{f,s} \triangleq P(Y > \epsilon, \mathcal{O} \,|\mathcal{T}_1) = \int_R^{\sqrt{2}a} P_d(s)\, f_S(s)\, ds \tag{3.11}$$

where $P_d(s) \triangleq P(Y > \epsilon \,|\mathcal{T}_1, S = s)$ is the detection probability at a given distance $S = s$, averaged over the random channel power gain G, that, by accounting for (3.9), is given as follows:

$$P_d(s) = \int_0^{+\infty} Q\left(\left(\frac{\epsilon}{P_v} - 1 - \gamma(s,g)\right)\sqrt{\frac{T_s f_s}{1 + 2\gamma(s,g)}}\right) f_G(g)\, dg \tag{3.12}$$

where $f_G(g)$ is the pdf of the overall channel power gain. The spatial false-alarm probability measures the percentage of missed spatial opportunities and, as it is possible to note in (3.11), it is influenced by the PU mobility through the pdf of the distance ($f_S(s)$).

3.3.2 Mobility-Aware Sensing Enabled Capacity

In the spatio-temporal spectrum scenario, the CU can opportunistically access to a licensed channel when the PU is inactive or when the PU is active and the CU is outside the PrR. Thus, we can define the following probabilities:

Definition 7. *Channel Access Probability*: the probability that the channel is available for the opportunistic access. By accounting for (3.1) and (3.3), it is given as follows:

$$\mathrm{CAP} = P_{\mathrm{off}} + P_{\mathrm{on}} P(\mathcal{O}) \tag{3.13}$$

This probability measures the maximum percentage of temporal and spatial opportunities that is possible to exploit.

Definition 8. *Channel Access Probability enabled by sensing*: the probability that the channel is correctly sensed available and used for the opportunistic access. By accounting for (3.10) and (3.11), it is given as follows:

$$\begin{aligned} \mathrm{CAP}_{\mathrm{sens}} &= \left(1 - P(Y > \epsilon \,|\mathcal{T}_0)\right) P_{\mathrm{off}} + \left(1 - P(Y > \epsilon \,|\mathcal{T}_1, \mathcal{O})\right) P(\mathcal{O}) P_{\mathrm{on}} \\ &= \left(1 - P_{f,t}\right) P_{\mathrm{off}} + \left(P(\mathcal{O}) - P_{f,s}\right) P_{\mathrm{on}} \end{aligned} \tag{3.14}$$

This probability measures the actual percentage of discovered temporal and spatial opportunities enabled by sensing, i.e., by taking into account the impact of sensing accuracy[2]. Due to the sensing errors, it is lower than CAP but can be improved by increasing the sensing time, as we will show in Section 3.4.

Finally, to measure the actual use of the licensed channel, we need also to take into account the sensing efficiency (η), given by the ratio of the transmission time (T_x) and the sensing period ($T_s + T_x$), that contrary decreases with the sensing time. To this aim, we define the following performance metric:

Definition 9. *Mobility-Aware Sensing Enabled Capacity*: the product of the sensing efficiency and the channel access probability enabled by sensing. By accounting for the expression of η and (3.14), it is given as follows:

$$\mathrm{MSC} = \eta \, \mathrm{CAP}_{\mathrm{sens}} = \frac{T_x}{T_s + T_x} \left(\left(1 - P_{f,t}\right) P_{\mathrm{off}} + \left(P(\mathcal{O}) - P_{f,s}\right) P_{\mathrm{on}} \right). \tag{3.15}$$

This performance metric measures the actual transmission capacity that is achieved by CU with a limited sensing accuracy and in the presence of PU mobility.

[2]We don't assume to know the PU position in which case the missed spatial opportunities should not be considered. Instead, our objective is to select the sensing time that maximizes the percentage of discovered temporal and spatial opportunities without introducing an excessive overhead.

3.3.3 PU interference constraints

In the spatio-temporal spectrum scenario, interference against the PU can occur during the transmission stage only when the CU is inside the PrR, thus the average interference is lower than that corresponding to the temporal spectrum scenario. More specifically, a first occurrence is when the CU does not detect the active PU during the sensing stage and, consequently, starts to transmit by interfering with the PU. In this instance, the maximum level of interference can be limited by introducing a constraint on the detection probability in the worst case, namely when the CU is at the boundary of the PrR, at the distance R from the PU, where the detection probability is minimum [80], [91]. This constraint is satisfied by selecting the decision threshold ϵ as follows:

$$\begin{aligned} \text{Find}: \quad & \epsilon \\ \text{Subject to}: \quad & P_d(R, T_s, \epsilon) \leq \alpha \end{aligned} \tag{3.16}$$

where P_d is given in (3.12), whereas α is the detection constraint. This problem has a unique solution since the detection probability is a monotonic decreasing function with ϵ [76], thus $P_d(\epsilon)$ is invertible and the decision threshold satisfying (3.16) can be calculated.

Moreover, even though the PU is inactive and the sensing decision is correct, interference can still occur during the transmission stage since the PU can became active again. In this instance, it is possible to limit the level of interference by introducing a constraint on the interference probability that is satisfied by selecting a maximum transmission time [99]. To this aim, we can define the interference probability as follows[3]:

$$\begin{aligned} P_{\text{int}} &= (1 - P_{f,t}(T_s))\, P\left(T_{\text{off}} < T_x\right) P_{\text{off}}\, P(\mathcal{I}) \\ &= (1 - P_{f,t}(T_s))\left(1 - \exp(-\lambda_{\text{off}} T_x)\right) P_{\text{off}}\, P(\mathcal{I}) \\ &\leq \left(1 - \exp(-\lambda_{\text{off}} T_x)\right) P_{\text{off}}\, P(\mathcal{I}) \end{aligned} \tag{3.17}$$

where $T_{\text{off}} \sim \text{Exp}(\lambda_{\text{off}})$ is the random variable that models the duration of the OFF state that is exponentially distributed, since the process of arrival is Poisson distributed[4] [98]. The upper bound in (3.17) represents

[3] We assume that, during the transmission time, the CU remains inside or outside the protection range, i.e., the PU movements are sufficiently slow.

[4] We remember that, due to the memoryless property of the Poisson distribution, the residual time from the most recent instant in which the channel is sensed to that before the PU becomes active again, is statistically equivalent to T_{off}.

the maximum interference probability without the impact of sensing accuracy, that becomes very tight when the sensing time is sufficiently large. In the following, we use this expression that allows us to make the analysis (Section 3.4) mathematically tractable. In particular, as it is possible to note, the interference probability increases with the transmission time T_x, and reaches its maximum value $P_{\text{off}}\,P(\mathcal{I})$ when T_x is sufficiently large. More specifically, T_x has to solve the following problem:

$$\begin{aligned} \text{Find}: \quad & T_x \\ \text{Subject to}: \quad & P_{\text{int}} \leq \beta \end{aligned} \tag{3.18}$$

where β is the interference probability constraint. By using (3.17) and after simple mathematical manipulations, the maximum transmission time that satisfies (3.18) has the following expression:

$$T_x^{\max} = \frac{1}{\lambda_{\text{off}}} \ln\left(\frac{P_{\text{off}}\,P(\mathcal{I})}{P_{\text{off}}\,P(\mathcal{I}) - \beta}\right) \tag{3.19}$$

that is valid when $\beta < P_{\text{off}}\,P(\mathcal{I})$, otherwise the interference constraint is always satisfied independently on the value of T_x. As it is possible to note, the maximum transmission time depends on both the PU traffic and mobility statistics; in particular, it increases when P_{off} or $P(\mathcal{I})$ decreases since the interference probability also decreases.

3.4 Theoretical Performance Analysis

In this section, we first formulate the optimization problem that consist in finding the sensing time value that maximizes the mobility-aware sensing enabled capacity, while satisfying the PU interference constraints (subsection 3.3.3). Then, we theoretically prove the existence of a single optimal sensing time. Finally, the theoretical results are discussed at the end of the section.

3.4.1 Sensing Time Optimization Problem

To prove the existence of a single optimal sensing time, we formulate the following optimization problem:

$$\begin{aligned} \text{Find}: &\quad T_s \\ \text{Maximizing}: &\quad \text{MSC}(T_s) \\ \text{Subject to}: &\quad P_d(R, T_s, \epsilon) \leq \alpha,\ P_{\text{int}} \leq \beta \end{aligned} \tag{3.20}$$

where $\text{MSC}(T_s)$ is given in (3.15) and the interference constraints are given in subsection 3.3.3. To prove the existence of a single solution, we have to analyze the expression of $\text{MSC}(T_s)$ obtained from (3.15) by introducing the interference constraints, in particular we have to analyze the temporal and spatial false-alarm probability with the sensing time. In order to make the analysis mathematically tractable, we give the proof in the AWGN channel hypothesis, i.e., by removing the effects of multipath and shadow fading. In Section 3.5, we will extend the analysis through simulations by considering also their effects.

3.4.2 Analysis of $P_{f,t}$ with the sensing time

To analyze the temporal false-alarm probability with the sensing time, first we have to single-out the expression of the decision threshold satisfying (3.16). To this aim, by accounting for (3.12), we have to solve the following equation:

$$P_d(R, T_s) = Q\left(\left(\frac{\epsilon}{P_v} - 1 - \gamma(s)\right)\sqrt{\frac{T_s f_s}{1 + 2\gamma(s)}}\right) = \alpha. \tag{3.21}$$

By using the Q-function inverse, after simple mathematical manipulations, we have:

$$\epsilon = \left(Q^{-1}(\alpha)\sqrt{\frac{1 + 2\gamma(R)}{T_s\, f_s}} + 1 + \gamma(R)\right) P_v \tag{3.22}$$

and, by substituting (3.22) in (3.10), finally we have:

$$P_{f,t}(T_s) = Q\left(Q^{-1}(\alpha)\sqrt{1 + 2\gamma(R)} + \gamma(R)\sqrt{T_s\, f_s}\right) \tag{3.23}$$

The temporal false-alarm probability decreases with the sensing time T_s, since $Q(.)$ is a monotonic decreasing function. Moreover, we have the following result:

Proposition 5. The temporal false-alarm probability $P_{f,t}$ is a convex function with T_s if the following condition (a) otherwise (b) is satisfied:

$$(a): \quad |Q^{-1}(\alpha)|^2 (1 + 2\gamma(R)) - 4 < 0; \tag{3.24}$$

$$(b): \quad (T_s < t_1^2) \cup (T_s > t_2^2) \tag{3.25}$$

where t_1 and t_2 are given in (I.4).

Proof. See Appendix I. □

Remark 16. If the condition (a) is satisfied, then $P_{f,t}$ is a convex function, independently from T_s. For example, in low SNR scenarios, i.e., $\gamma(R) << 1$, the condition (a) is satisfied when $\alpha < Q(-2) = 0.97$. Otherwise, the sensing time has to satisfy the condition (b). In particular, as also proved in [80], this condition is satisfied when T_s is sufficiently large such that $P_{f,t}(T_s) < 0.5$, that is reasonable in conditions of practical interest.

3.4.3 Analysis of $P_{f,s}$ with the sensing time

By substituting (3.22) in (3.12), after simple mathematical manipulations, we have the following expression of the detection probability:

$$P_d(s, T_s) = Q\left(Q^{-1}(\alpha) \sqrt{\frac{1 + 2\gamma(R)}{1 + 2\gamma(s)}} + (\gamma(R) - \gamma(s)) \sqrt{\frac{T_s\, f_s}{1 + 2\gamma(s)}} \right) \tag{3.26}$$

As it is possible to note, when $s < R$, i.e., the CU is located inside the PrR, the detection probability increases with the sensing time T_s, since $\gamma(s) > \gamma(R)$, and it converges to one; when $s = R$, i.e., the CU is located at the boundary of the PrR, the detection probability is equal to α; furthermore, when $s > R$, i.e., the CU is located outside the PrR, the detection probability decreases with the sensing time, since $\gamma(s) < \gamma(R)$, and it converges to zero. This behavior is a consequence of the imposed constraint on the detection probability at the boundary of the PrR. This behavior is desired since by increasing the sensing time, from one side, we want to reduce the interference against the PU inside the PrR and, from the other side, we want to increase the percentage of discovered spatial opportunities and so the performance of the CR network. In particular, when s is sufficiently large such that $\gamma(s) \simeq 0$, the detection probability converges to the temporal false-alarm probability in (3.23).

From the above discussion, we can state that the spatial false-alarm probability $P_{f,s}(T_s)$, given in (3.11), is a decreasing function with the sensing time. Moreover, we have the following result:

Proposition 6. The spatial false-alarm probability $P_{f,s}$ is a convex function with T_s if the following condition (c) otherwise (d) is satisfied:

$$(c): \quad |Q^{-1}(\alpha)|^2 (1 + 2\gamma(R)) - 4(1 + 2\gamma(s)) < 0; \tag{3.27}$$

$$(d): \quad (T_s < t_3^2) \cup (T_s > t_4^2) \tag{3.28}$$

where t_3 and t_4 are given in (J.4).

Proof. See Appendix J. □

Remark 17. The considerations of Remark 16 can also be extended to $P_{f,s}$. In particular, when s tends to R, the condition (d) is certainly satisfied, since t_3 tends to infinite, whereas, when s is sufficiently large such that $\gamma(s) << \gamma(R)$, the conditions (c) and (d) become equal to (a) and (b) in Proposition 5, respectively.

3.4.4 Analysis of MSC with the sensing time

In the following, we prove in Theorem 8 the existence of a single optimal sensing time that solves the problem (3.20), namely that maximizes $\mathrm{MSC}(T_s)$. The proof requires first the following result:

Proposition 7. The channel access probability enabled by sensing is an increasing and concave function with T_s.

Proof. From (3.14) it follows that:

$$\frac{d\,\mathrm{CAP}_{\mathrm{sens}}(T_s)}{dT_s} = -\frac{d\,P_{f,t}(T_s)}{dT_s} P_{\mathrm{off}} - \frac{d\,P_{f,s}(T_s)}{dT_s} P_{\mathrm{on}}. \tag{3.29}$$

Since the temporal and spatial false-alarm probabilities decrease with T_s, then the channel access probability increases with T_s, namely (3.29) is positive. In particular, by exploiting the Propositions 5 and 6, we have that (3.29) is decreasing with T_s. □

Theorem 8. It exists a single optimal sensing time T_s that maximizes the mobility-aware sensing enabled capacity, while satisfying the PU interference constraints.

Proof. From (3.15), we have that:

$$\frac{d\,\mathrm{MSC}(T_s)}{dT_s} = -\frac{T_x}{(T_s+T_x)^2}\,\mathrm{CAP}_{\mathrm{sens}}(T_s) + \frac{T_x}{T_s+T_x}\,\frac{d\,\mathrm{CAP}_{\mathrm{sens}}(T_s)}{dT_s} \tag{3.30}$$

where the first term at the right side of the equality (3.30) is negative and the second term is positive. In particular, when T_s tends to zero, the first term is finite (see (3.14), (3.23) and (3.26)) but the second term tends to infinite (see (3.29), (I.1) in Appendix I and (J.1) in Appendix J), thus (3.30) is positive. On the other hand, when T_s tends to infinite, the second term tends exponentially to zero, that can be neglected compared to the first term when T_s is sufficiently large, thus (3.30) is negative. This means that $\mathrm{MSC}(T_s)$ has at least one maximum, and from (3.30) we have:

$$\frac{d\,\mathrm{MSC}(T_s)}{dT_s} = 0 \quad \Leftrightarrow \quad \frac{d\,\mathrm{CAP}_{\mathrm{sens}}(T_s)}{dT_s} = \frac{\mathrm{CAP}_{\mathrm{sens}}(T_s)}{T_s+T_x} \tag{3.31}$$

Moreover, by deriving (3.30), after simple mathematical manipulations, we have:

$$\begin{aligned}\frac{d^2\,\mathrm{MSC}(T_s)}{dT_s^2} = {} & \frac{2T_x}{(T_s+T_x)^3}\,\mathrm{CAP}_{\mathrm{sens}}(T_s) - \frac{2T_x}{(T_s+T_x)^2}\,\frac{d\,\mathrm{CAP}_{\mathrm{sens}}(T_s)}{dT_s} \\ & + \frac{T_x}{(T_s+T_x)}\,\frac{d^2\,\mathrm{CAP}_{\mathrm{sens}}(T_s)}{dT_s^2}\end{aligned} \tag{3.32}$$

and, by replacing (3.31) in (3.32), we have:

$$\frac{d^2\,\mathrm{MSC}(T_s)}{dT_s^2} = \frac{T_x}{(T_s+T_x)}\,\frac{d^2\,\mathrm{CAP}_{\mathrm{sens}}(T_s)}{dT_s^2} \tag{3.33}$$

Since $\mathrm{CAP}_{\mathrm{sens}}(T_s)$ is a concave function with T_s (Proposition 7), then (3.32) is negative when (3.30) is zero, thus $\mathrm{MSC}(T_s)$ has a single maximum. □

3.5 Performance Assessment

In this section, we carry out the performance assessment of the proposed framework when two widely adopted mobility models are considered [93], [94], i.e., the Random Walk mobility Model (RWM) and the Random Way-Point mobility Model (RWPM). To this aim, first of

all, we validate the theoretical results derived in Section 3.4 through Monte Carlo simulations for the AWGN scenario, then the effects of both multipath and shadow fading are considered; in particular, for the multipath fading we use the exponential distribution (that comes from the Rayleigh fading assumption), whereas for the shadow fading we use the log-normal distribution [100].

More specifically, to simulate the PU mobility, we first generate 10^4 topologies by placing both the PU and CU randomly in a squared network region. Then, for each topology, we let the PU moves according to the adopted mobility model (RWM or RWPM) for enough time to reach the steady-state distribution[5]. Then, the probability that the PU visits each position and the probability that the PU is inside the protection range, are estimated. Furthermore, to simulate the effects of both multipath and shadow fading, we generate 10^4 realizations of the channel power gains according to their statistical distributions. In the following, we provide several experiments that validate the theoretical analysis; interesting guidelines for spectrum sensing design are also provided.

Experiment 1. In this experiment, we assume the AWGN channel model and validate the theoretical results when the RWM and RWPM are adopted. In particular, we use the following set of parameters: the protection range is $R = 0.4\,a$, the PU inactivity probability is $P_{\text{off}} = 0.6$, the detection constraint is $\alpha = 0.9$, the interference probability constraint is $\beta = 10^{-2}$, the PU arrival rate is $\lambda_{\text{off}} = 0.5$, the sampling frequency is $f_s = 10^6$, the path-loss exponent is $\rho = 4$.

In Fig. 3.3, left-side plot, it is shown the Detection Probability ($P_d(s, T_s)$), given in (3.26), versus the distance between PU and CU normalized to the network side (s/a), when the CU is located outside the PrR ($s > R$), and for different values of the sensing time (T_s). It is shown that, the $P_d(s, T_s)$ decreases with T_s, while satisfying the detection constraint (α)[6]. In particular, the $P_d(s, T_s)$ decreases when the SNR at the boundary of the protection range ($\gamma(R)$) increases. Furthermore, the $P_d(s, T_s)$ decreases with the distance and converges to the Temporal

[5]We remember that, the spatial distribution of the considered mobility models is independent from the speed of the mobile node, but it only depends on the network region.

[6]Conversely, it can be shown that the detection probability increases with the sensing time when the CU is located inside the PrR, namely when the distance is lower than the protection radius.

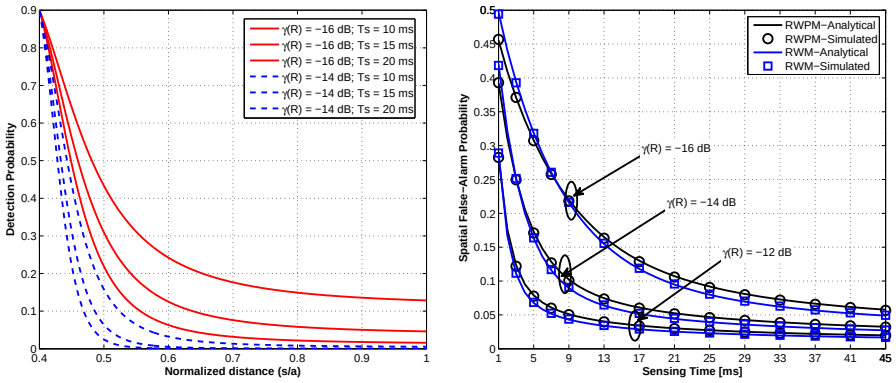

Figure 3.3: Experiment 1: On the left-side plot, it is shown the Detection Probability ($P_d(s, T_s)$) versus the distance between PU and CU normalized to the network side (s/a), when the CU is located outside the PrR ($s > R$), and for different values of T_s. On the right-side plot, it is shown the Spatial False-Alarm Probability ($P_{f,s}(T_s)$) versus T_s, for both the mobility models (RWM, RWPM), in the AWGN scenario.

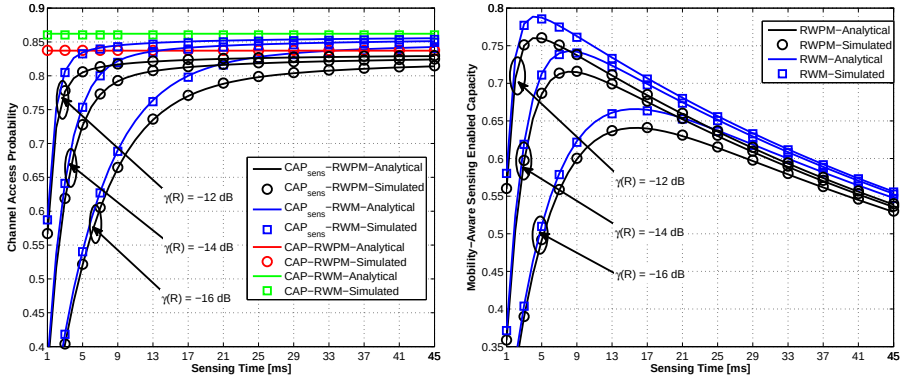

Figure 3.4: Experiment 1: On the left-side plot, it is shown the Channel Access Probability (CAP) and the Channel Access Probability enabled by sensing ($\mathrm{CAP}_{\mathrm{sens}}(T_s)$) versus T_s, whereas, on the right-side plot, it is shown the Mobility-Aware Sensing Enabled Capacity ($\mathrm{MSC}(T_s)$) versus T_s, for both the mobility models (RWM, RWPM), in the AWGN scenario.

False-Alarm Probability ($P_{f,t}(T_s)$), given in (3.23), that, for the sake of simplicity, it is not plotted here.

In Fig. 3.3, right-side plot, it is shown the Spatial False-Alarm Probability ($P_{f,s}(T_s)$), given in (3.11), versus T_s, for both the adopted mo-

bility models. First of all, we observe that, the analytical expressions given in (3.11), where the pdf of the distance ($f_S(s)$) has been derived in [95] for both the RWM and RWPM, match well the simulated results. Then, we observe that, the $P_{f,s}(T_s)$ decreases with T_s and it is a convex function, since, as proved in Proposition 6, the condition (c) is verified[7]. The same results can be shown for the temporal false-alarm probability ($P_{f,t}(T_s)$), given in (3.23), as proved in the Proposition 5. Furthermore, we observe that, the $P_{f,s}(T_s)$ decreases with $\gamma(R)$, and depends on the adopted mobility model.

In Fig. 3.4, left-side plot, it is shown the Channel Access Probability (CAP), given in (3.13), and the Channel Access Probability enabled by sensing ($\text{CAP}_{\text{sens}}(T_s)$), given in (3.14), versus T_s, for both the adopted mobility models. First of all, we observe that, the $\text{CAP}_{\text{sens}}(T_s)$ is lower than CAP, due to the missed temporal and spatial opportunities. However, the $\text{CAP}_{\text{sens}}(T_s)$ increases with T_s, since both the $P_{f,t}(T_s)$ and $P_{f,s}(T_s)$ decreases, and approaches to the CAP when T_s is sufficiently large. Moreover, the $\text{CAP}_{\text{sens}}(T_s)$ increases with $\gamma(R)$. In particular, the $\text{CAP}_{\text{sens}}(T_s)$ is a concave function, as proved in the Proposition 7. Furthermore, by accounting for the PU mobility effect, we observe that, in the RWM case, both the CAP and $\text{CAP}_{\text{sens}}(T_s)$ are higher than the RWPM case. This is because, in the RWM case, the probability that the CU is located outside the protection range ($P(\mathcal{O})$) is higher than the RWPM case, as well as the percentage of spatial opportunities.

Finally, in Fig. 3.4, right-side plot, it is shown the Mobility-Aware Sensing Enabled Capacity ($\text{MSC}(T_s)$), given in (3.15), versus T_s, for both the adopted mobility models. We observe that, by increasing T_s, the $\text{MSC}(T_s)$ at the beginning increases, since the increasing of the $\text{CAP}_{\text{sens}}(T_s)$ overcome the decreasing of the sensing efficiency ($\eta(T_s)$); however, after a certain value, the $\text{MSC}(T_s)$ starts to decrease since the $\text{CAP}_{\text{sens}}(T_s)$ slowly approaches to its maximum value (CAP) and the decreasing of $\eta(T_s)$ is predominant. Thus, this trade-off implies the existence of a single optimal sensing time that maximizes the $\text{MSC}(T_s)$, as proved in the Theorem 8. In particular, when $\gamma(R)$ increases, the $\text{MSC}(T_s)$ also increases and varies more rapidly with T_s, whereas the optimal sensing time decreases. Furthermore, we observe that, in the RWM case, the $\text{MSC}(T_s)$ is higher than the RWPM case. In fact, in the

[7]It is possible to show that, in the cases where the condition (c) is not verified, the condition (d) holds when the sensing time is sufficiently large.

RWM case, not only the $\mathrm{CAP}_{\mathrm{sens}}(T_s)$ but also $\eta(T_s)$ is greater than the RWPM case, since the maximum transmission time ($T_x^{\max}$) satisfying the PU interference constraint (β), given in (3.19), is higher than the RWPM case. This is because, as stated before, in the RWM case the probability that the CU is located inside the protection range ($P(\mathcal{I})$) is lower than the RWPM case. Specifically, for the considered parameters, we have that: $T_x^{\max} = 99\,\mathrm{ms}$ in the RWM case, $T_x^{\max} = 84\,\mathrm{ms}$ in the RWPM case. Finally, in the AWGN scenario, we observe that the optimal sensing time is almost the same for both the mobility models.

Experiment 2. In this example, first of all, we prove the existence of the single optimal sensing time that maximizes the mobility-aware sensing enabled capacity in a more realistic channel propagation scenario, i.e., when both the effects of multipath and shadow fading are taken into account. Then, we provide several experiments that highlight how the optimal sensing time, which depend on the adopted mobility model, should be set according to the radio environment conditions, such as the SNR, the protection range, the PU temporal activity statistics; the trend of the maximum transmission capacity achieved by the CU is also shown.

We use the following set of parameters: the detection constraint is $\alpha = 0.9$, the interference probability constraint is $\beta = 10^{-2}$, the PU arrival rate is $\lambda_{\mathrm{off}} = 0.5$, the sampling frequency is $f_s = 10^6$, the path-loss exponent is $\rho = 4$, the standard deviation of the shadowing is $\sigma_{dB} = 5$. In particular, the decision threshold in (3.16), that satisfies the detection constraint, is calculated numerically.

In Fig. 3.5, left-side plot, it is shown the MSC versus T_s, for both the adopted mobility models. The results confirm the existence of a single optimal sensing time that maximizes the MSC, while satisfying the PU interference constraints. In particular, the optimal sensing time decreases with $\gamma(R)$, and, contrarily to the AWGN scenario, it is different for the two mobility models. Moreover, as well known, we observe that, the presence of fading causes a severe performance degradation compared to the AWGN channel scenario.

In Fig. 3.5, right-side plot, it is plotted the optimal sensing time (T_s^{opt}) versus $\gamma(R)$, for both the adopted mobility models. We observe that, the T_s^{opt} decreases with $\gamma(R)$, and, in the RWM case, it is greater than the RWPM case. In particular, the T_s^{opt} is higher when the protec-

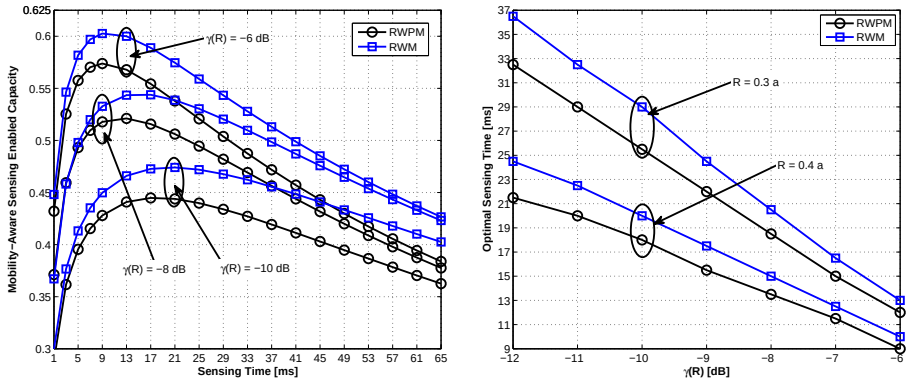

Figure 3.5: Experiment 2: On the left-side plot, it is shown the Mobility-Aware Sensing Enabled Capacity ($\mathrm{MSC}(T_s)$) versus T_s, whereas, on the right-side plot, it is shown the optimal sensing time (T_s^{opt}) versus the SNR at the distance R ($\gamma(R)$), for both the mobility models (RWM, RWPM), in the Fading scenario.

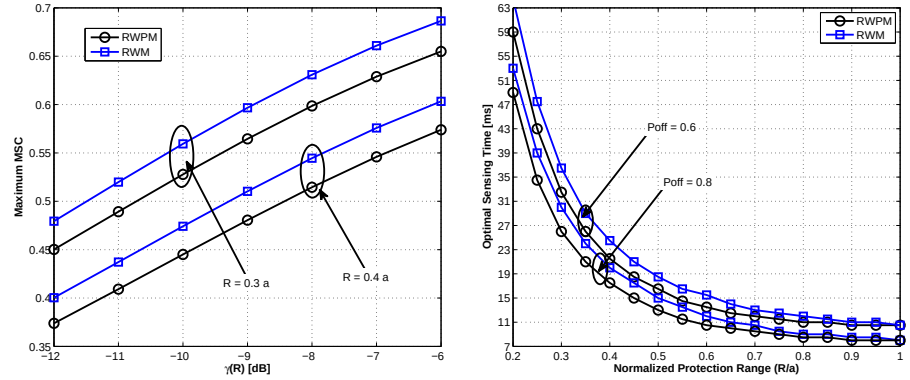

Figure 3.6: Experiment 2: On the left-side plot, it is shown the maximum value of $\mathrm{MSC}(T_s)$ versus the SNR at the distance R ($\gamma(R)$), whereas, on the right-side plot, it is shown the optimal sensing time (T_s^{opt}) versus the protection range normalized to the network side (R/a), for both the mobility models (RWM, RWPM), in the Fading scenario.

tion radius R is lower, due to the following two reasons: (i) more spatial opportunities are available and can be discovered, thus the $\mathrm{CAP}_{\mathrm{sens}}(T_s)$ is higher; (ii) the maximum transmission time ($T_x^{\max}$), given in (3.19), is greater since $P(\mathcal{I})$ is lower, thus the sensing efficiency is higher. In particular, when $R = 0.3\,a$, we have that: $T_x^{\max} = 161\,\mathrm{ms}$ in the RWM

case, $T_x^{\max} = 138\,\text{ms}$ in the RWPM case. Furthermore, the maximum MSC ($\text{MSC}_{\max}$), that is shown in Fig. 3.6, left-side plot, increases with $\gamma(R)$, and also increases when R decreases. In particular, in the RWM case, it is greater than the RWPM case, for the same reasons explained in the Experiment 1.

In Fig. 3.6, right-side plot, it is shown the T_s^{opt} versus R/a, for both the adopted mobility models. We observe that, the T_s^{opt} decreases with R for the same reasons expressed before, where the difference between the RWM and RWPM model vanishes when R is very large, since $P(\mathcal{I})$ converges to one for both the mobility models. In particular, the T_s^{opt} is lower when P_{off} is higher, since the maximum transmission time $T_x^{\max}$ is lower, as shown in Fig. 3.7, left-side-plot, and so the decreasing rate of the sensing efficiency is higher and prevails over the increasing rate of CAP_{sens}. Furthermore, the maximum MSC ($\text{MSC}_{\max}$), that is shown in Fig. 3.7, right-side plot, decreases with R, and also the difference between the RWM and RWPM model vanishes when R is very large, for the same reason expressed before. However, it increases when P_{off} is higher, since more temporal opportunities are available and can be discovered.

Experiment 3. As expressed throughout the thesis, an effective way to counteract the fading effect and improve the sensing accuracy is to exploit the spatial diversity through the cooperation of spatially distributed CUs [19]. Here, we design a simple scenario to show how the cooperative sensing performance behaves in the presence of PU mobility. More specifically, we consider a set of M cooperative users that send their local sensing decisions to a common CU, that acts as a decision maker, through ideals reporting channels. The decision maker combines these sensing decisions by using the OR fusion-rule, that gives better performance than other decision rules in many cases of practical interest [101], [102], and finally takes the decision about the presence/absence of a spectrum opportunity. For the sake of simplicity, we assume that the cooperative users are approximatively at the same distance from the PU, and experience uncorrelated shadowing effects. The set of parameters is the same used in the previous example.

In Fig. 3.8, left-side plot, it is shown T_s^{opt} versus the number of cooperative users (M), for both the adopted mobility models. We observe that, the T_s^{opt} decreases with M and the difference between the

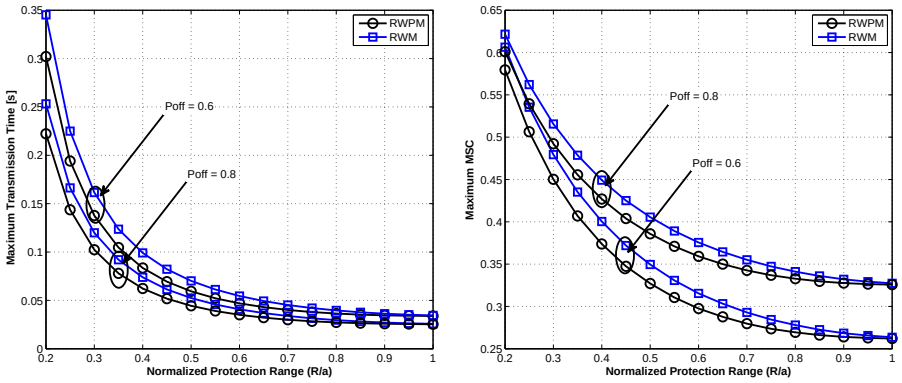

Figure 3.7: Experiment 2: On the left-side plot, it is shown the maximum Transmission time ($T_x^{\max}$), whereas, on the right-side plot, it is shown the maximum value of MSC, versus the protection range normalized to the network side (R/a), for both the mobility models (RWM, RWPM), in the Fading scenario.

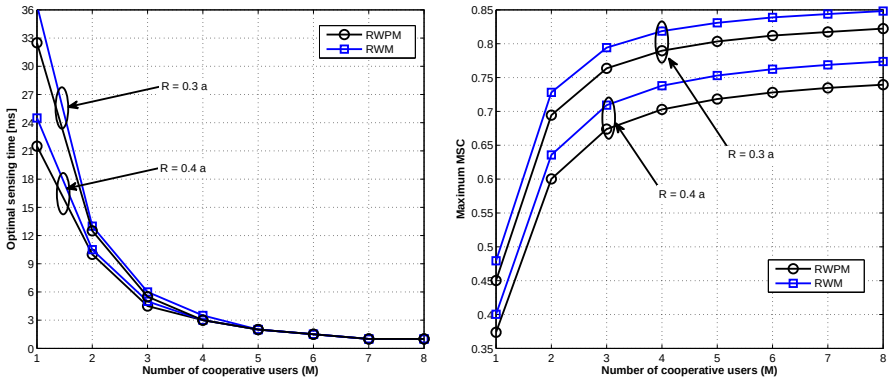

Figure 3.8: Experiment 3: On the left-side plot, it is shown the optimal sensing time T_s^{opt}, whereas, on the right-side plot, it is shown the maximum value of MSC, versus the number of cooperative users (M), for both the mobility models (RWM, RWPM), in the Fading scenario. It is considered the OR-fusion rule for taking the cooperative decision.

RWM and RWPM vanishes when M is sufficiently large. Furthermore, the T_s^{opt} increases when R is lower, for the same reasons expressed before. Instead, as shown in Fig. 3.8, right-side plot, the maximum MSC ($\text{MSC}_{\max}$) increases with M and approaches to its maximum value when M is sufficiently large, since the $\text{CAP}_{\text{sens}}(T_s)$ approaches to its maximum

value. In particular, the $\text{MSC}_{\max}$, in the RWM case, is higher than the RWPM case, for the same reasons expressed before. Finally, it is higher when the protection radius R is lower.

3.6 Conclusions

In this chapter, the spatio-temporal spectrum sensing design problem in the presence of Primary-User (PU) mobility has been addressed. More specifically, a new performance metric, named *mobility-aware sensing enabled capacity* has been introduced, that measures the actual transmission capacity achieved by the Cognitive User (CU) with a limited sensing accuracy, namely by taking into account both the missed temporal and spatial opportunities. Then, a theoretical analysis has been developed to prove the existence of a single optimal sensing time that maximizes the mobility-aware sensing enabled capacity, while satisfying the PU interference constraints. The theoretical results have been validated by simulations when two widely adopted mobility models are considered, i.e., the Random Walk mobility Model (RWM) and the Random Way-Point mobility model (RWPM). Then, several experiments, that constitute the guidelines for spectrum sensing design, have been provided that show how the optimal sensing time, which depend on the adopted mobility model, should be set in according to the radio environment conditions. In particular, it has been shown that the optimal sensing time is higher in the RWM case, but the corresponding maximum transmission capacity is even more higher, since the mobility pattern influences differently the percentage of discovered spatial opportunities that is higher in the RWM case. The future developments concern the analysis of the proposed framework in the presence of multiple mobile PUs transmitting on a given channel, and by proposing effective cooperative sensing decision approaches.

Conclusions

In this thesis, the role of the *cooperative paradigm* in wireless networks has been studied with the aim to demonstrate that it is an effective way to counteract the impairments of wireless channels caused by the fading effects, through the exploitation of the *spatial diversity*, and so to guarantee satisfactory performance that otherwise would not be achievable through an individual action. More specifically, the advantages of the cooperative paradigm has been shown with reference to both traditional relay networks, for *cooperative transmission*, and cognitive radio networks, for cooperative spectrum sensing, and three different problems on these research topics have been presented.

With reference to Cooperative Relay Networks, we studied the performance of distributed Space-Time Block Coding (STBC) schemes involving multiple decode-and-forward (D&F) relays in the presence of impulsive noise, modeled in according to the Middleton Class-A (MCA) distribution, by considering both optimal (ML, IML) and suboptimal (MD) detecting structures at the destination, and both centralized and decentralized cooperative strategies. We proved analytically that, with respect to Gaussian noise, the major effect of the impulse noise on the performance of the IML and MD detectors concerns the finite signal-to-noise ratio (SNR) diversity order, which does not monotonously increase as the SNR rises, but instead oscillates between a maximum and a minimum before to reach its asymptotic (i.e., in the high SNR region) value. The same behavior is shown for both centralized and decentralized schemes, and also when the number of active relays is random. In particular, independently from the detecting structure employed at the destination, decentralized scheme pays a performance degradation with respect to its centralized counterpart, that becomes slight by increasing the number of relays. Moreover, we showed that in the case of complex orthogonal STBC, this oscillating behavior tends to completely disap-

pear in the case of the IML detector for sufficiently large values of the asymptotic diversity order; contrary, the performances of the MD detector, both in terms of finite-SNR diversity order and coding gain, become worsen.

With reference to Cognitive Radio (CR) Networks, we focus the attention on the two objectives of spectrum sensing functionality: (i) to guarantee an high detection accuracy for avoiding harmful interference against Primary-User (PU) networks, (ii) to efficiently identify and exploit the spectrum holes for enhancing the transmission capacity of CR networks.

Regarding the first spectrum sensing objective, we studied the performance of different cooperative spectrum sensing techniques for two different decision approaches, namely the Combining Decision (CD) approach, where the decision maker does not participate in sensing, and the Sensing & Combining Decision (SCD) approach, where the decision maker participates in sensing and uses its sensing statistics in place of one another Cognitive User (CU). In particular, by accounting for the multipath fading effects of both sensing and reporting channels, we first design the proposed cooperative sensing techniques in according to both the decision approaches, then we proved that the detection accuracy exhibits a threshold behavior as a function of the adopted decision approach, independently on the considered cooperative sensing technique, namely on the left side of the threshold the higher detection accuracy is assured by the CD approach, whereas on the right side of the threshold it is guaranteed by the SCD approach. Moreover, we derived analytically the closed-form expression of the threshold value, which depends on sensing and reporting channel parameters.

Finally, regarding the second spectrum sensing objective, we addressed the spatio-temporal spectrum sensing design problem in the presence of PU mobility with the goal to optimize the sensing time that maximizes the actual transmission capacity achieved by the CU with a limited sensing accuracy, while satisfying the PU interference constraints. More specifically, for the considered scenario, we first introduced the *Mobility-aware Sensing enabled Capacity* (MSC), that is a new performance metric for CR networks that measures the actual transmission capacity achieved by the CU with a limited sensing accuracy, namely by taking into account both the missed temporal and spatial opportunities. Then, it is analytically proven the existence of a single

optimal sensing time that maximizes the MSC, while satisfying the PU interference constraints. Interesting guidelines for spectrum sensing design are also provided that show how the optimal sensing time, which depends on the adopted mobility model, should be set in according to the radio environment conditions. For example, we proved that the optimal sensing time is higher for the Random Walk mobility Model (RWM) than the Random Way-Point mobility Model (RWPM), but the corresponding maximum transmission capacity is even more higher, since the percentage of discovered spatial opportunities is higher in the RWM case. In particular, it is proven through simulations that the transmission capacity can be largely improved by means of cooperative spectrum sensing, and a reduced optimal sensing time can be also achieved.

Appendix A

Proof of Theorem 1

Accounting for (1.10), using the result [103] that $\mathrm{E}[\exp(-\tilde{\mathbf{g}}^H \mathbf{A}\, \tilde{\mathbf{g}})] = \det^{-1}(\mathbf{I}_N + \boldsymbol{\Sigma}_{\tilde{\mathbf{g}}}\, \mathbf{A})$, for $\mathbf{A} \in \mathbb{C}^{(N_{\max}+1)\times(N_{\max}+1)}$, and remembering that $\det(\mathbf{I}_N + \mathbf{B}\,\mathbf{C}) = \det(\mathbf{I}_P + \mathbf{C}\,\mathbf{B})$, for $\mathbf{B} \in \mathbb{C}^{(N_{\max}+1)\times P}$ and $\mathbf{C} \in \mathbb{C}^{P\times(N_{\max}+1)}$, one has

$$
\begin{aligned}
&\mathrm{E}_{\tilde{\mathbf{g}}\,|\,\widetilde{\mathbf{m}}=\mathbf{m},\tilde{\mathbf{s}}=\mathbf{s},\tilde{\boldsymbol{\mathcal{R}}}=\boldsymbol{\mathcal{R}}} \left[\mathrm{PEP}_{\mathrm{iml}}(\tilde{\mathbf{h}}, \tilde{\mathbf{m}})\right] \\
&= \frac{1}{\pi} \int_0^{\pi/2} E_{\tilde{\mathbf{g}}\,|\,\widetilde{\mathbf{m}}=\mathbf{m},\tilde{\mathbf{s}}=\mathbf{s},\tilde{\boldsymbol{\mathcal{R}}}=\boldsymbol{\mathcal{R}}} \left[\exp\left(-\frac{\tilde{\mathbf{g}}^H \mathbf{S}\, \boldsymbol{\mathcal{R}}^H \boldsymbol{\mathcal{C}}_{k,\ell}^H\, \boldsymbol{\Sigma}_{\mathbf{m}}^{-1}\, \boldsymbol{\mathcal{C}}_{k,\ell}\, \boldsymbol{\mathcal{R}}\, \mathbf{S}\, \tilde{\mathbf{g}}}{4\,\sigma^2 \sin^2\theta}\right)\right] \mathrm{d}\theta \\
&= \frac{1}{\pi} \int_0^{\pi/2} \det{}^{-1}\left(\mathbf{I}_P + \gamma\, \frac{\boldsymbol{\Sigma}_{\mathbf{m}}^{-1}\, \boldsymbol{\Phi}_{k,\ell}(\mathbf{s})}{4\, \sin^2\theta}\right) \mathrm{d}\theta \qquad \text{(A.1)}
\end{aligned}
$$

where $\gamma \triangleq 1/\sigma^2$ and $\boldsymbol{\Phi}_{k,\ell}(\mathbf{s}) \triangleq \boldsymbol{\mathcal{C}}_{k,\ell}\, \boldsymbol{\mathcal{R}}\, \mathbf{S}\, \boldsymbol{\Sigma}_{\tilde{\mathbf{g}}}\, \mathbf{S}\, \boldsymbol{\mathcal{R}}^H \boldsymbol{\mathcal{C}}_{k,\ell}^H \in \mathbb{C}^{P\times P}$ is a given matrix. Since the diagonal matrix $\boldsymbol{\Sigma}_{\tilde{\mathbf{g}}}$ is nonsingular and the rank of a matrix is unchanged upon left or right multiplication by a nonsingular matrix [61], it follows that $\mathrm{rank}(\boldsymbol{\Phi}_{k,\ell}(\mathbf{s})) = \mathrm{rank}(\boldsymbol{\mathcal{C}}_{k,\ell}\, \boldsymbol{\mathcal{R}}\, \mathbf{S})$. Moreover, since $\mathrm{rank}(\boldsymbol{\mathcal{C}}_{k,\ell}) = \min(P, L)$ (rank criterion) and $R(\mathbf{s}) = \mathrm{rank}(\boldsymbol{\mathcal{R}}\, \mathbf{S}) = \min(L, N(\mathbf{s})+1)$, it results [61] that $\min(P, L) + R(\mathbf{s}) - L \leq \mathrm{rank}(\boldsymbol{\mathcal{C}}_{k,\ell}\, \boldsymbol{\mathcal{R}}\, \mathbf{S}) \leq \min(\min(P, L), R(\mathbf{s}))$. Hence, in the case of $P \geq L$, one has $\mathrm{rank}(\boldsymbol{\mathcal{C}}_{k,\ell}\, \boldsymbol{\mathcal{R}}\, \mathbf{S}) = R(\mathbf{s})$ and, consequently, because the matrix $\boldsymbol{\Sigma}_{\mathbf{m}}$ is nonsingular, one obtains $\mathrm{rank}(\boldsymbol{\Sigma}_{\mathbf{m}}^{-1}\, \boldsymbol{\Phi}_{k,\ell}(\mathbf{s})) = \mathrm{rank}(\boldsymbol{\Phi}_{k,\ell}(\mathbf{s})) = R(\mathbf{s}) \leq P$. Then, since $\boldsymbol{\Phi}_{k,\ell}(\mathbf{s})$ is a positive semidefinite Hermitian matrix, i.e., its eigenvalues are nonnegative real numbers, and the eigenvalues of the diagonal matrix $\boldsymbol{\Sigma}_{\mathbf{m}}$ are simply equal to its diagonal entries (which are positive and are assumed to be arranged in increasing order,

i.e., $\sigma_{m_1}^2 \leq \sigma_{m_2}^2 \leq \cdots \leq \sigma_{m_P}^2$), one gets

$$\begin{aligned}
&\det\left(\mathbf{I}_P + \gamma\,\frac{\boldsymbol{\Sigma}_{\mathbf{m}}^{-1}\,\boldsymbol{\Phi}_{k,\ell}(\mathbf{s})}{4\,\sin^2\theta}\right) = \prod_{r=1}^{P}\left[1 + \gamma\,\frac{\mu_r(\boldsymbol{\Sigma}_{\mathbf{m}}^{-1}\,\boldsymbol{\Phi}_{k,\ell}(\mathbf{s}))}{4\,\sin^2\theta}\right] \\
&\geq \left(\frac{\gamma}{4\,\sin^2\theta}\right)^{R(\mathbf{s})} \prod_{r=1}^{R(\mathbf{s})} \mu_r(\boldsymbol{\Sigma}_{\mathbf{m}}^{-1}\,\boldsymbol{\Phi}_{k,\ell}(\mathbf{s})) \\
&\geq \left(\frac{\gamma}{4\,\sin^2\theta}\right)^{R(\mathbf{s})} \left(\prod_{p=P-R(\mathbf{s})+1}^{P} \frac{1}{\sigma_{m_p}^2}\right) \left[\prod_{r=1}^{R(\mathbf{s})} \mu_r(\boldsymbol{\Phi}_{k,\ell}(\mathbf{s}))\right]. \qquad \text{(A.2)}
\end{aligned}$$

Therefore, by substituting (A.2) in (A.1) and accounting for (1.4), one has

$$\begin{aligned}
&\mathrm{E}_{\tilde{\mathbf{m}}\,|\,\tilde{\mathbf{s}}=\mathbf{s},\tilde{\boldsymbol{\mathcal{R}}}=\boldsymbol{\mathcal{R}}}\left\{\mathrm{E}_{\tilde{\mathbf{g}}\,|\,\tilde{\mathbf{m}},\tilde{\mathbf{s}}=\mathbf{s},\tilde{\boldsymbol{\mathcal{R}}}=\boldsymbol{\mathcal{R}}}\left[\mathrm{PEP}_{\mathrm{iml}}(\tilde{\mathbf{h}},\tilde{\mathbf{m}})\right]\right\} \\
&\leq \frac{\Theta}{\gamma^{R(\mathbf{s})}}\left(\prod_{p=P-R(\mathbf{s})+1}^{P} \frac{\mathrm{E}[\tilde{m}_p]\,\lambda^{-1}+\Gamma}{1+\Gamma}\right) \\
&\cdot \left[\prod_{r=1}^{R(\mathbf{s})} \mu_r(\boldsymbol{\Phi}_{k,\ell}(\mathbf{s}))\right]^{-1} = \frac{\Theta}{\gamma^{R(\mathbf{s})}} \prod_{r=1}^{R(\mathbf{s})} \mu_r^{-1}(\boldsymbol{\Phi}_{k,\ell}(\mathbf{s})) \qquad \text{(A.3)}
\end{aligned}$$

with $\Theta \triangleq \frac{4^{R(\mathbf{s})}}{\pi}\int_0^{\pi/2}(\sin^2\theta)^{R(\mathbf{s})}\,\mathrm{d}\theta$, where we have also used the fact that the Poisson RVs $\widetilde{m}_1, \widetilde{m}_2, \ldots, \widetilde{m}_P$ are statistically independent and $\mathrm{E}[\tilde{m}_p] = \lambda$. Let $\boldsymbol{\mathcal{R}}\,\mathbf{S}\,\boldsymbol{\Sigma}_{\tilde{\mathbf{g}}}\,\mathbf{S}\,\boldsymbol{\mathcal{R}}^H = \mathbf{U}\,\boldsymbol{\Omega}\,\mathbf{U}^H$ be the economy-size eigenvalue decomposition of $\boldsymbol{\mathcal{R}}\,\mathbf{S}\,\boldsymbol{\Sigma}_{\tilde{\mathbf{g}}}\,\mathbf{S}\,\boldsymbol{\mathcal{R}}^H$, with $\mathbf{U} \in \mathbb{C}^{L\times R(\mathbf{s})}$ satisfying $\mathbf{U}^H\,\mathbf{U} = \mathbf{I}_{R(\mathbf{s})}$ and

$$\begin{aligned}
\boldsymbol{\Omega} = \mathrm{diag}[&\mu_1(\boldsymbol{\mathcal{R}}\,\mathbf{S}\,\boldsymbol{\Sigma}_{\tilde{\mathbf{g}}}\,\mathbf{S}\,\boldsymbol{\mathcal{R}}^H), \mu_2(\boldsymbol{\mathcal{R}}\,\mathbf{S}\,\boldsymbol{\Sigma}_{\tilde{\mathbf{g}}}\,\mathbf{S}\,\boldsymbol{\mathcal{R}}^H), \ldots, \\
&\mu_R(\boldsymbol{\mathcal{R}}\,\mathbf{S}\,\boldsymbol{\Sigma}_{\tilde{\mathbf{g}}}\,\mathbf{S}\,\boldsymbol{\mathcal{R}}^H)] \in \mathbb{R}^{R(\mathbf{s})\times R(\mathbf{s})} \qquad \text{(A.4)}
\end{aligned}$$

one has $\mu_r(\mathbf{\Phi}_{k,\ell}(\mathbf{s})) = \mu_r(\boldsymbol{\mathcal{C}}_{k,\ell}\,\mathbf{U}\,\mathbf{\Omega}\,\mathbf{U}^H\boldsymbol{\mathcal{C}}_{k,\ell}^H) = \mu_r(\mathbf{\Omega}\,\mathbf{U}^H\boldsymbol{\mathcal{C}}_{k,\ell}^H\,\boldsymbol{\mathcal{C}}_{k,\ell}\,\mathbf{U})$, for $r \in \{1, 2, \ldots, R(\mathbf{s})\}$. Moreover, it can be shown (see, e.g., [104]) that

$$\begin{aligned}
&\prod_{r=1}^{R(\mathbf{s})} \mu_r(\mathbf{\Phi}_{k,\ell}(\mathbf{s})) = \prod_{r=1}^{R(\mathbf{s})} \mu_r(\mathbf{\Omega}\,\mathbf{U}^H\boldsymbol{\mathcal{C}}_{k,\ell}^H\,\boldsymbol{\mathcal{C}}_{k,\ell}\,\mathbf{U}) \\
&\geq \left[\prod_{r=1}^{R(\mathbf{s})} \mu_r(\boldsymbol{\mathcal{R}}\,\mathbf{S}\,\mathbf{\Sigma}_{\tilde{\mathbf{g}}}\,\mathbf{S}\,\boldsymbol{\mathcal{R}}^H)\right]\left[\prod_{r=L-R(\mathbf{s})+1}^{L} \mu_r(\mathbf{U}^H\boldsymbol{\mathcal{C}}_{k,\ell}^H\,\boldsymbol{\mathcal{C}}_{k,\ell}\,\mathbf{U})\right] \\
&\geq \left[\prod_{r=1}^{R(\mathbf{s})} \mu_r(\boldsymbol{\mathcal{R}}\,\mathbf{S}\,\mathbf{\Sigma}_{\tilde{\mathbf{g}}}\,\mathbf{S}\,\boldsymbol{\mathcal{R}}^H)\right]\left[\prod_{r=L-R(\mathbf{s})+1}^{L} \mu_r(\boldsymbol{\mathcal{C}}_{k,\ell}^H\,\boldsymbol{\mathcal{C}}_{k,\ell})\right]. \qquad \text{(A.5)}
\end{aligned}$$

Similarly, it can be seen that

$$\begin{aligned}
&\prod_{r=1}^{R(\mathbf{s})} \mu_r(\boldsymbol{\mathcal{R}}\,\mathbf{S}\,\mathbf{\Sigma}_{\tilde{\mathbf{g}}}\,\mathbf{S}\,\boldsymbol{\mathcal{R}}^H) = \prod_{r=1}^{R(\mathbf{s})} \mu_r(\mathbf{\Sigma}_{\tilde{\mathbf{g}}}\,\mathbf{S}\,\boldsymbol{\mathcal{R}}^H\boldsymbol{\mathcal{R}}\,\mathbf{S}) \\
&\geq \left[\prod_{r=N(\mathbf{s})-R(\mathbf{s})+1}^{N(\mathbf{s})} \sigma_{\tilde{g}_r}^2\right]\left[\prod_{r=1}^{R(\mathbf{s})} \mu_r(\mathbf{S}\,\boldsymbol{\mathcal{R}}^H\boldsymbol{\mathcal{R}}\,\mathbf{S})\right]. \qquad \text{(A.6)}
\end{aligned}$$

The expression (1.12) comes from by substituting (A.5) and (A.6) in (A.3), and accounting for (1.11).

Appendix B

Proof of Lemma 1

Let us study the solution of (1.20). The eigenvalues $\mu_r(\boldsymbol{\mathcal{R}}^H\boldsymbol{\mathcal{R}})$ are necessarily positive for $r \in \{1, 2, \ldots, R_{\max}\}$, whereas $\mu_r(\boldsymbol{\mathcal{R}}^H\boldsymbol{\mathcal{R}}) = 0$ for $r \in \{R_{\max}+1, R_{\max}+2, \ldots, N_{\max}+1\}$. Thus, application of the arithmetic-geometric mean inequality for nonnegative real numbers [61] leads to

$$\begin{aligned}\prod_{r=1}^{R_{\max}} \mu_r(\boldsymbol{\mathcal{R}}^H\boldsymbol{\mathcal{R}}) &\leq \left[\frac{1}{R_{\max}} \sum_{r=1}^{R_{\max}} \mu_r(\boldsymbol{\mathcal{R}}^H\boldsymbol{\mathcal{R}})\right]^{R_{\max}} \\ &= \left[\frac{1}{R_{\max}} \operatorname{trace}(\boldsymbol{\mathcal{R}}^H\boldsymbol{\mathcal{R}})\right]^{R_{\max}} = \left(\frac{\rho}{R_{\max}}\right)^{R_{\max}} \qquad \text{(B.1)}\end{aligned}$$

where we have also applied the constraint $\operatorname{trace}(\boldsymbol{\mathcal{R}}^H\boldsymbol{\mathcal{R}}) = \rho$. In (B.1), equality holds if and only if

$$\mu_r(\boldsymbol{\mathcal{R}}^H\boldsymbol{\mathcal{R}}) = \frac{\rho}{R_{\max}} \quad \text{for } r \in \{1, 2, \ldots, R_{\max}\}\,. \qquad \text{(B.2)}$$

When $L < N_{\max}+1$, i.e., $R_{\max} = L$, one has that $\mu_r(\boldsymbol{\mathcal{R}}^H\boldsymbol{\mathcal{R}}) = \mu_r(\boldsymbol{\mathcal{R}}\,\boldsymbol{\mathcal{R}}^H)$, for $r \in \{1, 2, \ldots, L\}$, and $\boldsymbol{\mathcal{R}}\,\boldsymbol{\mathcal{R}}^H$ is positive definite. In this case, condition (B.2) is fulfilled if and only if $\boldsymbol{\mathcal{R}}_{\text{opt}}\,\boldsymbol{\mathcal{R}}_{\text{opt}}^H = (\rho/L)\,\mathbf{I}_L$.

Let us now derive the solution of (1.21). The eigenvalues given by $\mu_r(\mathbf{S}\,\boldsymbol{\mathcal{R}}^H\boldsymbol{\mathcal{R}}\,\mathbf{S})$ are necessarily positive for $r \in \{1, 2, \ldots, R(\mathbf{s})\}$, whereas $\mu_r(\mathbf{S}\,\boldsymbol{\mathcal{R}}^H\boldsymbol{\mathcal{R}}\,\mathbf{S}) = 0$ for $r \in \{R(\mathbf{s})+1, R(\mathbf{s})+2, \ldots, N(\mathbf{s})+1\}$. Thus, applying again the arithmetic-geometric mean inequality, using the constraint $\operatorname{trace}(\mathbf{S}\,\boldsymbol{\mathcal{R}}^H\boldsymbol{\mathcal{R}}\,\mathbf{S}) = \rho\,R(\mathbf{s})/R_{\max}$, and reasoning as done above,

one has that $\prod_{r=1}^{R(\mathbf{s})} \mu_r(\mathbf{S}\,\boldsymbol{\mathcal{R}}^H\boldsymbol{\mathcal{R}}\,\mathbf{S})$ is maximized when

$$\mu_r(\mathbf{S}\,\boldsymbol{\mathcal{R}}^H\boldsymbol{\mathcal{R}}\,\mathbf{S}) = \frac{\rho}{R_{\max}} \quad \text{for } r \in \{1, 2, \ldots, R(\mathbf{s})\} \tag{B.3}$$

and the corresponding maximum value is $(\rho/R_{\max})^{R(\mathbf{s})}$. Since $L \geq N_{\max} + 1$, it follows that $R_{\max} = N_{\max} + 1$ and $R(\mathbf{s}) = N(\mathbf{s}) + 1$. Let $\boldsymbol{\mathcal{R}}(\mathbf{s}) \in \mathbb{C}^{L\times(N(\mathbf{s})+1)}$ denote the matrix $\boldsymbol{\mathcal{R}}\,\mathbf{S}$ deprived of all its zero columns, then $\mu_r(\mathbf{S}\,\boldsymbol{\mathcal{R}}^H\boldsymbol{\mathcal{R}}\,\mathbf{S}) = \mu_r(\boldsymbol{\mathcal{R}}^H(\mathbf{s})\,\boldsymbol{\mathcal{R}}(\mathbf{s}))$. Consequently $\boldsymbol{\mathcal{R}}^H(\mathbf{s})\,\boldsymbol{\mathcal{R}}(\mathbf{s})$ is positive definite and, hence, condition (B.3) is fulfilled for each realization $\mathbf{s}$ of $\tilde{\mathbf{s}}$ if and only if $\boldsymbol{\mathcal{R}}_{\text{opt}}^H\,\boldsymbol{\mathcal{R}}_{\text{opt}} = [\rho/(N_{\max}+1)]\,\mathbf{I}_{N_{\max}+1}$.

Appendix C

Proof of Theorem 2

Accounting for (A.1), using (1.4), and remembering that the Poisson RVs $\widetilde{m}_1, \widetilde{m}_2, \ldots, \widetilde{m}_P$ are statistically independent, one obtains

$$\begin{aligned}\mathrm{APEP}(\gamma) &= \mathrm{E}_{\tilde{\mathbf{m}}\,|\,\tilde{\mathbf{s}}=\mathbf{1}_{N_{\max}},\tilde{\boldsymbol{\mathcal{R}}}=\boldsymbol{\mathcal{R}}}\left\{\mathrm{E}_{\tilde{\mathbf{g}}\,|\,\tilde{\mathbf{m}},\tilde{\mathbf{s}}=\mathbf{1}_{N_{\max}},\tilde{\boldsymbol{\mathcal{R}}}=\boldsymbol{\mathcal{R}}}\left[\mathrm{PEP}_{\mathrm{iml}}(\tilde{\mathbf{h}},\tilde{\mathbf{m}})\right]\right\} \\ &= \frac{1}{\pi}\sum_{m_1=0}^{+\infty}\sum_{m_2=0}^{+\infty}\cdots\sum_{m_P=0}^{+\infty}\left[\prod_{p=1}^{P} p_{\widetilde{m}_p}(m_p)\right] \\ &\qquad \cdot\int_0^{\pi/2}\det{}^{-1}\left(\mathbf{I}_P+\gamma\,\frac{\boldsymbol{\Sigma}_{\mathbf{m}}^{-1}\,\boldsymbol{\Phi}_{k,\ell}}{4\,\sin^2\theta}\right)\mathrm{d}\theta \quad \text{(C.1)}\end{aligned}$$

with $\boldsymbol{\Phi}_{k,\ell} \triangleq \boldsymbol{\Phi}_{k,\ell}(\mathbf{1}_{\max})$ (see Appendix A). It is convenient to observe that, by virtue of (1.4), one can write

$$\prod_{p=1}^{P} p_{\widetilde{m}_p}(m_p) = \exp(-\lambda\,P)\prod_{p=1}^{P}\frac{\lambda^{m_p}}{m_p!} = \exp(-\lambda\,P)\det(\boldsymbol{\Lambda}_{\mathbf{m}}) \qquad \text{(C.2)}$$

where $\boldsymbol{\Lambda}_{\mathbf{m}} \triangleq \mathrm{diag}(\lambda^{m_1}/m_1!, \lambda^{m_2}/m_2!, \ldots, \lambda^{m_P}/m_P!)$. According to (1.1), we have to evaluate the derivative of $\mathrm{APEP}(\gamma)$ with respect to the SNR. By invoking the Leibnitz's rule, one gets

$$\begin{aligned}\frac{\mathrm{d}\,\mathrm{APEP}(\gamma)}{\mathrm{d}\gamma} &= \frac{\exp(-\lambda\,P)}{\pi}\sum_{m_1=0}^{+\infty}\sum_{m_2=0}^{+\infty}\cdots\sum_{m_P=0}^{+\infty}\det(\boldsymbol{\Lambda}_{\mathbf{m}}) \\ &\qquad \cdot\int_0^{\pi/2}\frac{\partial}{\partial\gamma}\det{}^{-1}\left(\mathbf{I}_P+\gamma\,\frac{\boldsymbol{\Sigma}_{\mathbf{m}}^{-1}\,\boldsymbol{\Phi}_{k,\ell}}{4\,\sin^2\theta}\right)\mathrm{d}\theta \quad \text{(C.3)}\end{aligned}$$

where, by observing that

$$\frac{\partial \det(\mathbf{A})}{\partial \gamma} = \det(\mathbf{A}) \operatorname{trace}\left(\mathbf{A}^{-1} \frac{\partial \mathbf{A}}{\partial \gamma}\right)$$

where $\mathbf{A}$ is an arbitrary nonsingular square matrix depending on γ, it follows that

$$\frac{\partial}{\partial \gamma} \det{}^{-1}\left(\mathbf{I}_P + \gamma \frac{\boldsymbol{\Sigma}_{\mathbf{m}}^{-1} \boldsymbol{\Phi}_{k,\ell}}{4 \sin^2 \theta}\right) = -\det{}^{-1}\left(\mathbf{I}_P + \gamma \frac{\boldsymbol{\Sigma}_{\mathbf{m}}^{-1} \boldsymbol{\Phi}_{k,\ell}}{4 \sin^2 \theta}\right) \cdot \operatorname{trace}\left[\left(\mathbf{I}_P + \gamma \frac{\boldsymbol{\Sigma}_{\mathbf{m}}^{-1} \boldsymbol{\Phi}_{k,\ell}}{4 \sin^2 \theta}\right)^{-1} \frac{\boldsymbol{\Sigma}_{\mathbf{m}}^{-1} \boldsymbol{\Phi}_{k,\ell}}{4 \sin^2 \theta}\right] . \quad \text{(C.4)}$$

After simple rearrangements, eq. (1.23) comes from by substituting (C.1), (C.2), (C.3), and (C.4) in (1.1), and accounting for (1.22). The rank of the matrix $\boldsymbol{\Sigma}_{\mathbf{m}}^{-1} \boldsymbol{\Phi}_{k,\ell}$ can be obtained by the discussion in Appendix A.

Appendix D

Proof of Theorem 3

Starting from (1.41) and reasoning as done for obtaining (A.1), one gets

$$\begin{aligned}
&\mathrm{E}_{\tilde{\mathbf{g}}\,|\,\tilde{\mathbf{m}}=\mathbf{m},\tilde{\mathbf{s}}=\mathbf{s},,\tilde{\boldsymbol{\mathcal{R}}}=\boldsymbol{\mathcal{R}}}\left[\mathrm{PEP}_{\mathrm{md}}(\tilde{\mathbf{h}},\tilde{\mathbf{m}})\right] \\
&\leq \frac{1}{\pi}\int_0^{\pi/2} E_{\tilde{\mathbf{g}}\,|\,\tilde{\mathbf{m}}=\mathbf{m},\tilde{\mathbf{s}}=\mathbf{s},\tilde{\boldsymbol{\mathcal{R}}}=\boldsymbol{\mathcal{R}}}\left[\exp\left(-\frac{\tilde{\mathbf{g}}^H\,\mathbf{S}\,\boldsymbol{\mathcal{R}}^H\,\boldsymbol{\mathcal{C}}_{k,\ell}^H\,\boldsymbol{\mathcal{C}}_{k,\ell}\,\boldsymbol{\mathcal{R}}\,\mathbf{S}\,\tilde{\mathbf{g}}}{4\,\sigma^2\,\mu_1(\boldsymbol{\Sigma}_{\mathbf{m}})\,\sin^2\theta}\right)\right]\,\mathrm{d}\theta \\
&= \frac{1}{\pi}\int_0^{\pi/2} \det{}^{-1}\left[\mathbf{I}_P+\gamma\,\frac{\boldsymbol{\Phi}_{k,\ell}(\mathbf{s})}{4\,\mu_1(\boldsymbol{\Sigma}_{\mathbf{m}})\,\sin^2\theta}\right]\,\mathrm{d}\theta \qquad \text{(D.1)}
\end{aligned}$$

where γ and $\boldsymbol{\Phi}_{k,\ell}(\mathbf{s})$ have been defined in Appendix A. Using (D.1) and following the same steps that leaded to (A.2), one has

$$\begin{aligned}
&\mathrm{E}_{\tilde{\mathbf{g}}\,|\,\tilde{\mathbf{m}}=\mathbf{m},\tilde{\mathbf{s}}=\mathbf{s},\tilde{\boldsymbol{\mathcal{R}}}=\boldsymbol{\mathcal{R}}}\left[\mathrm{PEP}_{\mathrm{md}}(\tilde{\mathbf{h}},\tilde{\mathbf{m}})\right] \\
&\qquad\qquad \leq [\mu_1(\boldsymbol{\Sigma}_{\mathbf{m}})]^{R(\mathbf{s})}\,\frac{\Theta}{\gamma^{R(\mathbf{s})}}\,\prod_{r=1}^{R(\mathbf{s})}\mu_r^{-1}(\boldsymbol{\Phi}_{k,\ell}(\mathbf{s})) \qquad \text{(D.2)}
\end{aligned}$$

where Θ has been defined in Appendix A. Therefore, by observing that $\mu_1(\boldsymbol{\Sigma}_{\mathbf{m}}) = \max(\sigma_{m_1}^2,\sigma_{m_2}^2,\ldots,\sigma_{m_P}^2)$ and accounting for (1.4), one has

$$\begin{aligned}
&\mathrm{E}_{\tilde{\mathbf{m}}\,|\,\tilde{\mathbf{s}}=\mathbf{s},\tilde{\boldsymbol{\mathcal{R}}}=\boldsymbol{\mathcal{R}}}\left\{\mathrm{E}_{\tilde{\mathbf{g}}\,|\,\tilde{\mathbf{m}},\tilde{\mathbf{s}}=\mathbf{s},\tilde{\boldsymbol{\mathcal{R}}}=\boldsymbol{\mathcal{R}}},\left[\mathrm{PEP}_{\mathrm{md}}(\tilde{\mathbf{h}},\tilde{\mathbf{m}})\right]\right\} \\
&\qquad\qquad \leq \mathrm{E}\left[\left(\frac{\tilde{m}\,\lambda^{-1}+\Gamma}{1+\Gamma}\right)^{R(\mathbf{s})}\right]\,\frac{\Theta}{\gamma^{R(\mathbf{s})}}\,\prod_{r=1}^{R(\mathbf{s})}\mu_r^{-1}(\boldsymbol{\Phi}_{k,\ell}(\mathbf{s})) \qquad \text{(D.3)}
\end{aligned}$$

where $\tilde{m} \triangleq \max\{\tilde{m}_1, \tilde{m}_2, \ldots, \tilde{m}_P\}$. Since the maximum of P quantities is less than or equal to any number $m \in \mathbb{N}$ if and only if all of these quantities are less than or equal to m, and $\tilde{m}_1, \tilde{m}_2, \ldots, \tilde{m}_P$ are i.i.d. RVs, it follows that $P(\tilde{m} \leq m) = [F(m)]^P$ and $P(\tilde{m} \geq m) = 1 - [F(m-1)]^P$, where $F(m) \triangleq F_{\tilde{m}_p}(m) = \sum_{i=0}^{m} p_{\tilde{m}_p}(i)$ is the cumulative distribution function (CDF) of $\tilde{m}_p$, which does not depend on p. Consequently, one has

$$\begin{aligned} P(\tilde{m} = m) &= P(\{\tilde{m} \leq m\} \cap \{\tilde{m} \geq m\}) \\ &= [F(m)]^P - [F(m-1)]^P \\ &\leq P\,[F(m) - F(m-1)] = P\,p_{\tilde{m}_p}(m) \end{aligned} \tag{D.4}$$

where the inequality comes from the Ruffini's rule and from the fact that the CDF of a RV is a positive number less than or equal to one. Thus, one has

$$\begin{aligned} \mathrm{E}\left[\left(\frac{\tilde{m}\,\lambda^{-1} + \Gamma}{1 + \Gamma}\right)^{R(\mathbf{s})}\right] &= \sum_{m=0}^{+\infty} \left(\frac{m\,\lambda^{-1} + \Gamma}{1 + \Gamma}\right)^{R(\mathbf{s})} P(\tilde{m} = m) \\ &\leq P\,\mathrm{E}\left[\left(\frac{\widetilde{m}_p\,\lambda^{-1} + \Gamma}{1 + \Gamma}\right)^{R(\mathbf{s})}\right]. \end{aligned} \tag{D.5}$$

Inequality (1.42) comes from by substituting (A.5), (A.6), and (D.5) in (D.3).

Appendix E

Proof of Proposition 1

By exploiting (2.25), $\mathbf{C}_{\mathbf{y}_{\mathrm{sc,a}}|\mathcal{H}_j}$ results rank-deficient, since $2\,L_e$ rows (equivalently $2\,L_e$ columns) are equal. In fact, the first L_e rows (L_e columns) of both $\mathbf{C}_{\mathbf{y}_{\mathrm{sc}}|\mathcal{H}_j}$ in (2.10) and $\mathbf{C}_{\mathbf{y}^*_{\mathrm{sc}}|\mathcal{H}_j}$ in (2.13) are equal to the real matrix $\mathbf{C}_{\mathbf{y}_0|\mathcal{H}_j}$ in (2.11). By accounting for footnote 7, after some algebraic manipulations, it is easy to show that $\mathbf{C}_{\mathbf{y}_{\mathrm{sc,a}}|\mathcal{H}_j}$ admits the full-rank factorization [78]: $\mathbf{C}_{\mathbf{y}_{\mathrm{sc,a}}|\mathcal{H}_j} = \mathbf{F}\,\mathbf{\Psi}$, i.e., it can be rewritten as product of a full-column rank matrix $\mathbf{F} \in \mathbb{C}^{(2\,M\,L_e)\times(2\,M-1)\,L_e}$ and a full-row rank matrix $\mathbf{\Psi} \in \mathbb{R}^{(2M-1)L_e \times 2ML_e}$, given by, respectively,

$$\boldsymbol{F} \triangleq \begin{bmatrix} \mathbf{0}_{L_e\times(M-1)L_e} & \mathbf{C}_{\mathbf{y}_0|\mathcal{H}_j} & \mathbf{0}_{L_e\times(M-1)L_e} \\ \mathbf{C}_{\overline{\mathbf{y}}|\mathcal{H}_j} & \mathbf{0}_{(M-1)L_e\times L_e} & \mathbf{C}_{\overline{\mathbf{y}}^*|\mathcal{H}_j} \\ \mathbf{0}_{L_e\times(M-1)L_e} & \mathbf{C}_{\mathbf{y}_0|\mathcal{H}_j} & \mathbf{0}_{L_e\times(M-1)L_e} \\ \mathbf{C}^*_{\overline{\mathbf{y}}^*|\mathcal{H}_j} & \mathbf{0}_{(M-1)L_e\times L_e} & \mathbf{C}^*_{\overline{\mathbf{y}}|\mathcal{H}_j}, \end{bmatrix} \tag{E.1}$$

$$\mathbf{\Psi} \triangleq \begin{bmatrix} \mathbf{0}_{(M-1)L_e\times L_e} & \mathbf{I}_{(M-1)L_e} & \mathbf{0}_{(M-1)L_e\times L_e} & \mathbf{0}_{(M-1)L_e\times(M-1)L_e} \\ \mathbf{I}_{L_e} & \mathbf{0}_{L_e\times(M-1)L_e} & \mathbf{I}_{L_e} & \mathbf{0}_{L_e\times(M-1)L_e} \\ \mathbf{0}_{(M-1)L_e\times L_e} & \mathbf{0}_{(M-1)L_e\times(M-1)L_e} & \mathbf{0}_{(M-1)L_e\times L_e} & \mathbf{I}_{(M-1)L_e} \end{bmatrix} \tag{E.2}$$

Hence, the Moore-Penrose inverse of $\mathbf{C}_{\mathbf{y}_{\mathrm{sc,a}}|\mathcal{H}_j}$ is equal [78] to: $\mathbf{C}^{\dagger}_{\mathbf{y}_{\mathrm{sc,a}}|\mathcal{H}_j} = (\mathbf{F}\,\mathbf{\Psi})^{\dagger} = \mathbf{\Psi}^H(\mathbf{\Psi}\mathbf{\Psi}^H)^{-1}(\mathbf{F}^H\mathbf{F})^{-1}\mathbf{F}^H$. Since one has that $\mathrm{rank}(\mathbf{C}_{\mathbf{y}_{\mathrm{sc,a}}|\mathcal{H}_j}) = \mathrm{rank}(\mathbf{C}^{\dagger}_{\mathbf{y}_{\mathrm{sc,a}}|\mathcal{H}_j}\,\mathbf{C}_{\mathbf{y}_{\mathrm{sc,a}}|\mathcal{H}_j}) = \mathrm{trace}(\mathbf{C}^{\dagger}_{\mathbf{y}_{\mathrm{sc,a}}|\mathcal{H}_j}\mathbf{C}_{\mathbf{y}_{\mathrm{sc,a}}|\mathcal{H}_j})$, being $\mathbf{C}^{\dagger}_{\mathbf{y}_{\mathrm{sc,a}}|\mathcal{H}_j}\,\mathbf{C}_{\mathbf{y}_{\mathrm{sc,a}}|\mathcal{H}_j}$ idempotent [78], it results that: $\mathrm{rank}(\mathbf{C}_{\mathbf{y}_{\mathrm{sc,a}}|\mathcal{H}_j}) = \mathrm{trace}((\mathbf{\Psi}\mathbf{\Psi}^H)^{-1}\mathbf{\Psi}\mathbf{\Psi}^H) = \mathrm{trace}(\mathbf{I}_{(2M-1)L_e}) = (2M-1)L_e$.

Appendix F

Proof of Theorem 5

Since the solution of (2.30) belongs to $\mathcal{R}(\mathbf{C}_{\mathbf{y}_{\mathrm{sc,a}}|\mathcal{H}_1})$ (Proposition 2), and $\mathbf{C}^{\dagger}_{\mathbf{y}_{\mathrm{sc,a}}|\mathcal{H}_1}\mathbf{C}_{\mathbf{y}_{\mathrm{sc,a}}|\mathcal{H}_1} = \mathbf{P}_{\mathcal{R}(\mathbf{C}_{\mathbf{y}_{\mathrm{sc,a}}|\mathcal{H}_1})}$, with $\mathbf{P}_{\mathcal{R}(\mathbf{C}_{\mathbf{y}_{\mathrm{sc,a}}|\mathcal{H}_1})}$ the orthogonal projector on $\mathcal{R}(\mathbf{C}_{\mathbf{y}_{\mathrm{a}}|\mathcal{H}_1})$ [78], it results:

$$\mathbf{C}^{\dagger}_{\mathbf{y}_{\mathrm{sc,a}}|\mathcal{H}_1}\mathbf{C}_{\mathbf{y}_{\mathrm{sc,a}}|\mathcal{H}_1}\mathbf{f}_{\mathrm{sc}} = \mathbf{f}_{\mathrm{sc}} \Leftrightarrow \mathbf{f}_{\mathrm{sc}} \in \mathcal{R}(\mathbf{C}_{\mathbf{y}_{\mathrm{sc,a}}|\mathcal{H}_1}) \tag{F.1}$$

Hence, by using (F.1) and the Cauchy-Schwartz's inequality in the DC expression one obtains

$$\begin{aligned} m^2_{\mathrm{wl}}(\mathbf{f}_{\mathrm{sc}}) &= \frac{|(\mathbf{C}^{1/2}_{\mathbf{y}_{\mathrm{sc,a}}|\mathcal{H}_1}\mathbf{f}_{\mathrm{sc}})^H\mathbf{C}^{1/2}_{\mathbf{y}_{\mathrm{sc,a}}|\mathcal{H}_1}\mathbf{C}^{\dagger}_{\mathbf{y}_{\mathrm{sc,a}}|\mathcal{H}_1}(\widetilde{\boldsymbol{\mu}}_{\mathrm{sc}|\mathcal{H}_1} - \widetilde{\boldsymbol{\mu}}_{\mathrm{sc}|\mathcal{H}_0})|^2}{\mathbf{f}^H_{\mathrm{sc}}\mathbf{C}_{\mathbf{y}_{\mathrm{sc,a}}|\mathcal{H}_1}\mathbf{f}_{\mathrm{sc}}} \\ &\leq (\widetilde{\boldsymbol{\mu}}_{\mathrm{sc}|\mathcal{H}_1} - \widetilde{\boldsymbol{\mu}}_{\mathrm{sc}|\mathcal{H}_0})^H\mathbf{C}^{\dagger}_{\mathbf{y}_{\mathrm{sc,a}}|\mathcal{H}_1}(\widetilde{\boldsymbol{\mu}}_{\mathrm{sc}|\mathcal{H}_1} - \widetilde{\boldsymbol{\mu}}_{\mathrm{sc}|\mathcal{H}_0}) \end{aligned} \tag{F.2}$$

where the equality holds if $\mathbf{C}^{1/2}_{\mathbf{y}_{\mathrm{sc,a}}|\mathcal{H}_1}\mathbf{f}_{\mathrm{sc}} = \xi\mathbf{C}^{1/2}_{\mathbf{y}_{\mathrm{sc,a}}|\mathcal{H}_1}\mathbf{C}^{\dagger}_{\mathbf{y}_{\mathrm{sc,a}}|\mathcal{H}_1}(\widetilde{\boldsymbol{\mu}}_{\mathrm{sc}|\mathcal{H}_1} - \widetilde{\boldsymbol{\mu}}_{\mathrm{sc}|\mathcal{H}_0}) \Leftrightarrow \mathbf{f}_{\mathrm{sc}} = \mathbf{f}_{\text{wl-sc}} = \xi\,\mathbf{C}^{\dagger}_{\mathbf{y}_{\mathrm{sc,a}}|\mathcal{H}_1}(\widetilde{\boldsymbol{\mu}}_{\mathrm{sc}|\mathcal{H}_1} - \widetilde{\boldsymbol{\mu}}_{\mathrm{sc}|\mathcal{H}_0})$. The constraint $\mathbf{f}^H_{\mathrm{sc}}\mathbf{f}_{\mathrm{sc}} = 1$ is satisfied by $\xi = 1/||\mathbf{C}^{\dagger}_{\mathbf{y}_{\mathrm{sc,a}}|\mathcal{H}_1}(\widetilde{\boldsymbol{\mu}}_{\mathrm{sc}|\mathcal{H}_1} - \widetilde{\boldsymbol{\mu}}_{\mathrm{sc}|\mathcal{H}_0})||^2_2$, which is real to assure the conjugate symmetric property of $\mathbf{f}_{\mathrm{sc}}$.

Appendix G

Proof of Proposition 3

Sensing & Combining Decision approach case: For Proposition 1, $\mathbf{C}_{\mathbf{y}_{\text{sc,a}}|\mathcal{H}_1}$ has at least one non-singular submatrix $\mathbf{X}_{11} \in \mathbb{C}^{(2\,M-1)L_e \times (2\,M-1)L_e}$ such that: $\mathbf{P}\,\mathbf{C}_{\mathbf{y}_{\text{sc,a}}|\mathcal{H}_1}\,\mathbf{Q} = \begin{bmatrix} \mathbf{X}_{11} & \mathbf{X}_{12} \\ \mathbf{X}_{21} & \mathbf{X}_{22} \end{bmatrix}$, where $\mathbf{P}$ and $\mathbf{Q}$ are permutation matrices, [78]. By defining $\mathbf{P} \triangleq \begin{bmatrix} \mathbf{0}_{(2\,M-1)L_e \times L_e} & \mathbf{I}_{(2\,M-1)L_e} \\ \mathbf{I}_{L_e} & \mathbf{0}_{L_e \times (2\,M-1)L_e} \end{bmatrix} \in \mathbb{R}^{2\,M\,L_e \times 2\,M\,L_e}$ and $\mathbf{Q} \triangleq \mathbf{P}^T$, it results:

$$\mathbf{X}_{11} = \begin{bmatrix} \begin{bmatrix} \mathbf{C}_{\overline{\mathbf{y}}|\mathcal{H}_1} & \mathbf{0}_{(M-1)L_e \times L_e} \\ \mathbf{0}_{L_e \times (M-1)L_e} & \mathbf{C}_{\mathbf{y}_0|\mathcal{H}_1} \end{bmatrix} & \begin{bmatrix} \mathbf{C}_{\overline{\mathbf{y}}^*|\mathcal{H}_1} \\ \mathbf{0}_{L_e \times (M-1)L_e} \end{bmatrix} \\ \begin{bmatrix} \mathbf{C}^*_{\overline{\mathbf{y}}^*|\mathcal{H}_1} & \mathbf{0}_{(M-1)L_e \times L_e} \end{bmatrix} & \begin{bmatrix} \mathbf{C}^*_{\overline{\mathbf{y}}|\mathcal{H}_1} \end{bmatrix} \end{bmatrix} \tag{G.1}$$

$$\begin{aligned} \mathbf{X}_{21} &= \begin{bmatrix} \mathbf{0}_{L_e \times (M-1)L_e} & \mathbf{C}_{\mathbf{y}_0|\mathcal{H}_1} & \mathbf{0}_{L_e \times (M-1)L_e} \end{bmatrix} = \mathbf{X}_{12}^T \\ \mathbf{X}_{22} &= \mathbf{C}_{\mathbf{y}_0|\mathcal{H}_1}. \end{aligned} \tag{G.2}$$

By substituting (G.1) and (G.2) in the Noble's equality [78], and by denoting with $\mathbf{C}^{\dagger}_{\mathbf{y}_{\text{sc,a}}|\mathcal{H}_1} \triangleq \begin{bmatrix} \mathbf{\Phi}_{11} & \mathbf{\Phi}_{12} \\ \mathbf{\Phi}_{21} & \mathbf{\Phi}_{22} \end{bmatrix}$, after some algebraic manipulations, we obtain:

$$\mathbf{\Phi}_{11} = \mathbf{\Phi}^*_{22} = \begin{bmatrix} \frac{1}{4}\mathbf{C}^{-1}_{\mathbf{y}_0|\mathcal{H}_1} & \mathbf{0}_{L_e \times (M-1)L_e} \\ \mathbf{0}_{(M-1)L_e \times L_e} & \overline{\mathbf{\Omega}} \end{bmatrix} \tag{G.3}$$

$$\mathbf{\Phi}_{12} = \mathbf{\Phi}^*_{21} = \begin{bmatrix} \frac{1}{4}\mathbf{C}^{-1}_{\mathbf{y}_0|\mathcal{H}_1} & \mathbf{0}_{L_e \times (M-1)L_e} \\ \mathbf{0}_{(M-1)L_e \times L_e} & -\mathbf{C}^{-1}_{\overline{\mathbf{y}}|\mathcal{H}_1}\mathbf{C}_{\overline{\mathbf{y}}^*|\mathcal{H}_1}\overline{\mathbf{\Omega}}^* \end{bmatrix} \tag{G.4}$$

with $\overline{\mathbf{\Omega}}$ given in (2.44). By exploiting (2.31), the WL subvector $\mathbf{t}_{\text{wl-sc}}$ is expressed as:

$$\mathbf{t}_{\text{wl-sc}} = \frac{(\mathbf{\Phi}_{11}\mathbf{H}_{\text{sc}} + \mathbf{\Phi}_{12}\mathbf{H}^*_{\text{sc}})(\boldsymbol{\eta}_{\text{sc}|\mathcal{H}_1} - \boldsymbol{\eta}_{\text{sc}|\mathcal{H}_0})}{\sqrt{2}\,||(\mathbf{\Phi}_{11}\mathbf{H}_{\text{sc}} + \mathbf{\Phi}_{12}\mathbf{H}^*_{\text{sc}})(\boldsymbol{\eta}_{\text{sc}|\mathcal{H}_1} - \boldsymbol{\eta}_{\text{sc}|\mathcal{H}_0})||_2^2} \tag{G.5}$$

The proof is achieved by substituting $\mathbf{\Phi}_{11}$ and $\mathbf{\Phi}_{12}$ in (G.5) and by using the expression of $\mathbf{H}_{\text{sc}}$.

Combining Decision approach case: By exploiting (2.28), and by denoting with $\mathbf{C}^{-1}_{\mathbf{y}_{\text{c,a}}|\mathcal{H}_1} \triangleq \begin{bmatrix} \mathbf{A}_{11} & \mathbf{A}_{12} \\ \mathbf{A}_{21} & \mathbf{A}_{22} \end{bmatrix}$, the WL subvector $\mathbf{t}_{\text{wl-c}}$ can be expressed as:

$$\mathbf{t}_{\text{wl-c}} = \frac{[\mathbf{A}_{11}\,\mathbf{H}_c + \mathbf{A}_{12}\,\mathbf{H}_c^*]\,(\boldsymbol{\eta}_{\text{c}|\mathcal{H}_1} - \boldsymbol{\eta}_{\text{c}|\mathcal{H}_0})}{\sqrt{2}\,||[\mathbf{A}_{11}\,\mathbf{H}_c + \mathbf{A}_{12}\,\mathbf{H}_c^*]\,(\boldsymbol{\eta}_{\text{c}|\mathcal{H}_1} - \boldsymbol{\eta}_{\text{c}|\mathcal{H}_0})||_2^2} \tag{G.6}$$

By accounting for the inverse of a partitioned matrix [61], it results: $\mathbf{A}_{11} = [\mathbf{C}_{\mathbf{y}_c|\mathcal{H}_1} - \mathbf{C}_{\mathbf{y}_{\tilde{c}}^*|\mathcal{H}_1}(\mathbf{C}^*_{\mathbf{y}_c|\mathcal{H}_1})^{-1}\mathbf{C}^*_{\mathbf{y}_{\tilde{c}}^*|\mathcal{H}_1}]^{-1}$ and $\mathbf{A}_{12} = -\mathbf{C}^{-1}_{\mathbf{y}_c|\mathcal{H}_1}\mathbf{C}_{\mathbf{y}_{\tilde{c}}^*|\mathcal{H}_1}\mathbf{A}^*_{11}$. By substituting (2.18), (2.20), $\mathbf{A}_{11}$, $\mathbf{A}_{12}$ in (G.6), the proof is achieved.

Appendix H

Proof of Theorem 6

The proof is carried out by comparing the WL deflection coefficients (2.29) and (2.32) assured by the CD and the SCD approach, respectively, since, under the gaussian hypothesis, a larger deflection coefficient corresponds to a major detection accuracy [72, 76, 81]. To this aim, (2.29) and (2.32) can be rewritten, respectively, as:

$$m^2_{\text{wl-c}}(\mathbf{f}_{\text{wl-c}}) = 2\sqrt{2}\,||\boldsymbol{\Sigma}_{\text{wl-c}}\,(\boldsymbol{\eta}_{\text{c}|\mathcal{H}_1} - \boldsymbol{\eta}_{\text{c}|\mathcal{H}_0})||_2^2 \text{Re}\Big[(\boldsymbol{\mu}_{\text{c}|\mathcal{H}_1} - \boldsymbol{\mu}_{\text{c}|\mathcal{H}_0})^H\,\mathbf{t}_{\text{wl-c}}\Big]$$

$$m^2_{\text{wl-sc}}(\mathbf{f}_{\text{wl-sc}}) = 2\sqrt{2}\,||\boldsymbol{\Sigma}_{\text{wl-sc}}\,(\boldsymbol{\eta}_{\text{sc}|\mathcal{H}_1} - \boldsymbol{\eta}_{\text{sc}|\mathcal{H}_0})||_2^2 \text{Re}\Big[(\boldsymbol{\mu}_{\text{sc}|\mathcal{H}_1} - \boldsymbol{\mu}_{\text{sc}|\mathcal{H}_0})^H\,\mathbf{t}_{\text{wl-sc}}\Big].$$

By substituting (2.45) in these expressions, after some manipulations, one obtains:

$$\begin{aligned} m^2_{\text{wl-c}}(\mathbf{f}_{\text{wl-c}}) &= 2\,\left(\nu_{1|\mathcal{H}_1} - \nu_{1|\mathcal{H}_0}\right)^2 \\ &\cdot \mathbf{1}^T_{\{L_e+L_g-1\}} \text{Re}\Big[\mathbf{H}_1^H\left(\boldsymbol{\Omega}_{\text{c}}\,\mathbf{H}_1 - \mathbf{C}^{-1}_{\mathbf{y}_1|\mathcal{H}_1}\mathbf{C}_{\mathbf{y}_1^*|\mathcal{H}_1}\boldsymbol{\Omega}_{\text{c}}^*\,\mathbf{H}_1^*\right)\Big]\mathbf{1}_{\{L_e+L_g-1\}} \\ &+ 2\,\text{Re}\left\{(\overline{\boldsymbol{\eta}}_{\mathcal{H}_1} - \overline{\boldsymbol{\eta}}_{\mathcal{H}_0})^T\,\overline{\mathbf{H}}^H\,(\overline{\boldsymbol{\Omega}}\,\overline{\mathbf{H}} - \mathbf{C}^{-1}_{\overline{\mathbf{y}}|\mathcal{H}_1}\,\mathbf{C}_{\overline{\mathbf{y}}^*|\mathcal{H}_1}\overline{\boldsymbol{\Omega}}^*\,\overline{\mathbf{H}}^*)(\overline{\boldsymbol{\eta}}_{\mathcal{H}_1} - \overline{\boldsymbol{\eta}}_{\mathcal{H}_0})\right\} \end{aligned} \tag{H.1}$$

$$\begin{aligned} m^2_{\text{wl-sc}}(\mathbf{f}_{\text{wl-sc}}) &= \left(\nu_{0|\mathcal{H}_1} - \nu_{0|\mathcal{H}_0}\right)^2\,\zeta^{-1}_{0|\mathcal{H}_1}\,L_e \\ &+ 2\,\text{Re}\left\{(\overline{\boldsymbol{\eta}}_{\mathcal{H}_1} - \overline{\boldsymbol{\eta}}_{\mathcal{H}_0})^T\,\overline{\mathbf{H}}^H(\overline{\boldsymbol{\Omega}}\,\overline{\mathbf{H}} - \mathbf{C}^{-1}_{\overline{\mathbf{y}}|\mathcal{H}_1}\,\mathbf{C}_{\overline{\mathbf{y}}^*|\mathcal{H}_1}\overline{\boldsymbol{\Omega}}^*\,\overline{\mathbf{H}}^*)(\overline{\boldsymbol{\eta}}_{\mathcal{H}_1} - \overline{\boldsymbol{\eta}}_{\mathcal{H}_0})\right\} \end{aligned} \tag{H.2}$$

where, the positive common term, i.e., $2\text{Re}\{\ldots\}$, depends on the $(M-1)$ SUs different from SU_0 and SU_1. Consequently,

$$\begin{aligned} &m^2_{\text{wl-sc}} \gtrless m^2_{\text{wl-c}} \Leftrightarrow \\ &\left(\nu_{0|\mathcal{H}_1} - \nu_{0|\mathcal{H}_0}\right)^2\,\zeta^{-1}_{0|\mathcal{H}_1}\,L_e \gtrless 2\,\left(\nu_{1|\mathcal{H}_1} - \nu_{1|\mathcal{H}_0}\right)^2\,\mathbf{1}^T_{\{L_e+L_g-1\}} \\ &\text{Re}\Big[\mathbf{H}_1^H\left(\boldsymbol{\Omega}_{\text{c}}\,\mathbf{H}_1 - \mathbf{C}^{-1}_{\mathbf{y}_1|\mathcal{H}_1}\mathbf{C}_{\mathbf{y}_1^*|\mathcal{H}_1}\boldsymbol{\Omega}_{\text{c}}^*\,\mathbf{H}_1^*\right)\Big]\mathbf{1}_{\{L_e+L_g-1\}} \end{aligned} \tag{H.3}$$

where both the members are positive, due to the DC definition. From (H.3), it results:

$$m^2_{\text{wl-sc}} \gtrless m^2_{\text{wl-c}} \Leftrightarrow$$
$$\frac{\left(\nu_{0|\mathcal{H}_1} - \nu_{0|\mathcal{H}_0}\right)^2 \zeta^{-1}_{0|\mathcal{H}_1} L_e}{2\left(\nu_{1|\mathcal{H}_1} - \nu_{1|\mathcal{H}_0}\right)^2 \mathbf{1}^T_{\{L_e+L_g-1\}} \text{Re}\left[\mathbf{H}_1^H \left(\mathbf{\Omega}_{\text{c}}\, \mathbf{H}_1 - \mathbf{C}^{-1}_{\mathbf{y}_1|\mathcal{H}_1} \mathbf{C}_{\mathbf{y}_1^*|\mathcal{H}_1} \mathbf{\Omega}^*_{\text{c}}\, \mathbf{H}^*_1\right)\right] \mathbf{1}_{\{L_e+L_g-1\}}} \gtrless 1 \tag{H.4}$$

Hence, by denoting with θ_{wl} the positive quantity defined in (2.48), (H.4) is equivalent to $m^2_{\text{wl-sc}} \gtrless m^2_{\text{wl-c}} \Leftrightarrow \theta_{\text{wl}} \gtrless 1$.

Appendix I

Proof of Proposition 5

From (3.23) we have that:

$$\frac{d\,P_{f,t}(T_s)}{dT_s} = -\frac{1}{\sqrt{2\pi}}\frac{\gamma(R)\sqrt{f_s}}{2\sqrt{T_s}}\,\exp\left(-\frac{A_{f,t}^2(T_s)}{2}\right) \tag{I.1}$$

where $A_{f,t}(T_s) = Q^{-1}(\alpha)\sqrt{1+2\gamma(R)} + \gamma(R)\sqrt{T_s f_s}$ is the Q-function argument of $P_{f,t}(T_s)$ in (3.23). In particular, from (I.1), after simple mathematical manipulations, we have:

$$\frac{d^2\,P_{f,t}(T_s)}{dT_s^2} = \frac{\gamma(R)\sqrt{f_s}}{4\sqrt{2\pi}\,T_s}\left(\frac{1}{\sqrt{T_s}} + \gamma(R)\sqrt{f_s}\,A_{f,t}(T_s)\right)\exp\left(-\frac{A_{f,t}^2(T_s)}{2}\right) \tag{I.2}$$

To prove the convexity of $P_{f,t}(T_s)$, we have to single-out the conditions under which (I.2) is positive. Thus, by accounting for the expression of $A_{f,t}(T_s)$, we have:

$$\left(\gamma(R)^2\,f_s\right)T_s - \left(\gamma(R)\,\sqrt{f_s}\,|Q^{-1}(\alpha)|\sqrt{1+2\gamma(R)}\right)\sqrt{T_s} + 1 > 0 \tag{I.3}$$

and, by substituting $\sqrt{T_s} = t$, we have that (I.3) is satisfied under the condition (a) otherwise (b) in (3.24), where:

$$t_1 = \frac{|Q^{-1}(\alpha)|\sqrt{1+2\gamma(R)} - \sqrt{|Q^{-1}(\alpha)|^2\,(1+2\gamma(R)) - 4}}{2\gamma(R)\sqrt{f_s}} \tag{I.4}$$

$$t_2 = \frac{|Q^{-1}(\alpha)|\sqrt{1+2\gamma(R)} + \sqrt{|Q^{-1}(\alpha)|^2\,(1+2\gamma(R)) - 4}}{2\gamma(R)\sqrt{f_s}} \tag{I.5}$$

In particular, since $t_2 < |Q^{-1}(\alpha)|\sqrt{1+2\gamma(R)}/(\gamma(R)\sqrt{f_s})$, then the condition (b) is also satisfied when $\sqrt{T_s} > |Q^{-1}(\alpha)|\sqrt{1+2\gamma(R)}/(\gamma(R)\sqrt{f_s})$, that is equivalent to the condition: $A_{f,t}(T_s) > 0 \Leftrightarrow P_{f,t}(T_s) < 0.5$.

Appendix J

Proof of Proposition 6

To prove the convexity of $P_{f,s}(T_s)$ in (3.11), we have to prove the convexity of $P_d(s,T_s)$ in (3.26) when $s > R$. Thus, similarly to the Proposition 5, we have that:

$$\frac{\partial\, P_d(s,T_s)}{\partial T_s} = -\frac{1}{\sqrt{2\pi}}\frac{(\gamma(R)-\gamma(s))}{\sqrt{1+2\gamma(s)}}\frac{\sqrt{f_s}}{2\sqrt{T_s}}\exp\left(-\frac{A_d^2(s,T_s)}{2}\right) \qquad \text{(J.1)}$$

where $A_d(s,T_s)$ is the Q-function argument of $P_d(s,T_s)$ in (3.26). In particular, from (J.1), after simple mathematical manipulations, we have:

$$\frac{\partial^2\, P_d(s,T_s)}{\partial\, T_s^2} = \frac{(\gamma(R)-\gamma(s))}{\sqrt{1+2\gamma(s)}}\frac{\sqrt{f_s}}{4\sqrt{2\pi}\,T_s}\cdot$$
$$\cdot\left(\frac{1}{\sqrt{T_s}}+\frac{(\gamma(R)-\gamma(s))}{\sqrt{1+2\gamma(s)}}\sqrt{f_s}\,A_d(s,T_s)\right)\exp\left(-\frac{A_d^2(s,T_s)}{2}\right) \qquad \text{(J.2)}$$

To prove the convexity of $P_d(s,T_s)$, we have to single-out the conditions under which (J.2) is positive. Thus, by accounting for the expression of $A_d(s,T_s)$, we have:

$$\left(\frac{(\gamma(R)-\gamma(s))^2\ f_s}{1+2\gamma(s)}\right)T_s$$
$$-\left(\frac{(\gamma(R)-\gamma(s))}{1+2\gamma(s)}\sqrt{f_s}\,|Q^{-1}(\alpha)|\sqrt{1+2\gamma(R)}\right)\sqrt{T_s}+1>0 \qquad \text{(J.3)}$$

and, by substituting $\sqrt{T_s} = t$, we have that (J.3) is satisfied under the condition (c) otherwise (d) in (3.27), where:

$$t_3 = \frac{|Q^{-1}(\alpha)|\sqrt{1+2\gamma(R)} - \sqrt{|Q^{-1}(\alpha)|^2\,(1+2\gamma(R)) - 4\,(1+2\gamma(s))}}{2\,(\gamma(R)-\gamma(s))\,\sqrt{f_s}} \tag{J.4}$$

$$t_4 = \frac{|Q^{-1}(\alpha)|\sqrt{1+2\gamma(R)} + \sqrt{|Q^{-1}(\alpha)|^2\,(1+2\gamma(R)) - 4\,(1+2\gamma(s))}}{2\,(\gamma(R)-\gamma(s))\,\sqrt{f_s}} \tag{J.5}$$

Bibliography

[1] R. Axelrod, *The Evolution of Cooperation.* Science, New Series, 1981.

[2] ——, *The Complexity of Cooperation: Agent-Based Models of Competition and Collaboration.* Princeton University Press, 1997.

[3] F. H. P. Fotzek and M. D. Katz, *Cooperation in Wireless Networks: Principles and Applications.* Springer, 2006.

[4] M. Uysal, *Cooperative Communications for Improved Wireless Network Transmission: Framework for Virtual Antenna Array Applications.* Information Science Reference, 2009.

[5] J. Laneman and G. Wornell, "Distributed space-time block coded protocols for exploiting cooperative diversity in wireless networks," *IEEE Trans. on Information Theory*, vol. 49, pp. 2415–2425, Oct. 2003.

[6] A. Sendonaris, E. Erkip, and B. Aazhang, "User cooperation diversity – part i & ii," *IEEE Trans. on Communications*, vol. 51, pp. 1927–1948, Nov. 2003.

[7] J. Laneman, D. Tse, and G. Wornell, "Cooperative diversity in wireless networks: efficient protocols and outage behaviors," *IEEE Trans. on Information Theory*, vol. 50, pp. 3062–3080, Sep. 2004.

[8] H. Jafarkhani, *Space-Time Coding - Theory and Practice.* Cambridge University Press, 2005.

[9] H. Wymeersch, J. Lien, and M. Z. Win, "Cooperative localization in wireless networks," *Proceedings of the IEEE*, vol. 97, pp. 427–450, March 2009.

[10] H. Ochiai, P. Mitran, H. V. Poor, and V. Tarokh, "Collaborative beamforming for distributed wireless ad hoc sensor networks," *IEEE Trans. on Signal Processing*, vol. 53, pp. 4110–4124, Oct. 2005.

[11] H. Shan, W. Zhuang, and W. Zongxin, "Distributed cooperative mac for multihop wireless networks," *IEEE Communications Magazine*, vol. 47, pp. 126–133, Feb. 2009.

[12] L. Tie, M. Motani, and V. Srinivasan, "Cooperative asynchronous multichannel mac: Design, analysis, and implementation," *IEEE Trans. on Mobile Computing*, vol. 8, pp. 338–352, August 2008.

[13] E. M. Royer and C.-K. Toh, "A review of current routing protocols for ad hoc mobile wireless networks," *IEEE Personal Communications*, vol. 86, pp. 46–55, August 2002.

[14] B. Gui, L. Dai, and L. J. Cimini, "Routing strategies in multihop cooperative networks," *IEEE Trans. on Wireless Communications*, vol. 8, pp. 843–855, Feb. 2009.

[15] S. Bohacek, "Performance improvements provided by route diversity in multihop wireless networks," *IEEE Trans. on Mobile Computing*, vol. 7, pp. 372–384, March 2008.

[16] A. M. Wyglinski, M. N. Nekovee, and Y. T. Hou, *Cognitive Radio Communications and Networks: Principles and Practice*. Elsevier, 2010.

[17] K. Ben Letaief and W. Zhang, "Cooperative communications for cognitive radio networks," *Proceedings of the IEEE*, vol. 97, May 2009.

[18] I. F. Akyildiz, W.-Y. Lee, and K. R. Chowdhury, "Crahns: Cognitive radio ad hoc networks," *Ad Hoc Networks (Elsevier)*, vol. 7, pp. 810–836, 2009.

[19] I. F. Akyildiz, B. F. Lo, , and R. Balakrishnan, "Cooperative spectrum sensing in cognitive radio networks: A survey," *Physical Communication (Elsevier) Journal*, vol. 4, no. 1, Mar. 2011.

[20] S. Yiu, R. Schober, and L. Lampe, "Distributed space-time block coding," *IEEE Trans. on Communications*, vol. 54, pp. 1195–1206, July 2006.

[21] B. Sirkeci-Mergen and A. Scaglione, "Randomized space-time coding for distributed cooperative communication," *IEEE Trans. on Signal Processing*, vol. 55, pp. 5003–5017, Oct. 2007.

[22] M. Sharp, A. Scaglione, and B. Sirkeci-Mergen, "Randomized cooperation in asynchronous dispersive links," *IEEE Trans. on Communications*, vol. 57, pp. 64–68, Jan. 2009.

[23] F. Verde and A. Scaglione, "Randomized space-time block coding for distributed amplify-and-forward cooperative relays," in *Proc. of IEEE Int. Conf. Acoustics, Speech and Signal Process (ICASSP)*, Mar. 2010, pp. 3030–3033.

[24] ——, "Decentralized space-time block coding for two-way relay networks," in *Proc. of 11th IEEE Workshop on Signal Processing Advances in Wireless Communications (SPAWC)*, June 2010, pp. 1–5.

[25] F. Verde, "Design of randomized space-time block codes for amplify-and-forward cooperative relaying," in *Proc. of 5th International Symposium on Communications, Control, and Signal Processing (ISCCSP)*, May 2012, pp. 1–5.

[26] F. Verde, D. Darsena, and A. Scaglione, "Cooperative randomized mimo-ofdm downlink for multicell networks: design and analysis," *IEEE Trans. on Signal Processing*, vol. 58, pp. 384–402, Jan. 2010.

[27] F. Verde, T. Korakis, E. Erkip, and A. Scaglione, "A simple recruitment scheme of multiple nodes for cooperative mac," *IEEE Trans. on Communications*, vol. 58, pp. 2667–2682, Sept. 2010.

[28] S. Bagheri, F. Verde, D. Darsena, and A. Scaglione, "Randomized decode-and-forward strategies for two-way relay networks," *IEEE Trans. on Wireless Communications*, vol. 10, pp. 4214–4225, Dec. 2011.

[29] P. Liu, C. Nie, T. Korakis, E. Erkip, S. Panwar, F. Verde, and A. Scaglione, "Sticmac: A mac protocol for robust space-time coding in cooperative wireless lans," *IEEE Trans. on Wireless Communications*, vol. 11, pp. 1358–1369, Apr. 2012.

[30] V. Tarokh, N. Seshadri, and A. Calderbank, "Space-time codes for high data rate wireless communication: performance criterion and code construction," *IEEE Trans. on Information Theory*, vol. 44, pp. 744–765, Mar. 1998.

[31] V. Tarokh, H. Jafarkhani, and A. Calderbank, "Space-time block codes from orthogonal designs," *IEEE Trans. on Information Theory*, vol. 45, pp. 1456–1467, July 1999.

[32] K. Blackard, T. Rappaport, and C. Bostian, "Measurements and models of radio frequency impulse noise for indoor wireless communications," *IEEE Journal on Selected Areas in Communications*, vol. 11, pp. 991–1001, Sep. 1993.

[33] T. Blankenship and T. Rappaport, "Characteristics of impulsive noise in the 450-mhz band in hospitals and clinics," *IEEE Trans. on Antennas and Propagation*, vol. 46, pp. 194–203, Feb. 1998.

[34] Q. Shan, "Estimation of impulsive noise in an electricity substation," *IEEE Trans. on Electromagnetic Compatibility*, vol. 53, pp. 653–663, Aug. 2011.

[35] L. Lampe, R. Schober, and S. Yiu, "Distributed space-time coding for multihop transmission in power line communications networks," *IEEE Journal on Selected Areas in Communications*, vol. 24, pp. 1389–1400, July 2006.

[36] M. Kuhn, S. Berger, I. Hammerstrom, and A. Wittneben, "Power line enhanced cooperative wireless communications," *IEEE Journal on Selected Areas in Communications*, vol. 24, pp. 1401–1410, July 2006.

[37] D. Middleton, "Statistical-physical models of electromagnetic interference," *IEEE Trans. on Electromagnetic Compatibility*, vol. 19, pp. 106–127, Aug. 1977.

[38] A. Spaulding and D. Middleton, "Optimum reception in the impulse interference environment – part i: coherent detection," *IEEE Trans. on Communications*, vol. 25, pp. 910–923, Sep. 1977.

[39] ——, "Procedure for determining the parameters of a first-order canonical models of class a and class b electromagnetic interference," *IEEE Trans. on Electromagnetic Compatibility*, vol. 21, pp. 190–208, Aug. 1979.

[40] M. Ghosh, "Analysis of the effect of impulse noise on multicarrier and single-carrier qam systems," *IEEE Trans. on Communications*, vol. 44, pp. 145–147, Feb. 1996.

[41] J. Ilow and D. Hatzinakos, "Analytic alpha-stable noise modeling in a poisson field of interferers or scatterers," *IEEE Trans. on Signal Processing*, vol. 51, pp. 64–76, Jan. 2003.

[42] C. Tepedelenlioğlu and P. Gao, "On the diversity reception over fading channels with impulse noise," *IEEE Trans. on Vehicular Technology*, vol. 54, pp. 2037–2047, Nov. 2005.

[43] P. Gao and C. Tepedelenlioğlu, "Space-time coding over fading channels with impulse noise," *IEEE Trans. on Wireless Communications*, vol. 6, pp. 220–229, Jan. 2007.

[44] J. Lee and C. Tepedelenlioğlu, "Space-time coding over fading channels with stable noise," *IEEE Trans. on Vehicular Technology*, vol. 60, pp. 3169–3177, Sep. 2011.

[45] A. Nasri, R. Schober, and I. Blake, "Performance and optimization of amplify-and-forward cooperative diversity systems in generic noise and interference," *IEEE Trans. on Wireless Communications*, vol. 10, pp. 1132–1143, Apr. 2011.

[46] S. Al-Dharrab and M. Uysal, "Cooperative diversity in the presence of impulse noise," *IEEE Trans. on Wireless Communications*, vol. 8, pp. 4730–4739, Sep. 2009.

[47] H. V. Khuong and T. Le-Ngoc, "Effect of impulsive noise on decode-and-forward cooperative relaying over fading channel," in *Proc. of IEEE Wireless Communications and Networking Conference (WCNC)*, Mar. 2011, pp. 1392–1397.

[48] R. Savoia and F. Verde, "Performance analysis of distributed spacetime block coding schemes in middleton class a noise," *IEEE Trans. on Vehicular Technology*, vol. 62, pp. 2579–2595, Jan. 2013.

[49] ——, "Performance analysis of decode-and-forward relaying in impulsive noise environments," in *Proc. of IEEE Eighth International Symposium on Wireless Communincation Systems (ISWCS)*, Nov. 2011, p. 412.416.

[50] P. Huber, *Robust Statistics*. New York: Wiley, 1981.

[51] X. Wang and H. Poor, "Robust multiuser detection in non-gaussian channels," *IEEE Trans. on Signal Processing*, vol. 47, pp. 289–305, Feb. 1999.

[52] S. Zhidkov, "Analysis and comparison of several simple impulse noise mitigation schemes for ofdm receivers," *IEEE Trans. on Communications*, vol. 56, pp. 5–9, Jan. 2008.

[53] D. Tse and P. Viswanath, *Fundamentals of Wireless Communication*. Cambridge University Press, 2005.

[54] R. Narasimhan, "Finite-snr diversity-multiplexing tradeoff for correlated rayleigh and rician mimo channels," *IEEE Trans. on Information Theory*, vol. 52, pp. 3965–3979, Sep. 2006.

[55] P. Delaney, "Signal detection in multivariate class-a interference," *IEEE Trans. on Communications*, vol. 43, pp. 365–373, Feb. 2006.

[56] K. Seddik, A. Sadek, A. Ibrahim, and K. Liu, "Design criteria and performance analysis for distributed space-time coding," *IEEE Trans. on Vehicular Technology*, vol. 57, pp. 2280–2292, July. 2008.

[57] J. Häring and A. Vinck, "Performance bounds for optimum and suboptimum receprtion under class-a impulsive noise," *IEEE Trans. on Communications*, vol. 50, pp. 1130–1136, July. 2002.

[58] J. Proakis, *Digital Communications*. New York: McGraw-Hill, 2001.

[59] R. K. R.S. Blum and B. Sadler, "An adaptive spatial diversity receiver for non-gaussian interference and noise," *IEEE Trans. on Signal Processing*, vol. 47, pp. 2100–2111, Aug. 1999.

[60] K. Vastola, "Threshold detection in narrow-band non-gaussian noise," *IEEE Trans. on Communications*, vol. 32, pp. 134–139, Feb. 1984.

[61] R. A. Horn and C. R. Johnson, *Matrix Analysis*. Cambridge University Press, 1990.

[62] A. Ben-Israel and T. N. E. Greville, *Generalized Inverses*. Springer-Verlag, 2002.

[63] L. Tran, T. Wisocki, J. Seberry, A. Mertins, and S. Adams, "Novel constructions of improved square complex orthogonal designs for eight transmit antennas," *IEEE Trans. on Information Theory*, vol. 55, pp. 4439–4448, Oct. 2009.

[64] S. Alamouti, "A simple transmit diversity technique for wireless communications," *IEEE Journal on Selected Areas in Communications*, vol. 16, pp. 1451–1458, Oct. 1998.

[65] W. Su, X.-G. Xia, and K. Liu, "A systematic design of high-rate complex orthogonal space-time block codes," *IEEE Trans. Communication Letters*, vol. 8, pp. 380–382, June 2004.

[66] S. Haykin, "Cognitive radio: brain-empowered wireless communications," *IEEE Journal on Selected Areas in Communications*, vol. 23, pp. 201–220, Feb. 2005.

[67] I. F. Akyildiz, W. Y. Lee, M. C. Vuran, and S. Mohanty, "A survey on spectrum management in cognitive radio networks," *IEEE Communication Magazine*, vol. 46, no. 4, pp. 40 – 48, April 2008.

[68] Q. Zhao and B. M. Sadler, "A survey of dynamic spectrum access," *IEEE Signal Processing Magazine*, vol. 24, no. 3, pp. 79 – 89, May 2007.

[69] A. Ghasemi and E. S. Sousa, "Spectrum sensing in cognitive radio networks: requirements, challenges and design trade-offs," *IEEE Communications Magazine*, vol. 46, no. 4, pp. 32 – 39, April 2008.

[70] E. Axell, G. Leus, E. G. Larsson, and H. V. Poor, "Spectrum sensing for cognitive radio : State-of-the-art and recent advances," *IEEE Signal Processing*, vol. 29, no. 3, pp. 101 – 116, May 2012.

[71] A. S. Cacciapuoti, I. F. Akyildiz, and L. Paura, "Correlation-aware user selection for cooperative spectrum sensing in cognitive radio ad hoc networks," *IEEE Journal on Selected Areas in Communications*, vol. 30, pp. 297–306, Feb. 2012.

[72] A. S. Cacciapuoti, M. Caleffi, D. Izzo, and L. Paura, "Cooperative spectrum sensing techniques with temporal dispersive reporting channels," *IEEE Trans. Wireless Commun.*, vol. 10, pp. 3392 – 3402, Oct. 2011.

[73] S. Mishra, A. Sahai, and R. Brodersen, "Cooperative sensing among cognitive radios," in *Proc. of IEEE ICC*, May 2009.

[74] A. Ghasemi and E. Sousa, "Collaborative spectrum sensing for opportunistic access in fading environments," in *Proc. of IEEE DySPAN*, Nov. 2005.

[75] A. Cacciapuoti, M. Caleffi, L. Paura, and R. Savoia, "Decision maker approaches for cooperative spectrum sensing: Participate or not participate in sensing?" *IEEE Trans. on Wireless Communications*, vol. 12, pp. 2445–2457, March 2013.

[76] S. M. Kay, *Fundamentals of Statistical Signal Processing II: Detection Theory.* Prentice-Hall, 1998.

[77] A. S. Cacciapuoti, M. Caleffi, and L. Paura, "Widely linear cooperative spectrum sensing for cognitive radio networks," in *Proc. of IEEE GLOBECOM 2010*, Dec. 2010, pp. 1–5.

[78] A. Ben-Israel and T. N. E. Greville, *Generalized Inverses: Theory and Applications.* Springer-Verlag, 2002.

[79] P. Schreier and L. Scharf, "Second-order analysis of improper complex random vectors and processes," *IEEE Trans. Signal Processing*, vol. 51, pp. 714–725, Mar. 2003.

[80] Y.-C. Liang, Y. Zeng, E. C. Peh, and A. T. Hoang, "Sensing-throughput tradeoff for cognitive radio networks," *IEEE Trans. Wireless Commun.*, vol. 7, pp. 1326–1337, Apr. 2008.

[81] Z. Quan, S. Cui, and A. H. Sayed, "Optimal linear cooperation for spectrum sensing in cognitive radio networks," *IEEE Journal of Select. Top. in Signal Processing*, pp. 28–40, Feb. 2008.

[82] B. Picinbono, "Second-order complex random vectors and normal distributions," *IEEE Trans. Signal Processing*, vol. 44, pp. 2637–2640, Oct. 1996.

[83] P. V. Mikheev, "Multi-dimensional gaussian probability density and its applications in the degenerate case," *Radiophysics and Quantum Electronics*, vol. 49, pp. 626–634, July 2006.

[84] B. J. Ma, G. Y. Li, and B. H. Juang, "Signal processing in cognitive radio," *IEEE Proceedings*, vol. 97, no. 5, pp. 805 – 823, May 2009.

[85] W.-Y. Lee and I. F. Akyildiz, "Optimal spectrum sensing framework for cognitive radio networks," *IEEE Trans. Wireless Communications*, vol. 7, no. 10, pp. 3845 – 3857, Oct. 2008.

[86] D. Tuam and B. L. Mark, "Joint spatial-temporal spectrum sensing for cognitive radio networks," *IEEE Trans. on Vehicular Technology*, vol. 59, no. 7, pp. 3480 – 3490, Sept. 2010.

[87] R. Tandra, A. Sahai, and V. Veeravalli, "Unified space-time metrics to evaluate spectrum sensing," *IEEE Communications Magazine*, vol. 49, no. 3, pp. 54 – 61, March 2011.

[88] Q. Wu, G. Ding, J. Wang, and Y.-D. Yao, "Spatial-temporal opportunity detection for spectrum-heterogeneous cognitive radio networks: Two-dimensional sensing," *IEEE Trans. Wireless Communications*, vol. 12, no. 2, pp. 516 – 526, Feb. 2013.

[89] K. W. Choi, E. Hossain, and D. I. Kim, "Cooperative spectrum sensing under a random geometric primary user network model," *IEEE Trans. Wireless Communications*, vol. 10, no. 6, pp. 1932 – 1944, April. 2011.

[90] A. W. Min, X. Zhang, and K. G. Shin, "Detection of small-scale primary users in cognitive radio networks," *IEEE Journal on Selected Areas in Communications*, vol. 29, no. 2, pp. 349 – 361, Jan. 2011.

[91] W. Han, J. Li, Z. Li, J. Si, and Y. Zhang, "Spatial false alarm in cognitive radio network," *IEEE Trans. on Signal Processing*, vol. 61, no. 6, pp. 1375 – 1388, March 2013.

[92] L. Paura and R. Savoia, "Mobility-aware sensing enabled capacity in cognitive radio networks," in *Proc. of IEEE International Workshop on Measurements and Networking*, Oct. 2013, pp. 179 – 183.

[93] T. Camp, J. Boleng, and V. Davies, "A survey of mobility models for ad hoc network research," *Wireless Communications and Mobile Computing*, vol. 2, no. 5, pp. 483 – 502, 2002.

[94] C. Bettstetter, H. Hartenstein, and X. Perez-Costa, "Stochastic properties of the random waypoint mobility model," *Wireless Networks*, 2004.

[95] A. S. Cacciapuoti, I. F. Akyildiz, and L. Paura, "Primary-user mobility impact on spectrum sensing in cognitive radio networks," in *Proc. of IEEE Symposium on Personal Indoor and Mobile Radio Communications*, Sep. 2011, pp. 451 – 456.

[96] ——, "Optimal primary-user mobility aware spectrum sensing design for cognitive radio networks," *IEEE Journal on Selected Areas in Communications*, vol. 31, no. 11, pp. 2161 – 2172, Nov. 2013.

[97] B. Sklar, "Rayleigh fading channels in mobile digital communication systems - characterization," *IEEE Communications Magazine*, vol. 35, no. 9, pp. 136 – 146, 1997.

[98] A. Papoulis, *Probability, Random Variables, and Stochastic Processes.* New York: McGraw-Hill, 1984.

[99] X. Zhang and H. Su, "Cream-mac: Cognitive radio-enabled multichannel mac protocol over dynamic spectrum access networks," *IEEE Journal of Selected Topics in Signal Processing*, vol. 5, no. 1, pp. 110 – 123, Feb. 2011.

[100] A. Goldsmith, *Wireless Communication.* Cambridge University Press.

[101] A. Ghasemi and E. S. Sousa, "Opportunistic spectrum access in fading channels through collaborative sensing," *Journal of Communications*, vol. 2, no. 2, pp. 71 – 82, Mar. 2007.

[102] K. Letaief and W. Zhang, "Cooperative communications for cognitive radio networks," *IEEE Proceedings*, vol. 97, no. 5, pp. 878 – 893, May 2009.

[103] N. Goodman, "Statistical analysis based on a certain multivariate complex gaussian distribution (an introduction)," *The Annals of Mathematical Statistics*, vol. 44, pp. 152–177, 1963.

[104] A. W. Marshall and I. Olkin, *Inequalities: Theory of majorization and its applications.* Academic Press, New York, 1979.